Design and fabrication of ultrathin nanophotonic devices based on metasurfaces

A DISSERTATION

Submitted in partial fulfillment of the
requirements for the the award of the degree
of
DOCTOR OF PHILOSOPHY
in
FACULTY OF PHYSICS

By

VISHAL VASHISTHA

FACULTY OF PHYSICS
ADAM MICKIEWICZ UNIVERSITY IN POZNAN
POLAND - 61 - 712
Dec, 2019

CANDIDATE'S DECLARATION

I hereby declare that this thesis report entitled **Design and fabrication of ultrathin nanophotonic devices based on metasurfaces**, submitted to the Faculty of Physics, Adam Mickiewicz University, Poznan, Poland, in partial fulfillment of the requirements for the award of the Degree of Doctor of Philosophy in Physics is an authentic record of the work carried out by me during the period from September 2016 to December 2019 under the supervision of **Prof. Maciej Krawczyk, and Dr. Andriy. E. Serebryannikov, Faculty of Physics, Adam Mickiewicz University, Poznan, Poland.** The matter presented in this thesis report has not been submitted by me for the award of any other degree of this institute or any other institute.

Date:

Place: Poznan

Vishal Vashistha

CERTIFICATE

This is to certify that the above statement made by the candidate is true to the best of my knowledge and belief.

Prof. Maciej Krawczyk
Professor
Faculty of Physics
Adam Mickiewicz University,
Poznan, Poland.

Dr. Andriy. E. Serebryannikov
Faculty of Physics
Adam Mickiewicz University,
Poznan, Poland.

You have a right to perform your prescribed duties, but you are not entitled to the fruits of your actions. Never consider yourself to be the cause of the results of your activities, nor be attached to inaction.

Bhagvad Geeta, Verse 47, Chapter 2

ABSTRACT

Light is one of the most fascinating research areas of science since the past few centuries and this century no exception. In 17^{th} century, Snell's law was introduced by Willebrord Snellius a Dutch astronomer and mathematician, which explains the properties of refraction and reflection of light. In 2011, prof. Capasso group from Harvard University generalized the Snell's law and introduced a new way to modify the wave fronts by using phase varying surfaces. The modified Snell's law follows the Fermat principle for the phase-changing surfaces. This phase changing surfaces can be created using tiny nanostructures to arbitrarily modified the amplitude, phase, and polarization of the wave. They are commonly considered as a broad class of metasurfaces. More generally, metasurfaces are artificially designed nanostructures which can modulate certain properties of electromagnetic waves. Metasurface concept is scalable to an arbitrary wavelength range and very well followed especially in the visible range. In this thesis, I used the concept of metasurfaces to design and fabricate the different nanophotonics devices. I designed and fabricated the Si-based all-dielectric color filters which can be used in transmission and reflection mode. The color filter design presented in this thesis is very efficient due to its all-dielectric nature. I also designed dynamically tunable color filters with the aid of source polarisation and a liquid crystal. In addition, I applied the surface impedance approach to control in-plane propagation in the photonic crystal waveguide.

Acknowledgements

First and foremost, it is my immense pleasure to thank my supervisor Prof. Maciej Krawczyk, who believed in me and my capability to work. He provided me an opportunity to work in my area of interest. In addition, I would like to thank my co-supervisor, Dr. Andriy Serebryannikov, who provided me the opportunity to work on the project funded by National Science Centre (NCN, project no UMO-2015/17/B/ST3/00118), Poland. He provided a great amount of insight and advice. Without their guidance, this work would have been impossible.

I would also like to sincerely thank all my teammates who helped me, not only in scientific understanding, but filled joy and happiness into my daily routine. It would never have been easy without my teammates to find a friendly environment in a county with a completely different language and culture.

I would like to extend my thanks to Prof. KP Chen and his group members from NCTU University, Taiwan where I spent a couple of months as a visiting scholar. I was overwhelmed with their hospitality and Taiwanese culture. I also sincerely extend my thanks to Prof. Arka Majumdar's group from the University of Washington, USA where I was a visiting scholar for six months through the NCN Etuida-6 funded project no UMO-2018/31/N/ST7/03918. I really enjoyed my stay in one of my favorite cities, Seattle. There I acquired new skills which will surely help me to reach a new stage of my career in the future.

I owe a lot to my family, who provided me consistent support and encouragement during my years of study. Even these few words can not explain the feeling of my heartfelt feelings toward my family, I would like to pay the highest reward towards my family. Thanks to Skype free video calls which fill the space of my absence in my home.

Other then the peoples, I must owe my full regards to different research funding organization, based on that I was able to visit tonnes of place and that also solve my financial issues.

In sense, this thesis is the collective effort of several people's advice and it seems to be impossible to acknowledge each and everyone here. As a Chinese say, we can not thank all, so thanks to a supernatural power, who connected to me with different people & their contribution in my work cannot be ignored.

Abbreviations

CFA	**C**olor **F**ilter **A**rray
RGB	**R**ed **G**reen **B**lue
CST	**C**omputer **S**imulation **T**echnology
PhC	**P**hotonics **C**rystal
DR	**D**ielectric **R**esonator
DRA	**D**ielectric **R**esonator **A**ntenna
LC	**L**iquid **C**rystal
CMOS	**C**omplementary **M**etal **O**xide **S**emiconductor
ECS	**E**xtinction **C**ross **S**ection
A-Si	**A**morphous **S**ilicon
PML	**P**erfect **M**atching **L**ayer
TFSF	**T**otal **F**ield **S**cattered **F**ield
CIE	**C**ommission **I**nternationale de **l'E**clairage
EBL	**E**lectron **B**eam **L**ithography
FDTD	**F**inite **D**ifference **T**ime **D**omain

Contents

List of Figures

List of Tables

Chapter 1

Introduction

Flat photonic devices will be highly demanded in the various future applications, and metasurfaces open the door to meet those demands [2]. $Metasurfaces$ are extremely thin artificially designed and engineered surfaces, which are composed of spatially varying resonating nanostructures [3]. These resonating nanostructures are known as nanoscatters, or nanoantennas or nanoresonators. The two dimensional (2d) $metasurfaces$ can steer the wave at the optical frequency with high efficiency by discretization the phase of the light in transmission (reflection) through (from) the metasurface. Metasurfaces impart the accurate phase at subwavelength scale resolution that allows making new ultra-compact flat nanophotonic devices such as color filters, metalenses, axicon devices, holograms, color displays, and polarimeters [2]. The single-step fabrication process makes it easy to fabricate and integrate with the existing devices.

1.1 Physics of metasurfaces

One of the goals of photonic engineering is to control the propagation of light. The one practical approach to achieve this goal at microwave frequencies was introduced by Prof. John Pendry who proposed metamaterials, in which propagation of the wave is controlled by means of the negative permittivity and permeability [4]. Conventional metals have an electric response (negative permittivity) but no magnetic response. The origin of negative permittivity in metals can be understood from the Drude model.

The origin of the magnetic response is usually due to the flow of orbital currents or unpaired electron spin, but both effects only respond to electromagnetic waves at low frequencies [5]. Prof. Pendry proposed to create a magnetic response by using metallic mesostructures [6]. He proposed to use an artificial loops similar to the orbital current in natural magnetic materials. He designed a metal-based split-ring resonator (SRR) to create strong magnetism at higher frequencies as shown in Fig. 1.1 [7]. When an electromagnetic (EM) wave interacts with the SRR in case of magnetic field perpendicular to its plane, it induces currents in the concentric rings. The created field is out of phase to the incoming wave and results in a strong magnetic response. This response can be further enhanced by increasing the number of SRRs in the array plane. The size of the SRR is much smaller than the incoming wave length. Thus, when the wave interacts with the array of SRRs, it effectively sees a medium as similar to the macroscopic interaction of the wave with the atom. By properly exciting the SRR, it is possible to achieve both electric and magnetic response from the SRR at the same frequency. It has to be noted that the induced fields are in the opposite directions to the incoming fields. Prof. Pendry also introduced the concept of effective permittivity (ϵ) and permeability (μ) to describe EM wave interaction with the metamaterials possessing the negative permittivity and negative permeability [8]. Later, these artificially designed atoms were known as meta-atoms (i.e., beyond atoms), and arrays of meta-atoms are commonly called as metamaterials. The special properties of metamaterials come from artificial structure designed by utilizing natural materials, rather primarily dependent on the intrinsic properties of the chemical constituents. So, it is possible to tune the response of SRR by tunning its geometric parameters. By properly choosing the parameters of SRR, it is possible to achieve sufficiently strong transmission at microwave frequencies. Estimates show that in order to design a metamaterial using SRR at optical frequencies, the size of the SRR must be less than 100 nm and spacing between them must be less than 10 nm. The fabrication of such SRRs is very challenging, especially with high precision. Also, calculation shows that amplitude of transmission from SRR decreases and negative permeability ceased to exist at optical frequencies [9].

Several alternative approaches have been proposed to design metamaterials at optical frequencies [10, 11]. In general, it is composed of two or more layers stacked in a specific manner to achieve negative permittivity and negative permeability. The fishnet like design is the most popular approach for designing metamaterials at optical frequencies, it is formed by stacking at least two metal layers separated by a dielectric layer [12, 13]. The other approaches to design metamaterials use 3D meta-molecules [14], materials

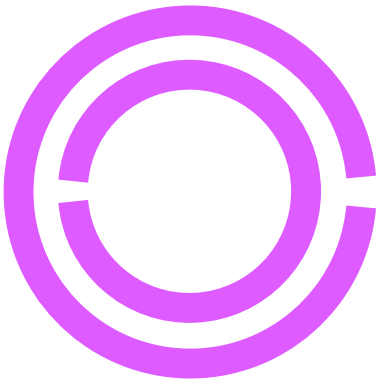

FIGURE 1.1: A split ring resonator (SRR), artificial magnetic unit to create magnetic response at microwave frequency.

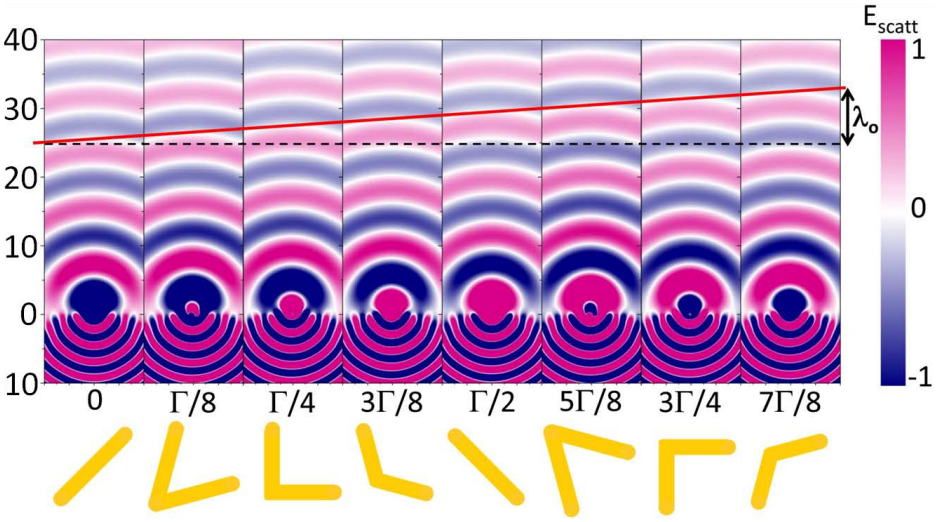

FIGURE 1.2: Phase gradient metasurfaces using V-shaped nanoantennas [3].

with a very high index [15], chiral metamaterials [16], and transformation optics methods [10, 17]. Although metamaterials draw high attention of the researchers, it is difficult to realize high-efficiency metamaterials at optical frequencies due to the three-dimensional nature of the designed structures. The reason for low efficiency is due to the stacking of multiple layers which results in high losses.

An alternate approach to control the propagation of light was proposed by prof. F. Capasso, who used two dimensional nanoantennas phase engineering approach to control the phase of the wave [2]. A phase gradient is introduced by spatially varying geometry of nanoantennas or by the orientation of the non-symmetric nanoantennas with the help of the geometrical phase along the flat interface. When the wave passes through the interface, the successive nanoantenna introduce the phase gradient at each point in space, as shown in Fig. 1.2. Such phase gradient surfaces represent a big class of metasurfaces and their operation can be explained using the generalized Snell's law. Snell's law is based on transnational symmetry and it follow the conservation of energy

and momentum. If there is a homogeneous interface, then the tangential component of propagation vector k must be conserved at the boundary between incidence half-space and transmission half-space as shown in Fig. 1.3. This can be written as

$$n_i k_o \sin\theta_i = n_t k_o \sin\theta_t, \tag{1.1}$$

where n_i and n_t, are refractive indexes of the incident media and refracted media, θ_i and θ_t are angles of incidence and refraction respectively. $k_o = \frac{2\pi}{\lambda_o}$ is the propagation vector in free space and λ_o is free space wavelength. The Snell's law can also be derived by applying the Fermats principle which states that light always follow the least time path. Now, let us consider a non-homogeneous interface where phase is spatially varying along the x-direction of the interface, see Fig. 1.3. If we apply the Fermats principle of stationary phase, we obtained the following:

$$n_i k_o \sin\theta_i dx + (\Phi + d\Phi) = n_t k_o \sin\theta_t dx + \Phi, \tag{1.2}$$

where Φ and $\Phi + d\Phi$ are change in phase in the x direction. The above presented equation can be rewritten as [3]:

$$n_i \sin\theta_i - n_t \sin\theta_t = \frac{\lambda_o}{2\pi}\frac{d\Phi}{dx}. \tag{1.3}$$

The similar equation can be derive for reflected wave and written as:

$$n_i \sin\theta_i - n_i \sin\theta_r = \frac{\lambda_o}{2\pi}\frac{d\Phi}{dx}, \tag{1.4}$$

where θ_r is the angle of reflection. Equations 1.3 and 1.4 differ from the standard Snell's law due to an additional term $\left(\frac{\lambda_o}{2\pi}\frac{d\Phi}{dx}\right)$. They represent the generalized Snell's law for refraction and reflection of EM wave [3]. Now, let consider a case, when an EM wave is incident normally to interface, i.e., $\theta_i = 0$, and there is a phase gradient along the interface. The generalized Snell's law is written as followed;

$$\sin\theta_t = \frac{\frac{\lambda_o}{2\pi}\frac{d\Phi}{dx}}{n_t}. \tag{1.5}$$

If the transmitted media is air $n_t = 1$, the angle of transmitted wave is given by;

$$\theta_t = \sin^{-1}\left(\frac{\lambda_o}{2\pi}\frac{d\Phi}{dx}\right). \tag{1.6}$$

The similar equation can be derived to calculate the angle of reflection using the generalized Snell's law. Considering the incident medium and refracted medium are same as air, the angle of reflection is given by

$$\theta_r = \sin^{-1}\left(\frac{\lambda_o}{2\pi}\frac{d\Phi}{dx}\right). \tag{1.7}$$

Equations 1.6 and 1.7 signify that, if there is a phase gradient $\frac{d\Phi}{dx}$ along the interface, then one can achieve any angle of reflection and refraction of the wave at a given wavelength. This effect is known as anomalous reflection and anomalous refraction of the wave, as shown in Fig. 1.4. Thus, the results are very important to design the metasurfaces for controlling reflection and refraction of the wave. It should be noted from the generalized Snell's law that phase gradient along the interface must be continuous to achieve perfect reflection and refraction of the wave. In practice, the phase gradient is introduced by subwavelength scale size of nanoantennas at discrete level. So, the discretization of the phase decides about the efficiency of anomalous refraction and reflection of the wave. Since the phase gradient is not continuous in practice and size of the nanoantennas is small as compared to the wavelength, the incoming wave sees the interface as a flat surface. As a result, when the light is incident on metasurfaces, anomalous refraction and reflection co-exist with an ordinary refraction and reflection of the wave. The latter satisfies the standard Snell's law, see Fig. 1.4. With the significant development in the area of nanofabrication, now it becomes possible to discretize the surfaces at subwavelength scale and design quite accurate size of nanoantennas, so even the discrete phase gradient can be quite close to continuous phase gradient, and thus may yield high efficiency beam steering devices. This makes the metasurfaces different than the metamaterials in the sense, that propagation of wave is controlled using phase gradient introduced by the nanoantennas on the surface unlike metamaterials, where propagation of wave depends upon the effective index of refraction.

The metasurfaces introduce the phase gradient at sub-wavelength scale, so that they have the capability in control of the amplitude, phase, and states of polarization of the wave. The recent development in the area of nanofabrication gives the ability to accurately control the wave propagation even at the visible spectrum by introducing nano-scatters [18–20]. This makes gradient metasurfaces a promising platform for nanophotonics applications.

In particular, it can be used to (re-)design and engineer the flat photonics components such as flat lens (also called metalens), flat prism, retro-reflector, and, vortex plate [21].

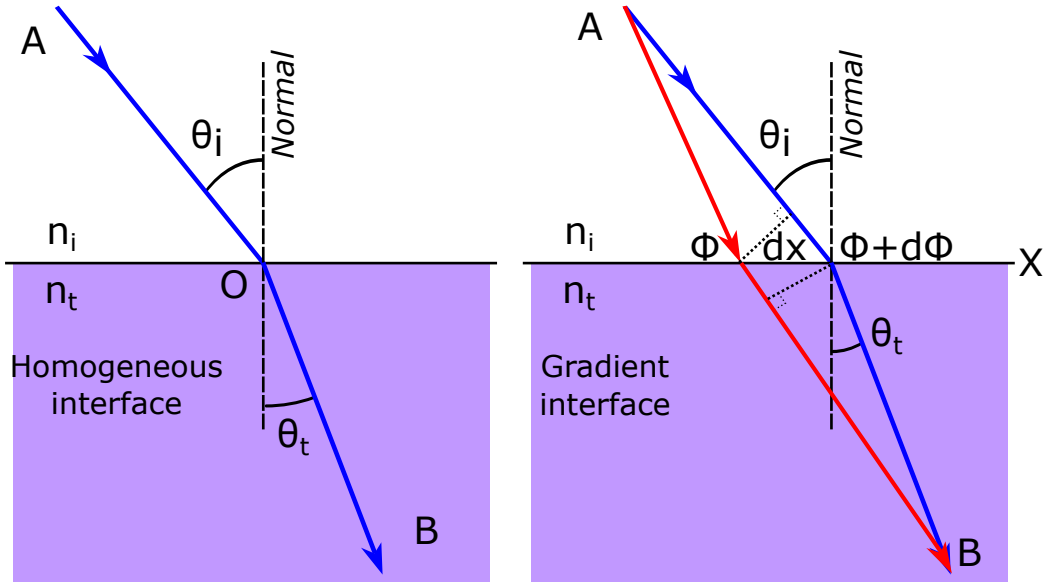

FIGURE 1.3: A comparison of standard Snell's law (left) and generalized Snell's law (right).

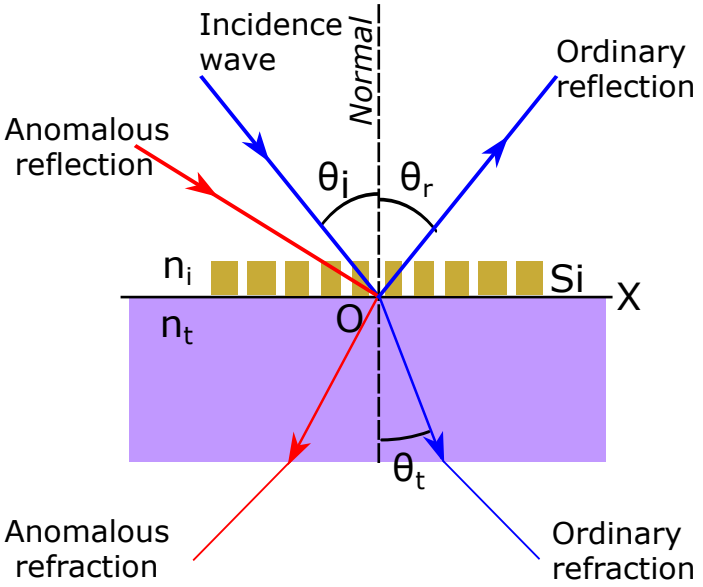

FIGURE 1.4: An ordinary and anomalous reflection and refraction of wave from metasurfaces.

A suitable phase gradient function is designed using nano-scatters to achieve the necessary phase at each point on a subwavelength scale. The nanoantennas can be designed using metals or dielectric materials [22, 23]. Different designs of nanoantennas have been proposed depending upon the applications. This issue is discussed in detail in the next sections.

1.1.1 Metasurfaces design using metallic nanoantennas

1.1.1.1 Metals basic

Metals show some specific properties at lower frequencies (in particular, below the plasma frequency). They have free charge carriers, and their properties can be described using the Drude model. According to Drude model, the permittivity of metals is given by

$$\varepsilon(\omega) = 1 - \frac{\omega_p^2}{\omega^2 + i\gamma\omega}, \tag{1.8}$$

where ω is the frequency of EM wave, $\gamma = \frac{1}{\tau}$ is the damping frequency which depends upon the relaxation time (τ) of electrons in solid, and ω_p is plasma frequency given by

$$\omega_p = \frac{Ne^2}{\epsilon_o m}, \tag{1.9}$$

where N, e and, m are the concentration, charge, and mass of the electron in metal, respectively. ϵ_o is the permittivity of the vacuum. The plasma frequency of the metals can be easily calculated based on the free carrier concentration and it is above 5 eV for most metals. So, below plasma frequency, the real part of permittivity of the metal is negative for the entire infrared and the visible range. The real and imaginary parts of permittivity of the metal are given by

$$\varepsilon_{\text{real}}(\omega) = 1 - \frac{(\omega_p\tau)^2}{1 + (\omega\tau)^2}, \tag{1.10}$$

$$\varepsilon_{\text{imag}}(\omega) = \frac{\omega_p^2\tau}{\omega\left[1 + (\omega\tau)^2\right]}. \tag{1.11}$$

The refractive index of metals is

$$n(\omega) = \sqrt{\varepsilon(\omega)} \tag{1.12}$$

and $n(\omega) = n^{'} + in^{''}$, where $n^{'}$ is a factor in the propagation constant and $n^{''}$ represents the losses in metal. Since the $\varepsilon_{\text{real}} \ll \varepsilon_{\text{imag}}$, so we can write;

$$n(\omega) \approx n^{''} = \sqrt{\frac{\varepsilon_{\text{imag}}}{2}} = \sqrt{\frac{\tau\omega_p^2}{2\omega}} \tag{1.13}$$

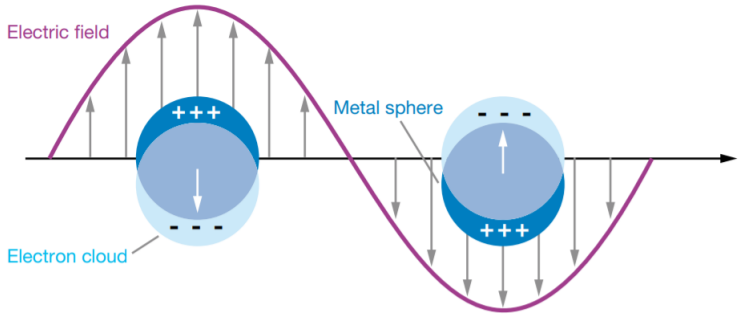

FIGURE 1.5: Localized surface plasmons on the metallic nanoscatter.

So, below plasma frequency, bulk metals are lossy and do not allow propagation of EM waves.

1.1.1.2 Surface plasmon resonance (SPR)

The interaction of a metallic nanoscatter with the incoming wave can be described within the frame of classical Maxwell theory as follows

$$\begin{aligned} J + \frac{\partial D}{\partial t} &= \nabla \times H, \\ -\frac{\partial B}{\partial t} &= \nabla \times E, \\ \nabla \cdot B &= 0, \\ \nabla \cdot D &= 0. \end{aligned} \tag{1.14}$$

The first two equations are direct consequences of Ampere's circuital law and Faraday's law where J and $\frac{\partial D}{\partial t}$ are the conduction current density and displacement current density. E, B are the electric and magnetic fields. H is the magnetic field intensity. The last two equations formalize the Gauss law for magnetic field and electric field. At the assumption of linear, isotropic and non-magnetic medium, there are additional material dependent relations given by

$$D = \varepsilon(\omega)E, \tag{1.15}$$

$$B = \mu_o H, \tag{1.16}$$

where μ_o is the permeability of the free space.

When the nanoscatter size is very small as compared to the incoming wave length, it excites the clouds of electrons on the surface of the nanoscatter. These clouds are called plasmons. A schematic representation of the incoming wave with spherical nanoscatter

is shown in Fig. 1.5. When the incoming wave with the electric field $E = E_o \exp(-i\omega t)$, interacts with free electrons of nanoscatter, it polarises the nanoscatter. If the wavelength of the incoming wave matches with the resonant condition, the electrons start to oscillate that yields surface plasmons. This frequency of oscillations is called surface plasmon frequency or surface plasmon resonance frequency ω_{sp} and is given by

$$\omega_{sp} = \frac{\omega_p}{\sqrt{1+\varepsilon_d}}, \tag{1.17}$$

where ε_d is permittivity of nanoscatter. The nanoscatter gets polarized due to electric field of the incoming wave. Polarizability (α) of the metallic nanoscatter is given by [24]:

$$\alpha = 4\pi a^3 \frac{\varepsilon_d - \varepsilon_m}{\varepsilon_d + 2\varepsilon_m}, \tag{1.18}$$

where a is the radius of the nanoscatter and ε_m is the permittivity of the surrounding media. From the above equation, it is clear that nanoscatter has strong polarizability when $\epsilon_d = -2\epsilon_m$. Since metals have a negative real part of permittivity, they can exhibit such a plasmon resonance. It is to be noted that the field is highly localized near the interface of the nanoscatter, so this regime is also referred to as localized surface plasmon resonance (LSPR). Also, the polarizability is the function of the radius of the nanoscatters, so it is possible to shift the spectral location the LSPR.

At the earlier stages of metasurface research, many designs have been based on metallic nanoantennas [25]. Metallic nanoantennas support plasmonic resonances and, hence, can introduce the phase shift when used in metasurfaces. It is to be noted that plasmonic resonances are dependent upon the size, shape, permittivity of metal and permittivity of surrounding media. So, they can be adjusted easily by selecting appropriate parameters depending upon the requirement [25]. As is known, at resonance condition, the plasmonic nanoantenna has a total phase change from 0 to π. To completely manipulate the light, we require a total phase shift from 0 to 2π. This limits the applications of plasmonic metasurfaces. As an alternative, a Berry-Pancharatnam (BP) phase [26] is combined with the plasmonic resonance phase to achieve a 2π phase shift, but that makes the device polarization sensitive. Another problem with plasmonic metasurfaces is associated with the high losses in the metals at optical frequencies. So, the efficiency of plasmonic metasurfaces is limited. The metals are highly reflective in nature, so it is possible to achieve high reflectivity by adding a thin metal layer below the nanoantenna.

Metal based metasurface has been reported with a efficiency upto 80% for holography application [27]. But it is not suitable for transmission mode devices due to high absorption. Recently a highest efficiency of 42.5% is reported in transmission mode plasmonic metasurfaces [28].

1.1.2 Metasurfaces design using dielectric nanoantennas

In the last few years, dielectric based metasurfaces become an emerging area of research to overcome the problem of plasmonic metasurfaces. The dielectric metasurfaces may have a broadband resonance at optical frequencies, and the dielectric nanoantennas have very low losses as compared to metals. The resonances associated with dielectric nanoantennas have been studied using Mie theory [29]. This theory is explained in the next section.

1.1.2.1 Mie analysis for dielectric particle

In 1908, Gustav Mie proposed a theory to predict the scattering of EM wave from a spherical dielectric particle when its size is comparable to the wavelength [29]. Mie's theory describes the scattering based on the solutions of Maxwell's equations for an EM plane wave. It allows the exact analysis only if the diameter of the spherical particle is of the order of 0.1λ to λ. If the diameter of the particle is smaller then the 0.1λ, the Mie theory converges to Rayleigh scattering theory [30]. Let us consider a spherical particle with a diameter a, which is excited by a plane wave propagating in the z-direction, as shown in Fig. 1.6. Any plane wave can be decomposed of parallel and perpendicular components. The Mie theory describes the scattered field components as a function of wavelength and scattering polar angle in the scattering plane. So, the scattered field can be decomposed into the components in the scattering plane (xz-plane). We assume here that the direction of the scattering is determined by the angle Θ, which is measured from the z-axis.

Each point of the spherical particle is treated as a dipole source which scatters the energy in space. The sum of each dipole field describes the total scattered field components. So, the scattering matrix for electric field components with respect to incoming electric

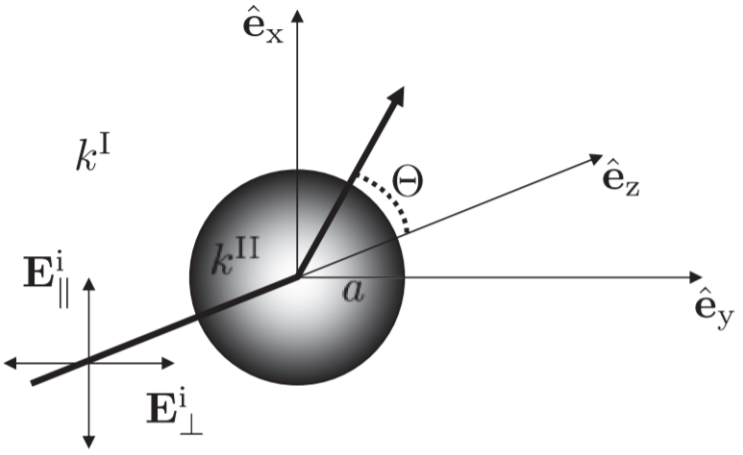

FIGURE 1.6: A spherical particle is excited by plane wave propagating in the z direction.

fields can be described as

$$\begin{bmatrix} E^s_{\parallel} \\ E^s_{\perp} \end{bmatrix} = \frac{e^{ikr+ikz}}{ikr} \begin{bmatrix} S_2(\Theta) & 0 \\ 0 & S_1(\Theta) \end{bmatrix} \begin{bmatrix} E^i_{\parallel} \\ E^i_{\perp} \end{bmatrix} \tag{1.19}$$

where $E^s_{\parallel}$ and $E^s_{\perp}$ are parallel and perpendicular components of the scattered electric field in the scatter plane xz and $E^i_{\parallel}$ and $E^i_{\perp}$ are parallel and perpendicular electric field components of the incoming wave in the scatter plane. k and r are the wave number of the incident wave in the surrounding medium and radial coordinate, respectively. The Mie theory essentially uses the multipole method and gives the sum of multipoles scatters as the coefficients of the scattering amplitude matrix, i.e., $\begin{bmatrix} S_2(\Theta) & 0 \\ 0 & S_1(\Theta) \end{bmatrix}$.

These coefficients are given by

$$S_1(x;\tilde{n};\Theta) = \sum_{n=1}^{\infty} \frac{2n+1}{n(n+1)} \left[a_n \pi_n(\Theta) + b_n \tau_n(\Theta)\right], \tag{1.20}$$

$$S_2(x;\tilde{n};\Theta) = \sum_{n=1}^{\infty} \frac{2n+1}{n(n+1)} \left[a_n \tau_n(\Theta) + b_n \pi_n(\Theta)\right], \tag{1.21}$$

where $x = 2\pi a/\lambda$, $\tilde{n}$ is the relative refractive index of the spherical particle to the medium, n is an integer that indexes an infinite series, and a_n and b_n are given by:

$$a_n = \frac{\varphi_n(x)\varphi_n'(y) - m\varphi_n'(x)\varphi_n(y)}{\zeta_n(x)\varphi_n'(y) - m\zeta_n'(x)\varphi_n(y)} \tag{1.22}$$

$$b_n = \frac{m\varphi_n(x)\varphi_n^{'}(y) - \varphi_n^{'}(x)\varphi_n(y)}{m\zeta_n(x)\varphi_n^{'}(y) - \zeta_n^{'}(x)\varphi_n(y)} \tag{1.23}$$

where φ and ζ are Ricatti-Bessel functions (the prime indicates the derivative) and $y = \tilde{n}x$. m is the complex refractive index of the particle relative to the surrounding medium. The τ_n and π_n are Legendre polynomials.

The intensity of the scattered field can be calculated as

$$i_1(x;\tilde{n};\Theta) = \left|S_1^2(\Theta)\right|, \tag{1.24}$$

$$i_2(x;\tilde{n};\Theta) = \left|S_2^2(\Theta)\right| \tag{1.25}$$

and far field intensity of the scattered field is given by

$$I_{\parallel}^s = \frac{i_1}{kr^2}E_{\parallel}^i, \tag{1.26}$$

$$I_{\perp}^s = \frac{i_2}{kr^2}E_{\perp}^i. \tag{1.27}$$

The far field spherical electric fields components in the spherical coordinate system are given by

$$E_\Theta = H_\Phi = \frac{i}{kr}e^{ikr+ikz}\cos(\phi)S_2(\Theta), \tag{1.28}$$

$$-E_\Phi = H_\Theta = \frac{i}{kr}e^{ikr+ikz}\sin(\phi)S_1(\Theta). \tag{1.29}$$

Once the scattering coefficients $S_1(\Theta)$ and $S_2(\Theta)$ are found, one can plot the radiation pattern for sphere of a given size. The scattering and extinction cross section of the spherical nanoscatters and equations are given by

$$Q^{\text{scat}} = \frac{2}{x^2}\sum_{n=1}^{\infty}(2n+1)\left(\left|a_n^2\right| + \left|b_n^2\right|\right), \tag{1.30}$$

$$Q^{\text{ext}} = \frac{2}{x^2}\sum_{n=1}^{\infty}(2n+1)\,\text{Re}\left(a_n + b_n\right). \tag{1.31}$$

When a spherical particle is excited, it stores the energy and re-radiates it into the surrounding space. During the process, some amount of energy is absorbed by the material and converted into heat. In general, the losses in the dielectric material are defined in terms of loss tangent $\tan\delta = \dfrac{\omega\varepsilon_{\text{imag}} + \sigma}{\varepsilon_{\text{real}}}$, where σ is the conductivity of dielectric, and $\varepsilon_{\text{real}}$ and $\varepsilon_{\text{imag}}$ are real and imaginary part of permittivity of the dielectric. This loss tangent is much smaller than unity ($\tan\delta \ll 1$), but it is also a function of

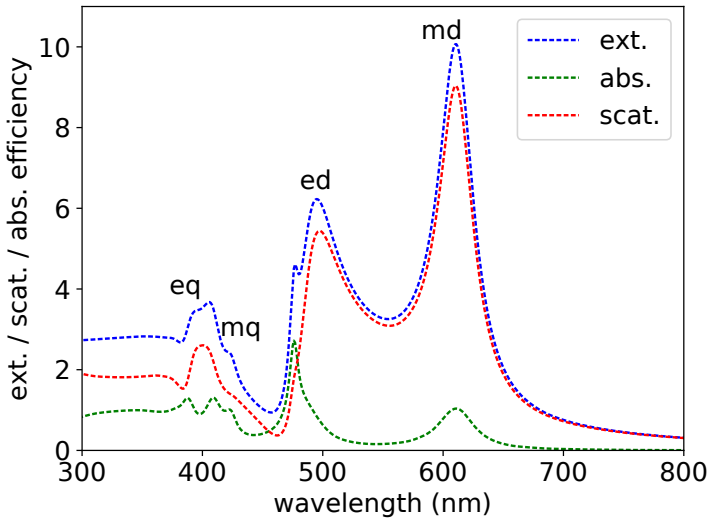

FIGURE 1.7: Mie scattering of Si nanoparticle with 140 nm size in vacuum.

size, shape and wavelength. A correct way to calculate the losses is based on the use of the absorption cross section of the particle given by

$$Q^{\text{abs}} = Q^{\text{ext}} - Q^{\text{scat}}. \tag{1.32}$$

The above introduced parameters are very useful to define the far-field characteristic of spherical particles. Here, few points must be noted. Mie analysis is exact only if the shape of the particles is spherical. Also, it is independent upon the medium and type of the material of the nanoparticles. There are many open-source platforms available to calculate the Mie coefficients [31, 32]. Here, we consider a case of Si nanoparticle with a diameter of 140 nm. The scattering efficiency and extinction coefficient are plotted in Fig. 1.7 [31].

The Mie scattering analysis is very important to understand the underlying physics of nanoparticles. It provides the inside details of the field (near field) pattern as well as scattering (far-field) behavior of a nanoparticle. Fig. 1.7 shows the two peaks in the extinction cross-section (ECS) of the Si nanoparticle. By analysis of the near field pattern (as shown in Fig. 1.8) [1], one can observe that there exist two dipolar fields associated with an electric dipole and a magnetic dipole. The first resonance (on frequency scale) arises when the incoming wavelength is of the order of the diameter of nanoparticles $\lambda_o = n_{sp} D_{sp}$, where n_{sp} is the index of refraction the nanoparticle material and D_{sp} is the diameter of the nanoparticle. This is known as magnetic dipole (md) resonance due to its specific field pattern as shown in Fig. 1.8 (b) [1]. It is worth to note, that the origin of dipolar magnetic resonance is completely different in comparison to SRR. The

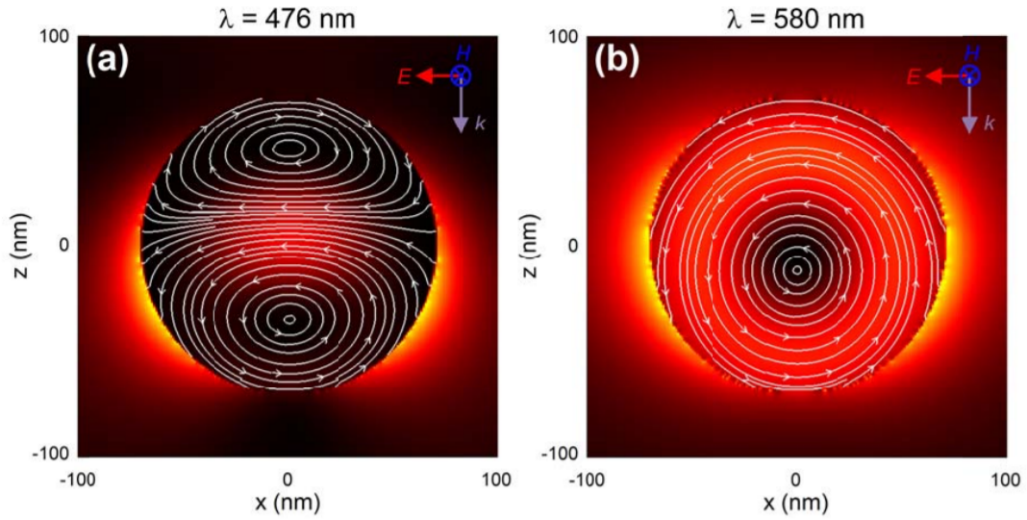

FIGURE 1.8: A spherical Si nanoparticle (140 nm in diameter embedded in silicon oxide medium) is excited by plane wave. The plot shows electric fields distribution at 476 and 580 nm in (a) the electric dipole field pattern, and (b) the magnetic dipole field pattern [1].

origin of the magnetic resonances in the dielectric nanoparticle is due to the existence of circulating electric field within the nanoparticle, while SRR has magnetic resonance due to the ring shape where oscillating electric fields create the artificial magnetic response. Since the dielectric nanoparticle supports the concentric circulating electric field within the nanoparticle, the magnetic response of dielectric nanoparticle is very strong and can be observed even in visible range [1]. The second resonance is electric dipole (ed) resonance where the electric field is concentrated on the surface of the nanoparticle. Its field pattern is shown in Fig. 1.8 (a) [1].

If we extend the spectrum of the ECS, it is observed that there exist higher-order multipole modes, see Fig.1.7 where the electric quadruple (eq) and magnetic quadruple (mq) resonances are visible at 390 and 410 nm. A systematic study of these resonances can be found in [1], see Fig. 1.9. Note that the refractive index for most practical dielectric materials at optical frequencies is very limited, being above 1 and below 3.5. For instance, at optical frequencies, silicon has highest refractive index of around 3.5. The order of the magnetic and electric dipole and quadruple resonances remains the same for a large part of the n range. The resonances peak is also function of the host medium, and resonance peak may have different spectral locations for the different media.

The Mie analysis helps to design the high-efficiency metasurfaces in transmission and reflection mode. It is possible to design the Huygens's source, which scatters the light only in the forward direction. This can be done by breaking the symmetry of nanoparticle and allow the overlapping of the electric and magnetic resonances. The forward

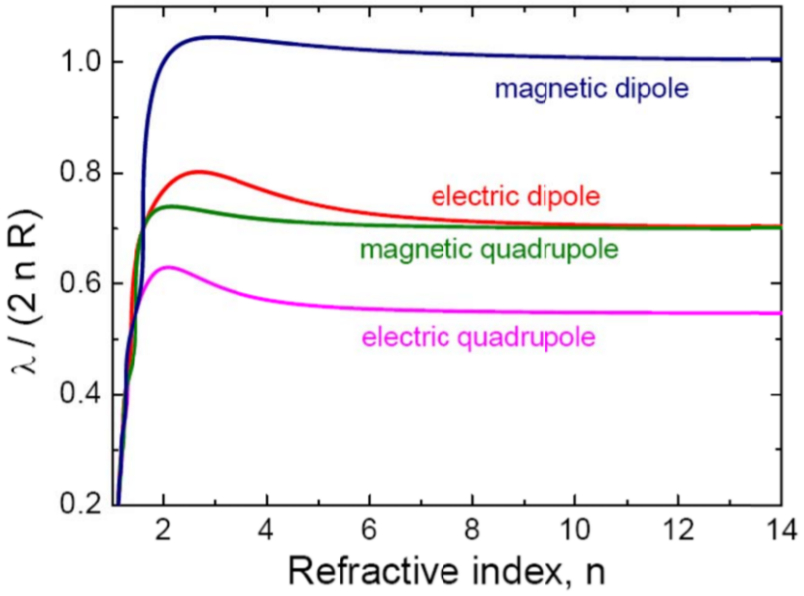

FIGURE 1.9: The sequence of occurrence of different field pattern inside the sphere [1].

scattering of two dipolar modes is sum up due to in-phase radiation pattern, and backward scattering is cancelled due to out of phase radiation pattern and results in nearly unity transmission with a total phase shift of 2π [33]. The process of back-scattering cancellation is known as Kerker effect [34]. This makes the dielectric nanoresonators a potential candidate to design high efficiency transmitting metasurfaces [35, 36]. The simplest possible structure to design the Huygens's source is a cylindrical shape, where the diameter and height of the nanocylinder are tuned to overlap the electric and magnetic dipole modes [36]. There are also several other designs which have been proposed to achieve high-efficiency transmitting metasurfaces [37].

If the size of the dielectric nanoparticles is comparable with respect to the incoming wavelength of the wave, one can excite the hybrid Mie Fabry-Perot modes. By proper optimization of hybrid modes, one can achieve near unity transmission [38, 39]. The different shapes of dielectric nanoparticles give an additional degree of freedom to excite complex resonances. By proper optimization of the resonance, one can achieve high efficiency in transmission mode, as well as in reflection mode. An extra degree of freedom can be added by using non-symmetric shapes of nanoparticles, which can excite individual resonances for each state of linear polarisation. One can excite also multi-modes for each state of polarization and combine them to achieve high-efficiency broadband resonances [40, 41].

1.2 Modelling of metasurfaces

It should be noted from equation 1.3 that the phase gradient across the interface has to be a continuous and slowly varying function to satisfy the generalized Snell's law. In practice, this is difficult to achieve, so the phase gradient is introduced by discretization of the interface at the subwavelength scale using nanoantennas. Since it involves the phase modification approach at the subwavelength scale, a ray-tracing method cannot be accurate due to interference and diffraction of the waves. One should solve the full wave Maxwell's equations to achieve an accurate analysis of metasurfaces. There are different methods to solve Maxwell's equations [42, 43]. Each method has its own advantages and disadvantages, but the end analysis should be the same, i.e., it is always carried out in terms of electric and magnetic fields. The discussion of different methods for solving wave equations is beyond the scope of this thesis. In most cases, a finite difference time domain (FDTD) solver can be used for metasurfaces design and analysis. FDTD method shows reasonable accuracy when compared to experimental results. It should be noted, that there are other methods available that can do exactly the same analysis as FDTD can. So, the choice of methods is arbitrary and one can choose any method for metasurface analysis, depending upon the resources and availability of the software.

In this thesis, I have used a commercially available Lumerical FDTD solver for metasurface design. Lumerical FDTD solver interface is very user-friendly and easy to calculate most of the parameters using inbuilt standard functions. The inbuilt analysis group can be used for additional post-processing calculations, such as extinction cross-section or quality factor. The FDTD methods discretize the structure in the rectangular grid and calculate the fields (electric and magnetic) using iterative methods based on given boundary conditions. The user has full control over the mesh grid to adjust the accuracy and simulation time. It is always recommended to perform a convergence test to achieve reasonable accuracy by adjusting the mesh size and simulation time. Additional help and support information is available on the webpage [44].

1.3 Purpose of the Thesis

The purpose of this work is to develop a new way of design and fabrication of all-dielectric metasurface based devices. There are already a bunch of groups that have presented different applications of metasurfaces. I began my research work with one

of the key areas of color filters design for display applications. Although the details of the motivation of color filter devices are discussed in Chapter 2, my main motivation to select the color filters applications is because of direct implementation of metasurfaces in advanced display devices.

In the past, most of the color filter design and research was related to plasmonic based color filters [45]. A very little attention was given on all-dielectric color filters [46, 47]. My goal was to improve the performance of color filters and make it suitable for integration with on-chip silicon platform. So, I decided to look for the possibilities for silicon-based high-efficiency all-dielectric color filters. It is well known, that silicon is moderately lossy in the visible range. So, the goal was to engineer the resonances of the silicon nanoparticles to achieve high-efficiency wide gamut color filters. As discussed in Sec. 1.2, the resonances of the dielectric nanoresonator can be tuned at visible wavelength by selecting appropriate dimensions and geometry. We proposed to use a cross-shaped silicon nanoresonator to overlap the electric and magnetic resonances in the visible range, to achieve high efficiency. This will be discussed in Chapter 3.

Another important aspect of color filter design is to achieve a tunable response. Once we fabricate the all-dielectric based color filters, ideally one cannot change the response of the color filters, since it depends on the size and refractive index of the nanoresonator material. So, this is another key topic, to design tunable color filters. We proposed to use the non-symmetric nanoresonator design to achieve polarization tunable color filters. Since the dielectric nanoresonators have highly confined mode within the nanoresonators, it is possible to confine the energy for two different states of polarization within a non-symmetric nanoresonator. The details are discussed in Chapter 4.

Although, the polarization tunable color filters are interesting, the above-mentioned method has two important limitations. First of all, it requires a polarization-dependent source to achieve a tunable response, which may not be possible for all cases. Also, there is no way to dynamically tune the response to a wide range of colors. Therefore, an alternative approach is required to tune the response. In Chapter 5, we propose to use a liquid crystal integrated with an aluminum nanograting to achieve the voltage tunable color filters. The liquid crystal's index of refraction is anisotropic and can be tuned by applying electric field. When an aluminum-based grating is sandwiched within the liquid crystal, it changes the response in the presence of external biasing voltage. This is discussed in chapter 5.

The concept of the metasurfaces is very general and has been used to design various optical components. In particular, metasurfaces have been exploited to design light guiding components, i.e., metalens, hologram, as well as, waveguide and mode converters [2, 48]. So, I extended my research to demonstrate the guiding of light in a specific area of photonic crystal slab (PhC) by modifying surface impedance using metasurface. This is described in Chapter 6.

1.4 Thesis Outline

Since a major part of the thesis involves the design analysis and fabrication of color filters devices, it is important to understand their working principle, functionality and importance in a digital imaging system. Chapter 2 presents a brief introduction, working principles, and the importance of color filters in the digital imaging system. It also explains the advantage of dielectric nanoantennas based color filter design.

Chapter 3 is dedicated to the silicon nanoantennas based color filter design. The cross-shaped nanoantennas design is proposed. The main goal was to design color filters with high efficiency and extended gamut on CIE 1934 chart. The idea was proposed by prof. R. Hedge based on his previous work of the metallic nanoantenna printing beyond the diffraction limit [49]. I performed simulation and optimization of the nanoantennas geometry using Lumerical FDTD solver. The final design was fabricated at IIT Bombay, India, where Gayatri Vaidya was involved to perform electron beam lithography (EBL). Finally, I did the measurements and validated the results of simulations. The manuscript was written based on the discussions with Prof. R. Hedge, Dr. A. Serebryannikov (co-supervisor), and Prof. M. Krawczyk (supervisor). We also discuss the manuscript with Prof. Nicolas Bonod, who is a world recognized expert in the area of metasurfaces. The chapter is published in the ACS Photonics [50].

Chapter 4 is the extension of the work of Chapter 3 to design tunable color filters. We used asymmetric nanoantennas based design approach therein. I performed the FDTD simulations using Lumerical for design and optimization. The device was fabricated at CEN laboratory, IIT Bombay, India. Gayatri Vaidya wrote the mask using EBL. I performed measurements with the aid of a polarization tunable optical microscope to validate the results. The results were discussed and analysed by my co-supervisor and supervisor. Dr. Pawel Gruszecki helps me to plot visualize the data using Python. The manuscript was reviewed by all co-authors and published in Scientific Reports [51].

Chapter 5 is the outcome of my research visit to Taiwan. This research was done in Prof. Chen's group at NCTU Taiwan University during my 4 months visit under NCTU elite internship program. The goal of this research was to design electrically tunable color filters. The integration of color filters with a liquid crystal (LC) was proposed to achieve tunable color filters. A low voltage (less than 5 volts) was used to tune the response of the color filters. The idea was proposed by Prof. Chen. The color filter was designed and simulated by Mr. Zu-Wen Xie, I was involved in the optimization of design and results analysis. The device was fabricated by Mr. Zu-Wen Xie with the help of Dr. Jhen-Hong Yang. Prof. Lee helps us to understand the working principle and use of liquid crystal (LC). The chapter is published in Optics Express [52].

Chapter 6 is dedicated to another new application of metasurfaces, it is control of the propagation of light using surface impedance modification. In this chapter, a photonic crystal waveguide is designed using high index silicon nanorods. The rods in the waveguide are covered with thin metal caps, playing a role of metasurface. The light bending and channeling is achieved in a volume-mode regime by just modifying the surface of the photonic waveguide. The idea was proposed by Dr. A. Serebryannikov. I performed the FDTD simulation to design the photonic crystal waveguide, contribute to the result analysis and writing the manuscript. The chapter is published in Optics Letters [53].

The last chapter is the summary and outlook of the work done in this thesis with the concluding remarks. It also presents a future possible direction work based on this thesis.

Chapter 2

Introduction to Color Filters

A pixel [54] is a fundamental unit of an imaging system and photodetectors are the key components of a pixel. The physical size of the photodetector decides the size of pixel and that, in turn, decides the resolution of any digital imaging system. Generally, photodetectors are solid state semiconductor devices which detect the intensities of light almost insensitive to the wavelength. Photodetectors usually represent a complementary metal oxide semiconductor (CMOS) sensor which converts the photons into an electrical signal that, in turn, determines the intensity of light. The fundamental size of the pixel is decided by the physical size of the photodetector. With the development of new fabrication techniques, it becomes possible to achieve the significantly small size of photodetector but still the pixel resolution is limited to microns size.

The reason for pixel size limit is another important device which is placed on top of the photodetector, so-called color filter array (CFA). Since the photodetectors are almost insensitive to wavelength, the CFA is used to separate the intensity of color. The CFA design was first proposed by Bryce Bayer, an American scientist work with Kodak company. In 1976, Bryce Bayer used twice as many green elements as red or blue to mimic the physiology of the human eye, since human eyes are more sensitive to green color. This pattern arrangement is known as a Bayer filter (also known as RGB filter) [55] shown in Fig. 2.1. It consists of a repeated pattern of one red, one blue and two green filters. When white light passed through the Bayer filter, the photodetectors

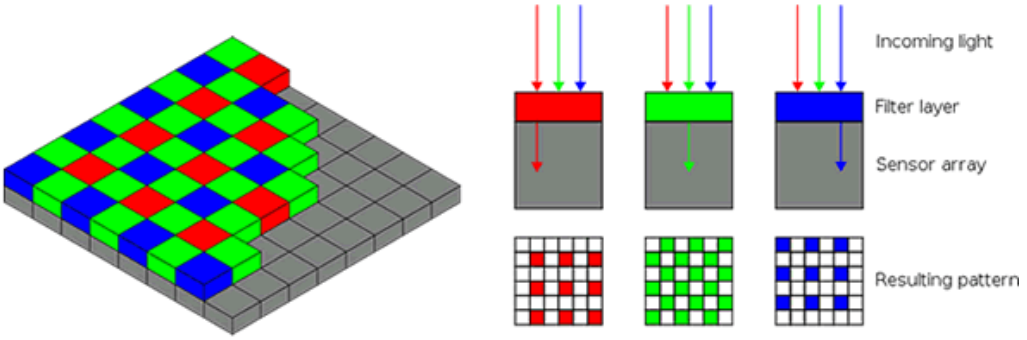

FIGURE 2.1: Bayer (RGB) color filter on the left. Right side shows the schematic operation of Bayer filter with photodetector (sensors).

detect the individual intensity of red, green, and blue light. The raw output of Bayer-filter cameras is referred to as a Bayer pattern image. The raw image data captured by the image sensor is then converted to a full-color image (with intensities of all three primary colors represented at each pixel) by a demosaicing algorithm which is tailored for each type of color filter. It should be noted that this color signal represented by the photodetector is not what human eyes sees. The converted signal of RGB intensities is further processed according to chromaticity matching function to match with human vision.

The CFA is aligned on top of the photodetectors, so that each photodetector only receives light with a predefined wavelength of the filters with no crosstalk. The minimum resolution of the pixel is decided by the resolution of the CFA. The CFA is made of pigment photoresist material [56, 57]. These materials are usually polymer, which are a few microns thick, absorb some visible spectrum, and allow a range of wavelengths to reach to CMOS sensor as shown in Fig. 2.1. Although the polymers provide a high quality of separation between the colors, the pigment based color filters suffer of many problems. It should be noted, that the absorption of the CFA is dependent upon the polymer material and its thickness. Since polymers are not compatible with the CMOS fabrication process flow, the CMOS sensors and CFA are fabricated separately, and it requires an additional aligner process. The CFA is aligned with the CMOS sensors, so that each photodetector receives light with a specific wavelength with almost no cross-talk. The process of alignment becomes even more complicated when the pixel resolution is very high, i.e., individual pixel size is very small. This imposes a secondary fundamental limit on pixel resolution. In addition to this problem, CFAs also increase the overall size of the display system. In order to absorb the light, the thickness of the polymer is of the order of microns depending upon the materials.

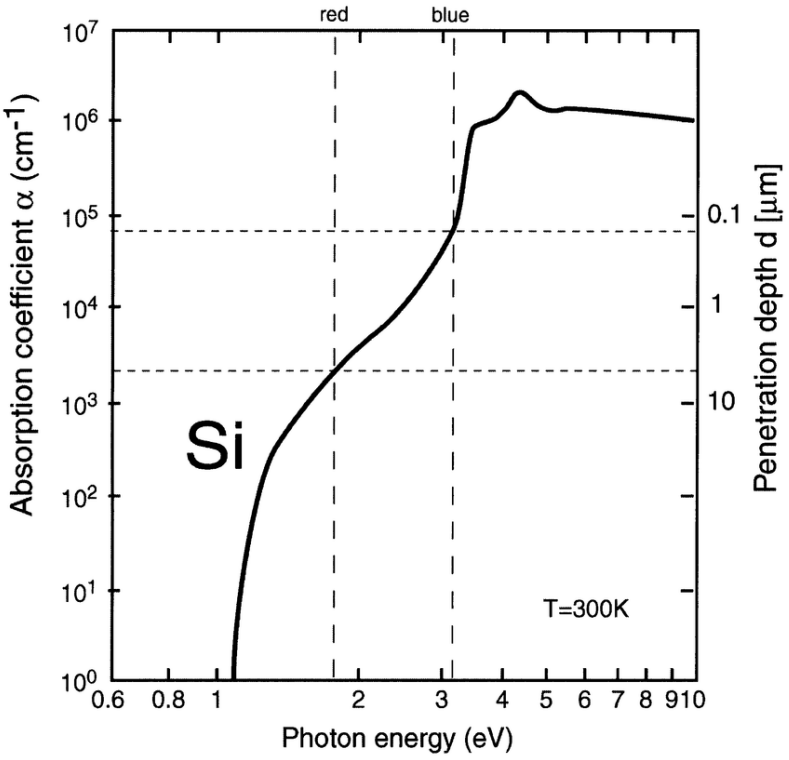

FIGURE 2.2: The absorption coefficient of Si wafer for different depth of penetration [60].

In addition, polymers degrade over time, so one should keep replacing the filters from time to time to maintain a good quality of the detector. Moreover, the pigment-based dyes are not environment friendly, so it is not easy to recycle them. New materials have been proposed to solve the problem of CFAs and pixel resolution has improved significantly over the years, but the fundamental problem of CFA alignment and large thickness is still an open problem of research.

An alternate solution to the problem of CFA resolution is addressed by the Foveon X3 sensor [58] designed by Foveon, Inc. [59][a] and manufactured by Dongbu Electronics. In this sensor, three photodiodes are vertically stacked on a silicon wafer. It is possible due to different wavelengths of light penetrating into silicon at different depths. The absorption of Si with respect to penetration depth is shown in Fig 2.2 [60]. Each of the three stacked photodiodes stacked on a Si wafer respond to different wavelengths of light. Finally, post-processing is done based on the absorption of the light by each photodiode. Comparison of Foveon X3 sensor based filter with CFA is shown in Fig. 2.3.

Despite the fact that Foveon X3 increases the true resolution of an imaging system and provides a solution for pigment based dyes, the main challenge of miniaturizing an imaging system is still an issue. This is because the absorption of Foveon X3 sensor

[a]Now a part of Sigma Corporation.

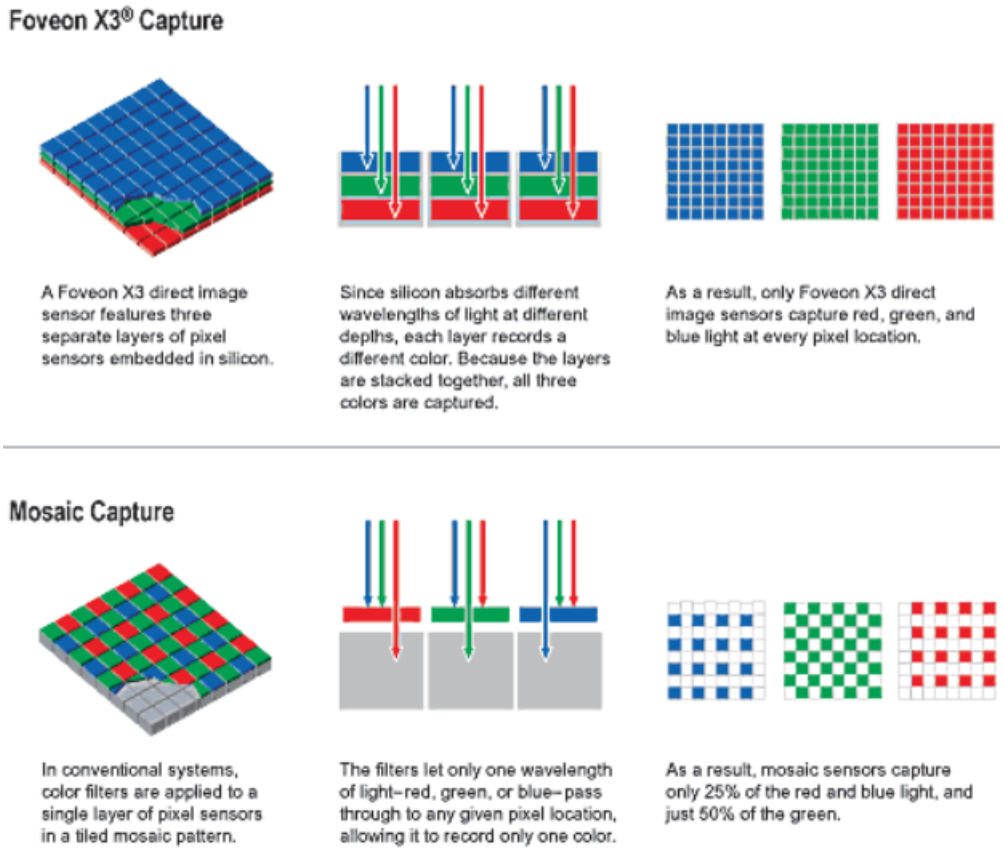

FIGURE 2.3: Comparison of Foveon X3 based color filter with CFA. [Image courtesy: Foveon, Inc.]

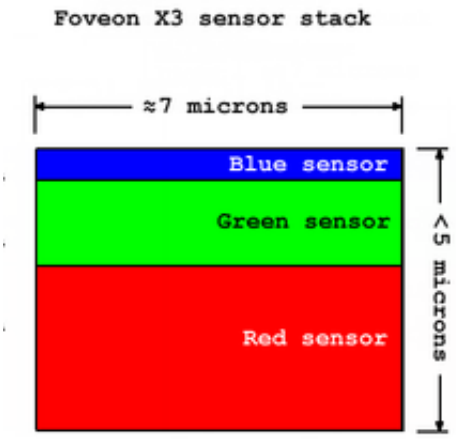

FIGURE 2.4: Thickness of Foveon X3 based color filter imaging system. [Image courtesy:Foveon, Inc.]

is dependent upon the absorption of Si wafer in visible range. So, the thickness of the Foveon X3 based imaging system is of the order of few microns as shown in Fig. 2.4.

Another way to design color filters is to use structural resonances. Structural resonances occur due to the interplay of light interaction with the tiny structure. This concept is inspired by the colors that exist in nature. When the tiny structure is arranged in

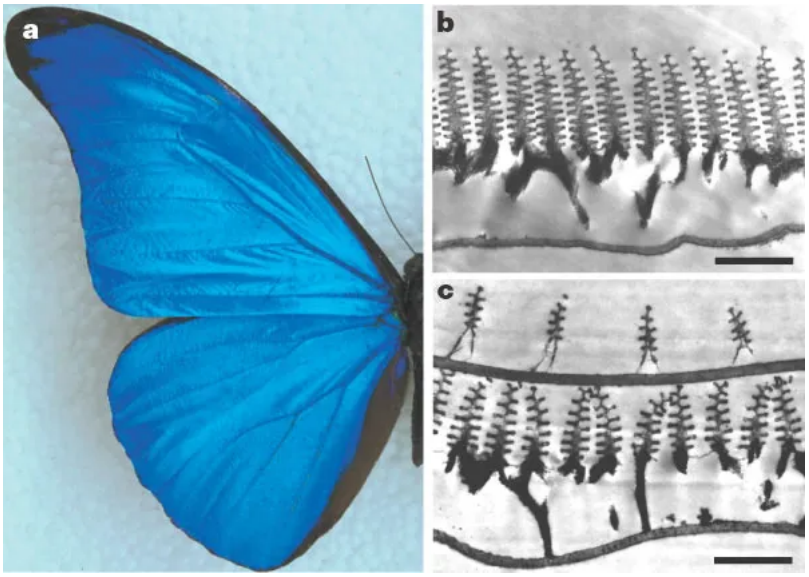

FIGURE 2.5: Real color image of the blue iridescence from a Morpho rhetenor wing [61].

a periodic fashion, it results in reflection at specific wavelength due to light-matter interaction. Structural color resonances have been found in nature and attempts have been made to reproduce them artificially. Figure 2.5 shows the periodic arrangement of tiny nanostructure arrange on a butterfly wing, which results in beautiful color [61]. Interestingly, Newton also predicted the colors of peacock feathers as due to the thin-film interference [62].

The structural colors were artificially produced using nanoparticles already in the ancient time. The Lycurgus cup by Roman glassworkers in the 4^{th} century is an interesting example. When the light illuminates it from inside and outside, it shows the two different colors due to the interaction of light with gold nanoparticles [63]. The main limitation of the structural color is the resolution. The structural colors are limited with the resolution of the order of wavelength.

Plasmonic color filters suggest a way to achieve resolution even below the diffraction limit. The plasmons are strongly localized within the metal layers and strongly interact with the light. It is also possible to localize the plasmons within the nanoparticles placed on the surfaces, if the size of the nanoparticle is of the order of the incoming wave length. In this case, localized surface plasmons polariton can appear. Plasmonic CFAs are designed using the tiny nanoantennas which interact with the incoming light. Localized surface plasmons are excited at the surface of the nanostructure and result in reflection at wavelengths corresponding to particular colors. Interestingly, plasmon resonances can be tailored by changing the geometry of nanoantenna [64]. Different materials and designs have been proposed for color filters which use the effects of surface plasmons.

In some studies, the color printing with the resolution even below the diffraction limit has been proposed [49]. Nevertheless, there is one problem with plasmonic color filters, which occurs due to high losses in metals. As already discussed in Chapter 1, metals are significantly lossy at optical frequencies and thus limit the efficiency of color filters, and allow the filtering only in reflection mode.

In the recent years, dielectric materials are considered as the emerging materials for optical devices. They have low loss compared to metals at optical frequencies. So they can be used to design high-efficiency color filters in reflection, as well as transmission mode. Dielectric based CFA are easily compatible with CMOS fabrication process flow. This is a key area of research in optics to design color filters using nanoantennas, which can be used to replace the pigment-based CFA in the future.

In the subsequent Chapters 3, 4, and 5, the different methods of designing the CFA using dielectric nanoantennas will be discussed. In Chapters 3 and 4, we discuss the methodology of designing all-dielectric color filters based on Si nanoantennas. In Chapter 5, we discuss the tunable color filters, in which an aluminum grating is integrated with a liquid crystal.

Chapter 3

All-Dielectric Metasurfaces Color Pixels with Extended Gamut*

Printing technology based on plasmonic structures has many advantages over pigment based color printing such as high resolution, ultra-compact size and low power consumption. However, due to high losses and broad resonance behavior of metals in the visible spectrum, it becomes challenging to produce well-defined colors. Here, we investigate cross-shaped dielectric nanoresonators which enable high quality resonance in the visible spectral regime and, hence, high quality colors. We numerically predict and experimentally demonstrate that the proposed all-dielectric nanostructures exhibit high quality colors with selective wavelengths, in particular, due to lower losses as compared to metal based plasmonic filters. This results in fundamental colors (RGB) with high hue and saturation. We further show that a large gamut of colors can be achieved by selecting the appropriate length and width of individual Si nanoantennas. Moreover, the proposed all-dielectric metasurface based color filters can be integrated with the well matured fabrication technology of electronic devices.

3.1 Introduction

With tremendous changes in nanotechnology over past few decades, it becomes possible to fabricate devices which promise to revolutionize many areas. Examples include

*This chapter is published in ACS Photonics [50]

ultra-thin planar lens [2, 65], optical sensing [66, 67], photo-voltaic devices [68, 69], non-fading colors [70], and various holography based devices [71, 72]. In particular, color pixels using nanoparticles have gained significant attention in recent years because of several advantages over pigment based color printing techniques like high resolution [73], high contrast, everlasting colors, significant low power consumption, and recyclability of product [74]. The concept of structural color printing is inspired by observations in nature, such as morpho butterflies, beetles, and the feathers of peacocks [75–78]. However, these colors are highly sensitive to the variations in the angle of incidence, shape, and size of the nanostructure. To make this plasmonics based structural technology more mature, its angle dependency [79, 80], sensitivity to polarization, and ease of fabrication must be taken into account. In recent years, many efforts have been done to study the aforementioned issue in plasmonic color printing [49, 81–88]. Earlier, the most commonly used materials for plasmonic nanostructure based pixels have been gold and silver [89, 90]. Gold has interband transition in the lower visible regime [89], while silver is suitable for the entire visible range but is susceptible with the native oxide that spoils the stability of colors. Moreover, gold and silver are not economical for large scale integration. Aluminum is probably the most prominent candidate [91]. It is more robust and economical for large-scale fabrication [70]. However, it shows lower quality (*i.e.*, broader) resonance in the visible spectrum than gold or silver, especially at 800nm wavelength, where interband transition takes place. Ultimately, all these metal based plasmonic devices show significant losses within the visible spectrum.

On the other hand, all-dielectric metasurfaces can be a promising solution with significant advantages over metallic nanostructures such as high quality resonances and low intrinsic ohmic losses [33, 92–99]. Silicon based all-dielectric devices have been reported for local manipulation by wavefronts, such as beam diversion, vortex plates and light focusing using meta-lenses [33, 37, 38, 100, 101]. The advantages of Si nanodisks are high refractive index and ease of fabrication with well established CMOS technology. Interestingly, the high refractive index allows to manipulate by magnetic and electric components of light simultaneously. In the case of metal based nanoantennas, absorption losses can be significant at visible spectrum, while interaction with magnetic component of the incident beam requires more complex shapes. Recently, an investigation has been conducted to demonstrate the possibility of using silicon-aluminum hybrid nanodisks [102, 103] to create colors of high quality. Silicon nanoparticles were proposed as a valuable alternative to plasmonic nanoantennae for the design of color

pixels [46, 47, 99, 104]. However, the potential of all-dielectric resonance structures is presently very far from being fully estimated and exploited.

In this work, we propose a systematic approach to build color filters by using advantages of cross-shaped Si nanoresonators, which are closely spaced to each other to create a metasurface. Recently reported numerical studies of the nanocross geometry [99] have indicated that a broader gamut of colors is possible in comparison to simpler shapes like the cylinder (disk). The main goal is to obtain a high quality (narrow) resonance throughout the visible spectrum that enables an extended gamut with colors of high purity. It is known that Si nanostructures of different shapes typically offer an opportunity to excite individual electric type and magnetic type Mie resonances, or both resonances simultaneously [1]. In fact, it has been demonstrated that by tuning the aspect ratio carefully, one can overlap both resonances to achieve near unity transmission [100]. In this paper, the all-dielectric metasurfaces are used in reflection mode. A very confined energy is concentrated within the structure due to the high quality of the used Mie resonances.

The main hypothesis that we follow here is based on the expectation that a proper manipulation by the selected Mie resonances may enable desired improvements of the resulting resonance quality owing to better confinement of resonance fields and, simultaneously, removal of secondary (unwanted) spectral features, so that enrichment of colors can be achieved. We decided in favor of cross-shaped Si nanoresonators as building elements, which are expected to be suitable [99] for achievement of the goals of this study. Each of them is made of two identical orthogonal rectangle-shaped Si nanoantennas. In this case, resonances are governed by cross-shaped nanoantennas and thus, colors can be controlled *via* all three geometrical parameters of individual nanoantennas. This gives a new degree of freedom as compared to the nanodisks, that is highly demanded for efficient optimization. Using the suggested approach, we predict by simulations and confirm experimentally that one can easily achieve a high quality resonance for the entire visible spectrum by carefully choosing the length and width of the cross-shaped nanoresonators.

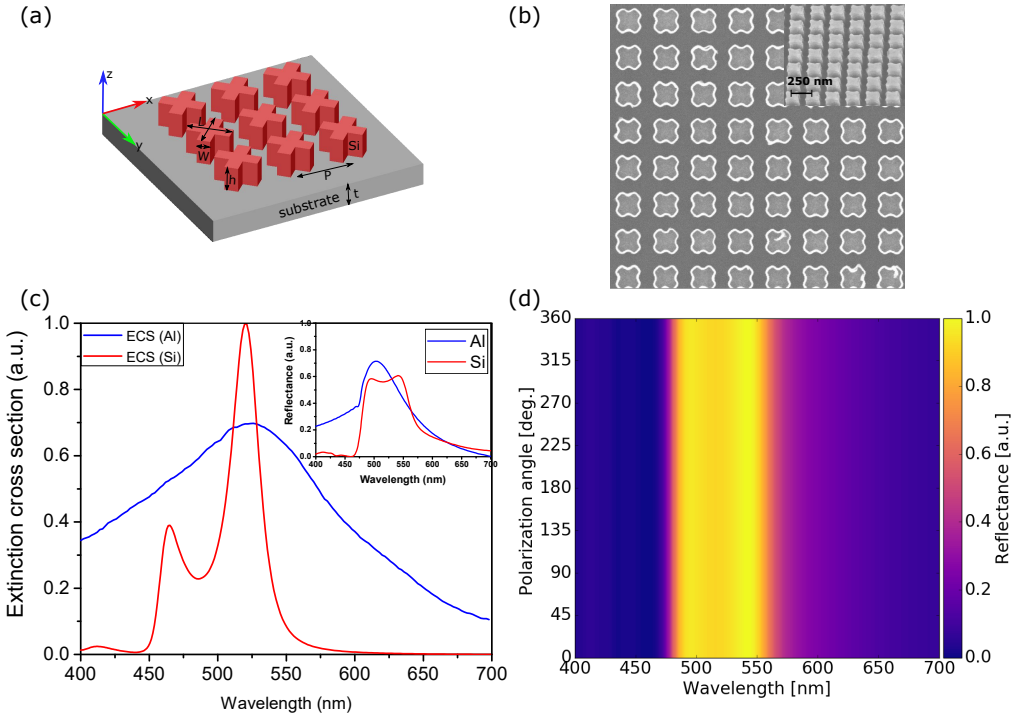

FIGURE 3.1: **Perspective view and SEM images of the all-dielectric metasurface, extinction cross section (ECS) spectra and reflectance spectra, and reflectance *vs* polarization angle.** (a) Schematic representation of the array of cross-shaped Si nanoresonators on top of the quartz substrate. The thickness of the substrate $t = 275\mu$m. For each nanoantenna, height $h = 140$nm, length L and width W are scaled to achieve different colors. The center-to-center distance between the two nanoresonators (lattice constant) is $P = 250$nm. (b) Top view of SEM images of the fabricated structure with $P = 250$nm. A 45° cross section view is added in the inset. (c) ECS spectra in case of Si and Al nanoantennae. Two peaks arising in the former case are due to electric type and magnetic type resonance (see supplementary information for the field patterns), while there is only single broad resonance in the latter case. The inset shows the reflectance spectra for the same two structures. The length, width and height are 100nm, 50nm and 140nm, respectively. (d) A colormap of simulated reflectance spectra of the Si based metasurface at polarization angle varied from 0° to 360°.

3.2 Results

Let us start from the general geometry and basic operation principles of the proposed devices. Figure 3.1(a) presents the perspective view of the proposed all-dielectric metasurface together with some details of geometry. The cross-shaped Si nanoresonators are deposited on top of the quartz substrate (see Methods of fabrication). The height of nanoantennae is selected as 140nm (in subwavelength range). Figure 3.1(b) represents the top view of SEM image of the device. A 45° cross section view is also added in the inset for the same fabricated device. For the studied Si structure, extinction cross section spectrum is presented in Fig. 3.1(c). Two resonance peaks are observed at 465nm and 520nm. They can be tuned throughout the visible range by changing the length-to-width aspect ratio of individual rectangle-shaped nanoantennas. The Si nanoresonator

dimensions have been optimized to excite these two resonances as close as possible but without a full overlapping. In addition, the criterium of minimizing unwanted spectral features has been applied in order to obtain more gradual behavior in the working spectral range. As follows from the obtained simulation results, optimization yields a resonance range that is narrower and, thus, corresponds to a resonance of higher quality, as compared to the case of Al cross-shaped nanoantennae, see Fig. 3.1(c). We have also compared the simulated reflectance spectra for the metal and Si based structures at the same dimensions [see Fig. 3.1(c), inset]. These results confirm that the metal nanostructure features broader resonances than the engineered Si one. An important advantage of cross-shaped nanoantennae is that they preserve the polarization independence. As an example, Fig. 3.1(d) presents the simulated reflectance spectrum for the entire range of polarization angle variation and entire wavelength range considered. The obtained results confirm that there is no change in the reflectance spectrum when the polarization angle is varied.

Since a specific color results from resonant interaction of light with nanoresonators, it can be obtained from adjustment of geometrical parameters that properly affect spectral locations and properties of Mie resonances. The possibility of obtaining multiple colors with the aid of metasurfaces like that in Fig. 3.1(a) and (b) is demonstrated in Fig. 3.2. The length and width of rectangle-shaped Si nanoantennae are simultaneously linearly scaled in order to tune the electric and magnetic type resonances in the entire visible spectrum from 400nm to 700nm, as shown in Fig. 3.2(a) for $P = 250$nm. A commercial-grade simulator based on the finite-difference time-domain method [44] is used to perform the calculations. They are conducted for a unit cell with periodic boundary conditions, and varied lattice constant from 250nm to 350nm, by keeping the periodicity in the subwavelength range (see Methods, Simulation). Each spectral zone in Fig. 3.2(a) corresponds to a specific color. It is clearly seen that the electric and magnetic type resonances can be tuned through the entire visible wavelength spectrum, as desired. Conversion of reflectance spectra into colors on CIE1931 chromaticity diagram can be performed, in the general case, by using an open source Python program [105]. The results of conversion of the spectra shown in Fig. 3.2(a) are presented in Fig. 3.2(b). Generally, a higher quality of resonances corresponds to a better approaching to the boundaries of the chromaticity diagram and, hence, enable higher quality and wider gamut of colors. Complete details about color visualization using reflectance spectra are given in supplementary information under section color representation from reflectance spectra.

By operating the metasurface in reflection mode, a broad spectrum of colors for highly selective wavelengths (*i.e.*, high quality colors) can be obtained. In principle, colors can be generated by using either additive or subtractive approach [106]. Here, we have used the additive approach. Ideally, the reflection spectrum must be as narrow as possible in order to generate a very specific color. A narrower resonance represents a more specific wavelength color, whereas the amplitude of the peak decides the saturation level of the color. With the aid of high quality narrow resonances, we improve the approaching to the boundaries of CIE-1931 chromaticity diagram, so a color of higher quality and a wider gamut of colors can be obtained, as desired. We experimentally found that different colors can be obtained at different values of period (P, lattice constant), which correspond to the scaled length (L) and width (W) of the nanoantenna, see Fig. 3.2(c). Each square in Fig. 3.2(c) corresponds to a unique set of geometrical parameters. The lowest series of the squares shown here corresponds to the structures, for which reflectance spectra are presented in Fig. 3.2(a). Thus, the resonance region corresponds to different colors at different values of P, see Fig. S4 in supplementary information. This dependence occurs owing to the coupling of resonance fields of nanoresonators. The use of larger values of P allows us to create a richer variety of colors, as we have more choices to increase the length and width. We have observed different colors under optical microscope due to variations in lattice constant (P) from 250nm to 350nm, see Fig. 3.2(c). The lattice constant was increased here by a reasonable increment of 20nm to make it feasible for fabrication process. Although it might be hard to distinguish between the highly saturated colors in Fig. 3.2(c), the reflectance spectra in Fig. 3.2(a) and the corresponding CIE-1931 chromaticity diagram in Fig. 3.2(b) give us a clear picture about it. In fact, a color gamut can be possible by making a matrix between the scaled lengths and widths.

The fact that two resonances, which are observed in Fig. 3.2(a) at different values of L and W, are closely spaced makes fabrication of a particular color possible, that is unlikely in case of metal based plasmonic structures, because they show a broad resonance. Moreover, it is possible to create a selective wavelength color due to sharp resonances, particularly in the lower part of the visible spectrum. It is observed in Fig. 3.2(a) that as we increase the size of cross-shaped resonators some additional Mie resonances are also excited, in coincidence with the predictions based on the simulation results. These resonances reduce the hue and saturation of red color, because of mixing contribution of different frequencies. So the red color seems to be the most difficult one to fabricate. Below, we will show that in spite of the above-mentioned difficulties the suggested structure allows us creating fairly red colors by carefully adjusting the values of P, L, and

W. Thanks to this adjustment, the unwanted effect of higher-order resonances can be minimized.

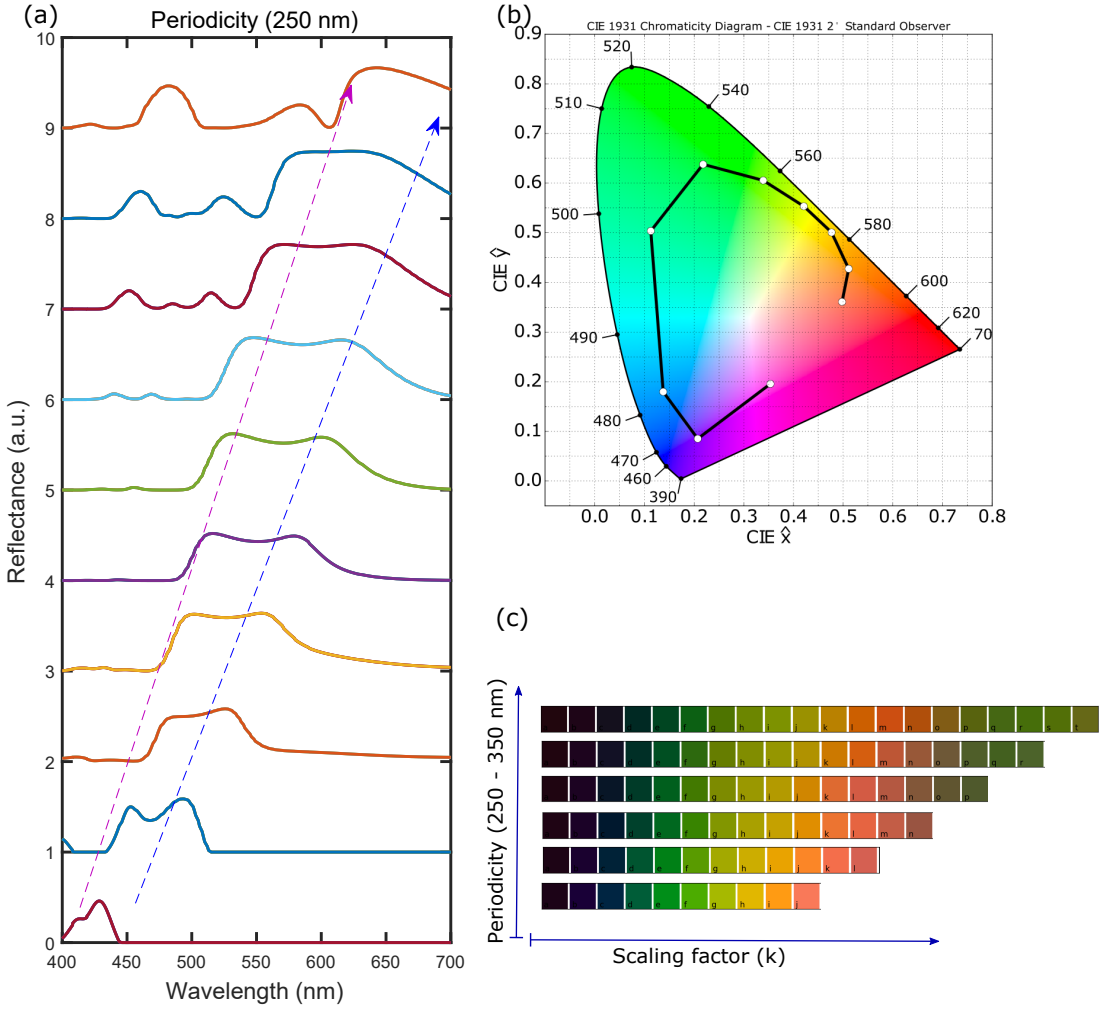

FIGURE 3.2: **Reflectance spectra (simulation), corresponding chromaticity diagram, and photograph of experimental images of the array visible under optical microscope.** (a) Unit-cell simulation results for cross shaped Si nanoresonators on quartz substrate; the initial values of geometrical parameters are $L = 65$nm, $W = 35$nm, and $P = 250$nm. L and W are linearly scaled from 65nm to 195nm and 35nm to 105nm, respectively, from bottom to top. The resonances are redshifted in the visible regime, as schematically shown by arrows. (b) Representation of reflectance spectra on standard CIE 1931 chromaticity diagram for $P = 250$nm. (c) Experimental colors visible under optical microscope for different values of P which are varied from 250nm (the lowest series) to 350nm (the most upper series) with step of 20nm (from the lowest series to the most upper one); L and W are linearly scaled from 65nm to 260nm and 35nm to 140nm, respectively; with $k = L/\min(L) = W/\min(W)$.

The three primary colors (RGB) represent the fundamental unit for color printing technology. All the other colors in the RGB gamut can be derived by mixing the primary colors appropriately. Figure 3.3 presents the results of a detailed experimental demonstration of the suggested devices in the form of pixels. A dual characterization is done to ensure the results by measuring the reflectance spectra of the samples with the aid of a home-made customized setup and observing the colors directly under optical microscope

(see Methods, Optical characterization). Figure 3.3(a) shows the experimental and simulated reflectance spectra for highly saturated primary colors. These results show good agreement with each other. Figure 3.3(b) shows the SEM images obtained at different sizes of nanoantennas. Insets are added to the SEM images to show the corresponding colors visible under optical microscope, which are associated with the different sizes of the cross-shaped nanoresonators. Finally, these three primary colors are fabricated in a form of pixel, being the main component of any display device. The size of each square block is 50μm. Details of the used fabrication method are given at the end of the paper. The optical microscope images shown in Fig. 3.3(c) confirm the quality of highly saturated primary colors, which is an important advantage of the suggested all-dielectric metasurface based pixels over the existing plasmonics devices. A CIE 1931 chart is used to represent the simulated and experimental spectra of the primary colors, see Fig. 3(d). One can see a very small shift in color spectrum, which might come from fabrication imperfections. It is noticeable that there is good coincidence between two sets of experimental results.

3.3 Conclusion

Polarization insensitive all-dielectric metasurfaces based on 2D arrays of cross-shaped Si nanoresonators have been proposed to realize color filters with extended gamut for the entire visible spectrum. A numerical investigation has been carried out that demonstrates the principal possibility of obtaining high-purity colors by means of optimization of resonance properties, which can be realized by a relatively simple adjustment of the structural parameters. The role of existence and properties of the dual resonance, which is achieved at a partial overlapping of electric type and magnetic type resonances, and that of suppression of unwanted spectral features in the obtaining of these advancements have been clarified. The utilized resonances can be tuned by changing the length-to-width aspect ratio of individual rectangle-shaped nanoantennas. This concept has been used to design and fabricate the color filters. Our simulation results reasonably agree with the experimental ones. Some differences should be noticed that may be connected with fabrication complexity of the structure. The experimentally demonstrated possibility of obtaining high quality (narrow) resonances, which enable high quality colors, is the most important result of this work. We have demonstrated the wide variety of colors for different periodicity and size of cross-shaped nanoresonators. Additionally, we have demonstrated the primary colors painting in the form of pixels. These colors show high

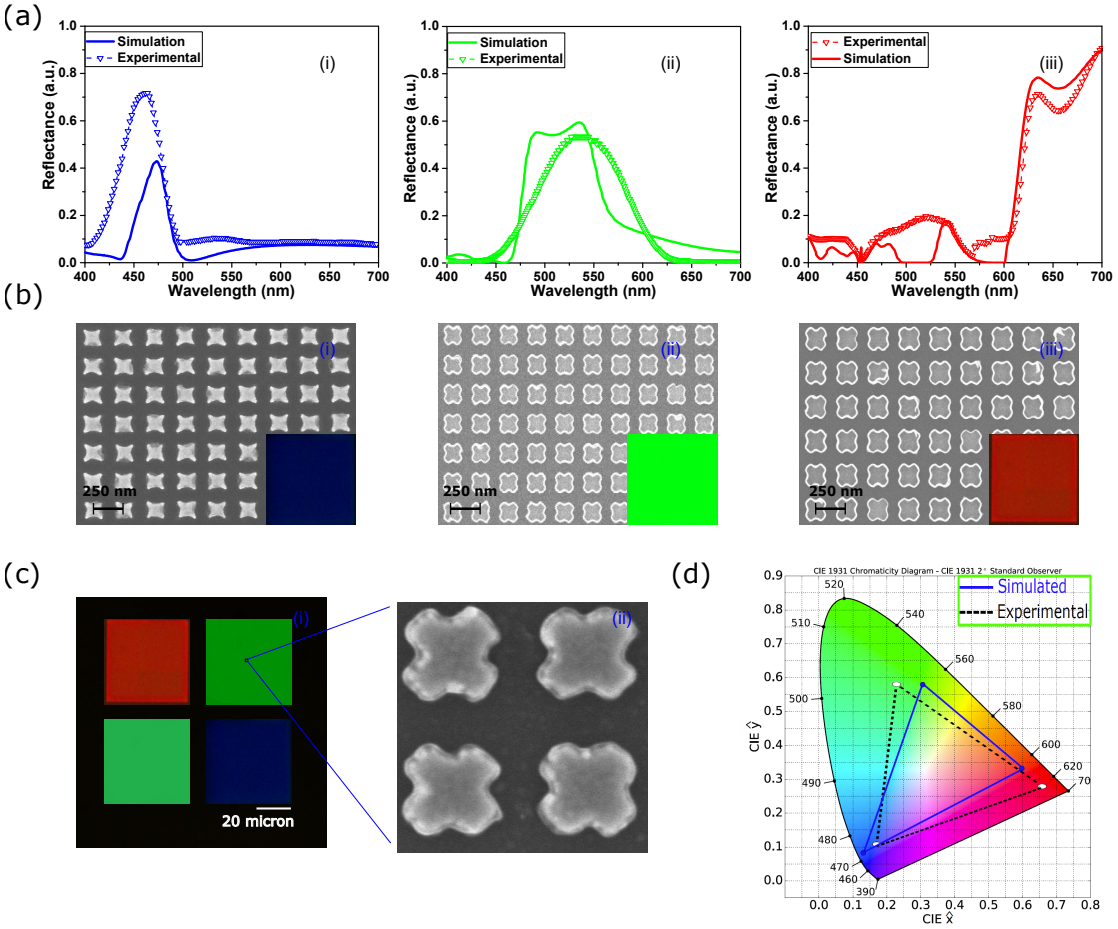

FIGURE 3.3: **Simulation and experimental results for primary colors with SEM images.** (a) Simulated and experimental reflectance spectra. The dimensions of cross-shaped Si nanoresonators (i) $L = 85$nm and $W = 46$nm for blue color. (ii) $L = 114$nm and $W = 62$nm for green color and (iii) $L = 215$nm and $W = 116$nm for red color. The lattice constant is 250nm for all three cases. (b) SEM images of the fabricated structures with the inset view of associated colors. (c) A photograph taken from Nikon camera attached with $50\times$ lens with $NA = 0.65$ and the enlarged SEM image of the nanostructure. (d) A CIE 1931 chromaticity diagram that is used to visualize the simulated and measured colors.

saturation and hue value. In fact, our device is capable to produce a large panel color in the visible regime with strong spectral selectivity, provided that the nanoantenna aspect ratio is properly chosen. By carefully controlling the balance between desired and unwanted Mie resonances, one can further optimize the color filter, especially in dark zone of red color. Since the $a-Si$ (amorphous-Si) is the most suitable material for large-scale fabrication with the existing technology, it can potentially be used for making low-cost, eco-friendly, high quality, long lasting painting possible for mass production in the future.

3.4 Methods

Simulations. We have used Lumerical FDTD solver [44] to study metasurfaces comprising the cross-shaped nanoresonators on a dielectric substrate. The materials used for substrate and cross-shaped nanoresonators are SiO_2 and Si, respectively. The material parameters are taken from default the material library of the used software. A plane wave ranging from 400nm to 700nm is illuminated from the top of the structure. Periodic boundary conditions are used in the unit cell along x and y directions. Perfect matching layer (PML) boundary conditions were used in the z directions to avoid any reflection. The reflectance spectra are simulated by considering a unit cell (one cross-shaped nanoresonator on substrate) with periodic boundary conditions in x and y directions.

Device fabrication. A piranha cleaned quartz sample (275µm thick) is used to fabricate the device. We have deposited a thin layer of 140nm amorphous Si using ICPCVD tool at 300elsius with 150W added microwave power. A single-layer PMMA photoresist is used for patterning cross-shaped nanoresonators by using Raith 150-Two EBL tool. An electronic mask is designed using an open source Python program. The exposed sample is developed using MIBK-IPA (1:3) and an IPA solution for 45s and 15s, respectively. A thin layer of metal (5nm Cr as adhesion layer and 40nm Au) is deposited to transfer the pattern on metal layer for lift-off process using four target evaporators. After lift-off, the sample is etched using plasma asher to get the final pattern. A process flow chart with step by step details is available in supplementary information.

Optical characterization. A dual optical characterization is done to ensure the results. The sample is placed under Olympus optical microscope and illuminated with white light without filter. The colors can be directly seen under optical microscope. The reflectance spectra are measured using a home-made customized setup. A HL 2000 halogen lamp source is coupled with an optical fiber to illuminate the sample in the visible range, *i.e.*, from 400nm to 700nm. A 50× objective lens with $NA = 0.65$ is used to get tight focusing of light on the sample. The reflectance spectra are measured using the same objective lens. All the collected data are normalized with respect to the bare quartz sample. A Nikon camera attached with assembly is used to take the photograph of the illuminated area.

3.5 Supplementary information

3.5.1 Simulations methodology

A commercially available Lumerical FDTD solver is used to simulate the cross shaped nanoresonators (combined noanoantennas). The substrate and cross-shaped nanoantenna materials are SiO_2 and Si that are available from material library of the solver. A total field scattered field (TFSF) source is used to calculate the extinction cross section (ECS) of the single cross shaped dielectric nanoantenna. The used source bandwidth is extended from 400nm to 700nm. Perfectly matched layer (PML) boundary conditions are employed in all directions, i.e., x, y, and z. The calculated ECS spectrum is shown in Fig. 3.4.

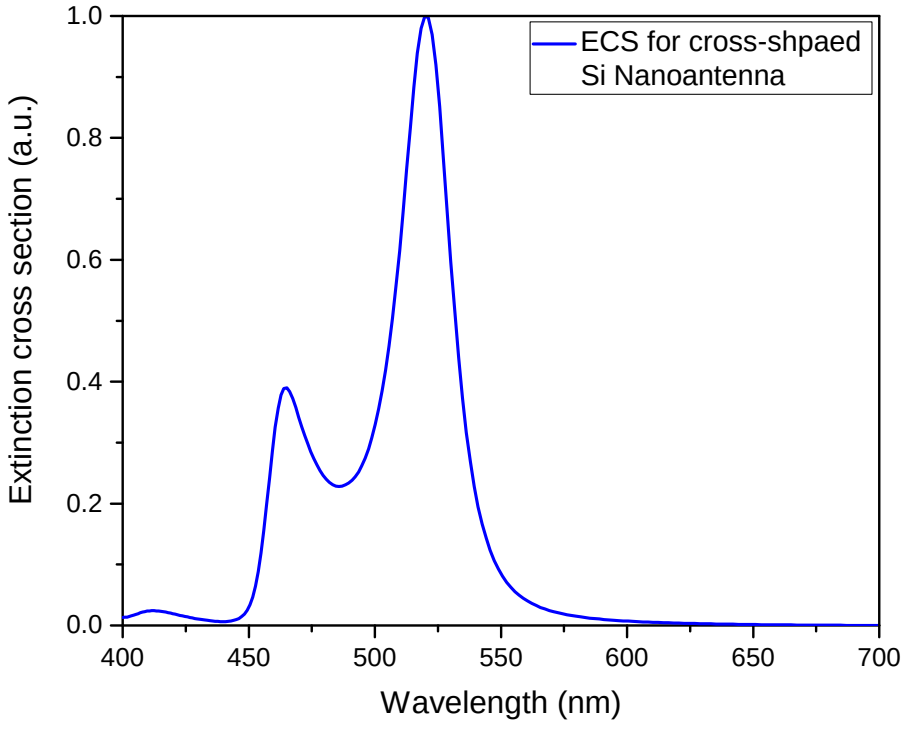

FIGURE 3.4: Extinction cross section (ECS) of single cross shaped Si nanoantenna with length, width and height of 100nm, 50nm, and 140nm, respectively.

In order to get deeper insight, electric and magnetic fields are plotted to clarify the properties of the nanoresonator modes at 465nm and 520nm. The field distributions are shown in Fig. 3.5 (a) and (b). It has to be noticed that at 465nm electric field is predominant in the center region of the cross, whereas magnetic field is predominant

there at 520nm, so we refer to these resonances as electric type and magnetic type resonances, respectively.

The reflectance spectra of 2D arrays of cross shaped Mie resonators are calculated using plane wave excitation, by varying wavelength from 400nm to 700nm. The plane wave is incident from the top of the structure shown in Fig. 3.6. Unit cell simulations are conducted by using periodic boundary conditions in x and y directions and PML boundary conditions in z direction. We have checked the convergence criteria by taking a very fine mesh size, i.e., 2nm in all directions. Figure 3.7 shows the reflectance spectra for numerous scaled structures, while the period is varied from 250nm to 350nm.

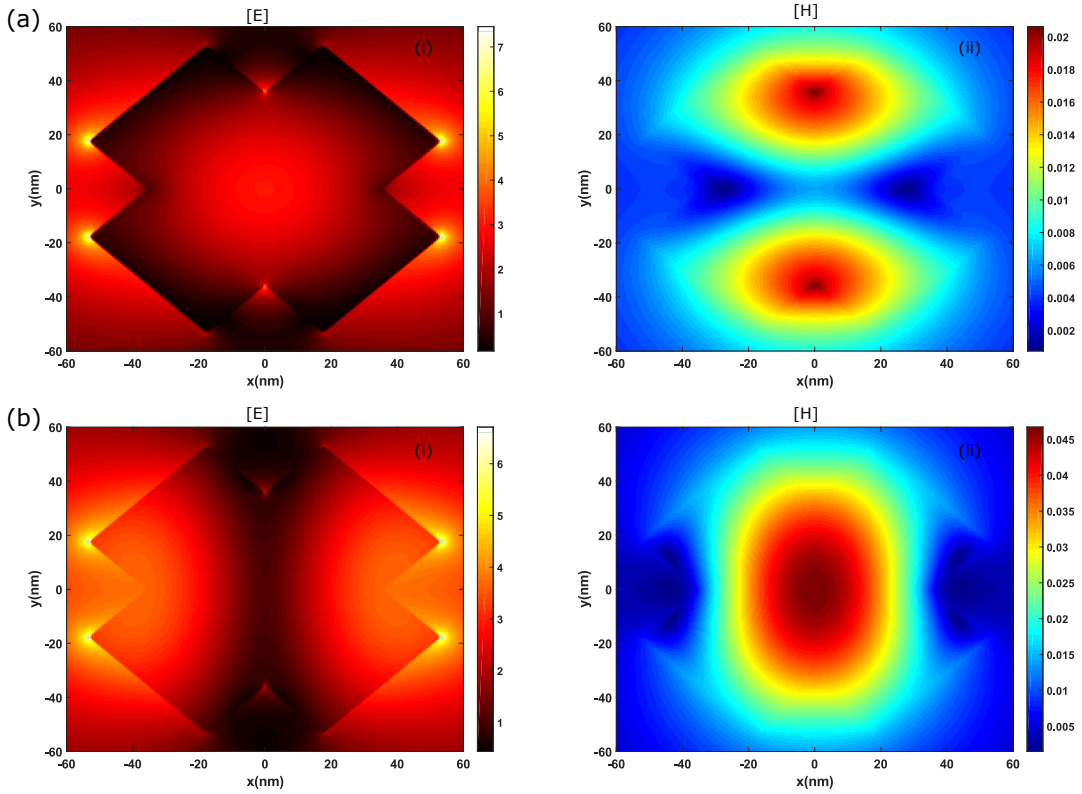

FIGURE 3.5: Electric and magnetic field intensity pattern in the xy plane for $z = 100$nm (a) at $\lambda = 465$nm and (b) at $\lambda = 520$nm.

3.5.2 Color representation from reflectance spectra

There are many methods to classify the different colors in different categories based on their properties. Among them, classification based on primary colors (RGB) is probably the most general one. When a white light is incident on the surface, it can be reflected at certain wavelengths, depending on the surface properties. These reflected wavelengths are perceived by human brain based on human reception system. The response of

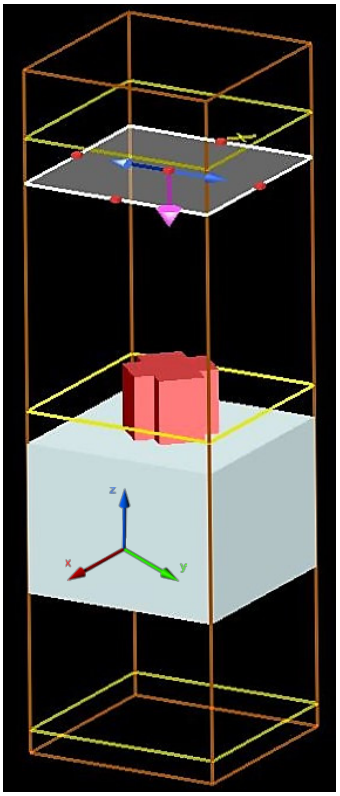

FIGURE 3.6: 3D view of the unit cell of metasurfaces. The structure is illuminated from the the top by a plane wave.

human visualization is not the same for each wavelength. It is defined in terms of standard chromaticity matching functions. These matching functions were defined by Commission Internationale de l'Eclairage (CIE) as followed:

$$X = \int I(\lambda) * CIEX(\lambda) * d(\lambda), \tag{3.1a}$$

$$Y = \int I(\lambda) * CIEY(\lambda) * d(\lambda), \tag{3.1b}$$

$$Z = \int I(\lambda) * CIEZ(\lambda) * d(\lambda), \tag{3.1c}$$

where $I(\lambda)$ is the spectrum of light intensity vs. wavelength, and $CIEX(\lambda)$, $CIEY(\lambda)$, $CIEZ(\lambda)$ are the CIE matching functions. These CIE matching functions are defined over the interval from 360nm to 830nm, and are assumed to be zero for all wavelengths outside this interval. These functions are plotted in Fig. 3.8. All three of them are positive everywhere within the bound, since the intensity of the light can not be negative.

The chromaticity functions X, Y, and Z are normalized to new scale from 0 to 1. The normalized functions are denoted by $\hat{x}$, $\hat{y}$, and $\hat{z}$. The normalization is introduced as

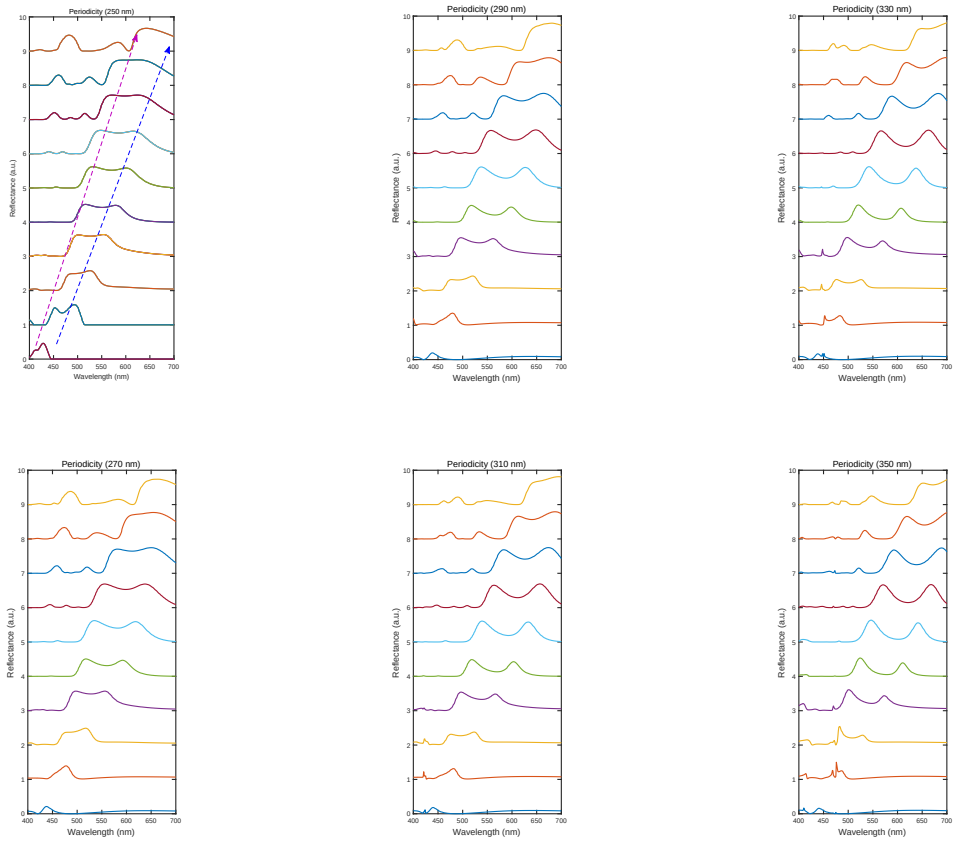

FIGURE 3.7: Reflectance spectra for different values of lattice constant, P, varied from 250nm to 350nm. For each plot, the length and width are scaled from 65nm to 260nm and 35nm to 140nm, respectively.

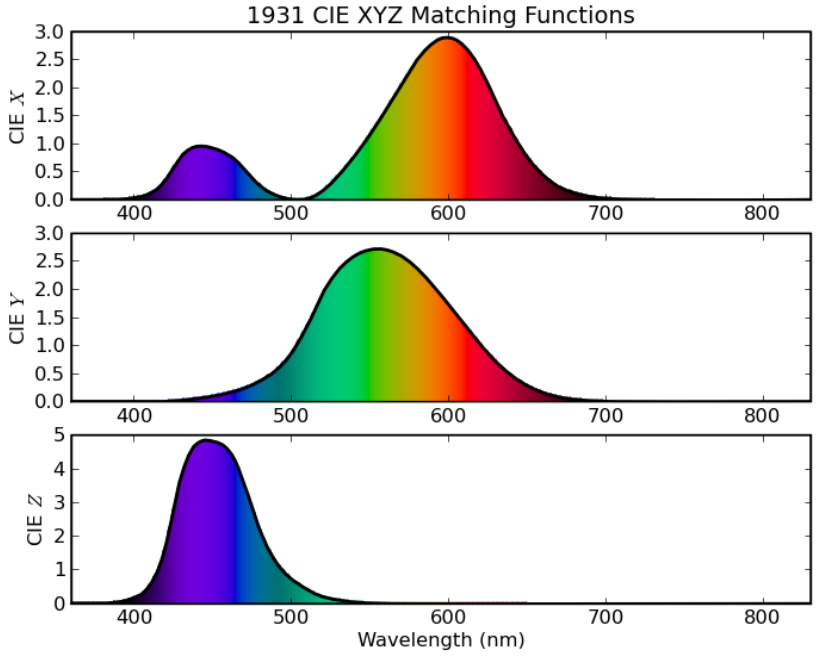

FIGURE 3.8: CIE chromaticity matching functions.

follows:

$$\hat{x} = X/(X+Y+Z), \tag{3.2a}$$

$$\hat{y} = Y/(X+Y+Z), \tag{3.2b}$$

$$\hat{z} = 1 - \hat{x} - \hat{y}. \tag{3.2c}$$

In the general case, the resulting $(\hat{x}, \hat{y})$-plot represents the all possible values of colors on CIE-1931 chromaticity diagram.

3.5.3 Device fabrication

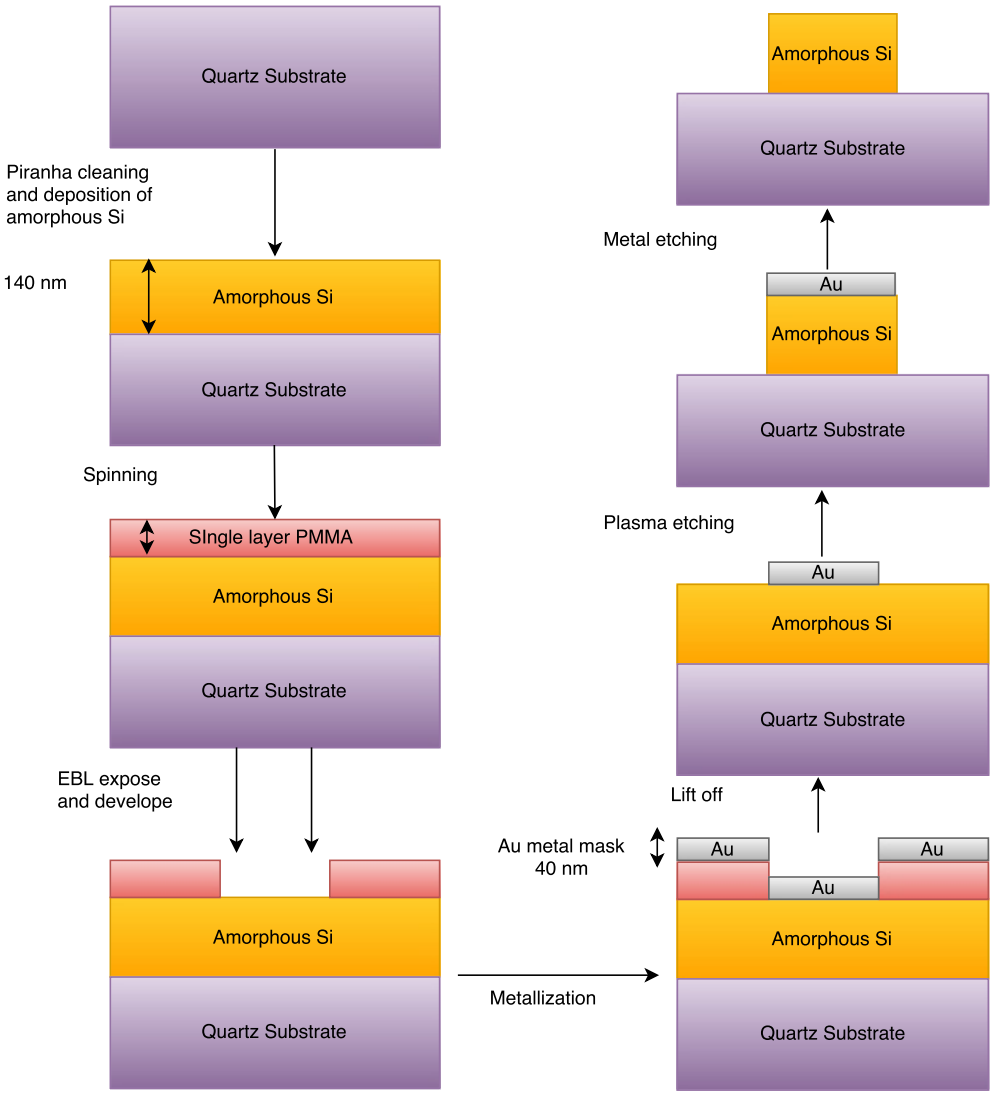

FIGURE 3.9: Process flow chart.

A quartz substrate (275μm thick) is used to fabricate the device. A standard piranha cleaning is done to clean the quartz substrate. We have deposited a thin layer of 140nm amorphous Si using ICPCVD tool at 300°C. We used a 150W microwave power, in addition to inductive coupled power in presence of 10sccm SiH_4, 20sccm H_2 and 20sccm Ar. The process is carried out at very low pressure to get the high quality deposition. A single layer positive photoresist (PMMA 2%) is used for patterning the cross shapes at 4000 RPM for 45s. The pattern is transferred to the PMMA positive photoresist by the Raith 150 electron beam lithography (EBL) tool. This sample is developed using MIBK-IPA (1:3) and IPA solutions for 45s and 15s, respectively. In order to transfer this pattern onto metal, we have deposited 5nm Cr (to increase adhesion) and 40nm Au on top of the patterned sample. These depositions are carried out with the aid of a thermal evaporator. After depositing the metal, we have kept the sample in acetone for 15h to lift-off the metal from the unwanted area. Finally, we have checked the pattern under optical microscope to confirm the result of liftoff process. This sample is etched using a plasma etcher, where the metal layer behaves like a hard mask to protect the patterned area. We used 30sccm ChF_3 and 10sccm O_2 to etch the amorphous Si anisotropically. The process is carried out for 4min. Finally, a Au etchant and a Cr etchant are used to remove the metal mask layer, which results in the appearance of cross shaped Si nanoresonators on top of the quartz substrate. A complete process flow is schematically shown in Fig. 3.9.

3.5.4 Optical characterization

A dual optical characterization is done to ensure the correctness of the results. The sample is placed under an Olympus optical microscope, which is illuminated with white light without filter. The colors that can be directly seen under microscope are shown in Fig. 3.10.

The reflectance spectrum is measured using a homemade customized setup. A HL 2000 halogen lamp source is coupled with an optical fiber to illuminate the sample in visible range (400nm to 700nm). A 50× objective lens with $NA = 0.65$ is used to tight focus on the sample. The reflectance is measured by using the same objective lens. The data are normalized with respect to the bare quartz sample. The simulated and experimental reflectance spectra are shown in Fig. 3.11.

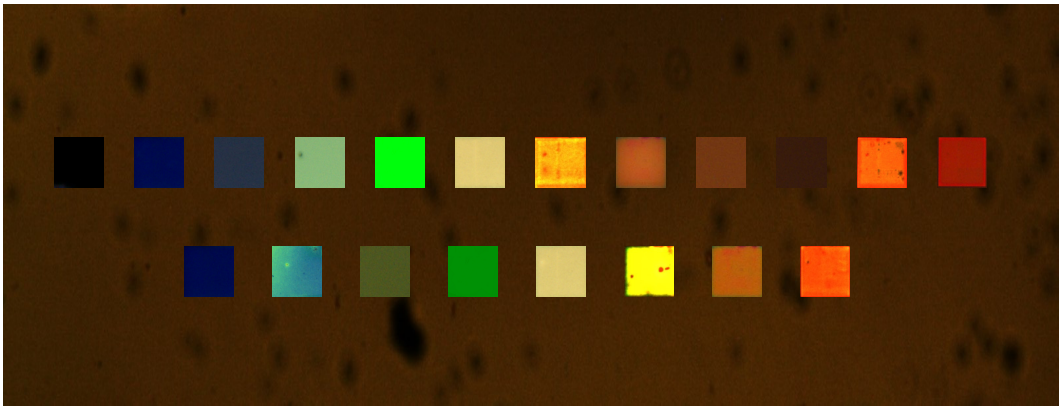

FIGURE 3.10: Colors visible under optical microscope.

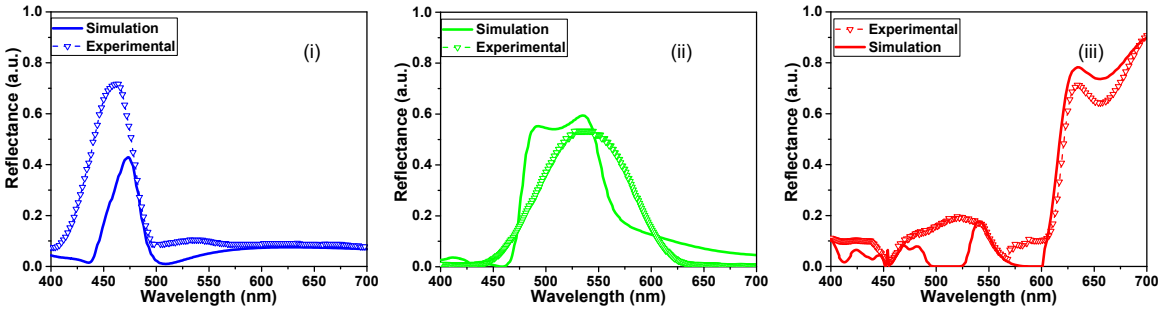

FIGURE 3.11: Simulated and experimental reflectance spectra for RGB colors.

Chapter 4

Polarization tunable all-dielectric color filters*

Polarization sensitive and insensitive color filters have important applications in the area of nano-spectroscopy and ccd imaging applications. Metallic nanostructures provide an efficient way to design and engineer ultrathin color filters. These nanostructures have capability to split the white light into fundamental colors and enable color filters with ultrahigh resolution but their efficiency can be restricted due to high losses in metals especially at the visible wavelengths. In this work, we demonstrate all-dielectric color filters based on Si nanoantennas, which are sensitive to incident-wave polarization and, thus, tunable with the aid of polarization angle variation. Two different information can be encoded in two different polarization states in one nanostructure. The nanoantenna based pixels are highly efficient and can provide high quality of colors, in particular, due to low losses in Si at optical frequencies. We experimentally demonstrate that a variety of colors can be achieved by changing the physical size of the nonsymmetric cross-shaped nanoantennas. The proposed devices allow to cover an extended gamut of colors on CIE-1931 chromaticity diagram due to the existence of high-quality resonances in Si nanoantennas. Significant tunability of the suggested color filters can be achieved with the aid of polarization angle change in both transmission and reflection mode. Additional tunability can be obtained by switching between transmission and reflection modes.

*This chapter is published in Scientific Reports [51]

4.1 Introduction

The light-matter interaction depends on size and shape of the object. Generally, operation of a plasmonic color filter is based on separation of the white light components with the aid of the engineered plasmon resonance. The resonance characteristics can be statically tuned by altering the physical size of the nanostructure and its composition, which in turn determine wavelengths, at which light is predominantly scattered, absorbed, or transmitted [107]. But what is most interesting and important for practical applications is that these specific wavelengths also depend on the angle of incidence and polarization of incident light. These dependencies can be efficiently utilized in design of dynamically tunable color filters that do not need external bias. Several polarization sensitive color filters have earlier been reported, which operate either in transmission mode [82, 84, 103, 108–110] or reflection mode [79, 111–113]. Most of the known performances are realized using plasmonic (metal) nanostructures. Earlier, the choice for realization of these nanostructures was gold and silver. However, gold is costly for large scale fabrication. It also suffers of interband transitions in the visible frequency range, while silver faces the problem of aging, since it is highly reactive with native oxides [89]. Aluminum might be a good choice because of high stability and low cost [83, 114, 115]. Unfortunately, Al is even more lossy due to interband transition in visible range. Ultimately, plasmonic color filters have high losses at the visible wavelength regime. Most of them operate in transmission mode. Few of them operate in the dual mode that involves reflection and transmission modes [116, 117]. Recently, the investigations have been conducted with the aim to design and fabricate all-dielectric based color filters [47, 80, 104] and hybrid ones which combine metallic and dielectric components [103]. Another methodology is based on the use of complementary design methods with the hope of high-quality saturated colors [118], which can cover a wide gamut on CIE-1931 chromaticity diagram. However, operation of the filters suggested to the time is polarization insensitive.

In this work, we demonstrate all-dielectric, polarization sensitive color filters, which are composed of nonsymmetric Si nanoantennas, unlike the earlier reported ones that use metal based plasmonics nanoantennas [82, 84, 103, 108]. It is demonstrated that the proposed color filters are strongly sensitive to the incident-wave polarization due to nonsymmetric cross shape of the used nanoantennas and, thus, they can be tuned by changing polarization. The nanoantennas show low losses at the visible spectrum and high confinement of light. We experimentally demonstrate that our color filters can

operate in transmission and reflection modes, and can be tuned by changing the incident-wave polarization in each of these modes. The low losses of Si nanoantennas result in high quality of colors in both modes. The designed nanoantennas are nonsymmetric and cross-shaped so two information can be encoded in one physical structure, and then decoded by using two incident waves with orthogonal polarization states. In contrast with the recently reported color filters, the proposed color filter combine advantages of all-dielectric design and related wide gamut of highly saturated colors with advantages of sensitivity to polarization and dual mode operation.

4.2 Results

Operation Principles. First, let us consider an array of rectangular Si nanoantennas. It is excited by x-polarized plane wave in the visible range. The nanoantennas are shown to be scalable by means of the length variation. Width, length, and height have initially been chosen as 40nm, 60nm, and 200nm, respectively, and then length varied from 60nm to 200nm. The simulated results for transmittance spectrum are presented in Fig. 4.1 (a). A dip in transmission spectrum for certain wavelength corresponds to certain color selectivity [82]. Thus, in order to obtain different colors for different nanoantenna lengths, it is necessary to have a transmission dip at the visible spectrum, and it must be shifted from lower visible spectrum to upper visible spectrum to achieve any arbitrary color.

As expected, the transmission dip occurs and is shifted towards larger wavelengths, while the nanoantenna length is increased. The extinction cross section of the corresponding single nanoantenna is also shifted towards larger wavelengths (see more details in supplementary information, Figure S1). In Fig. 4.1 (b), the obtained transmittance spectrum is converted into colors presented with the aid of CIE-1931 chromaticity diagram. One can see that different colors can be possible by partial scaling of nanoantennas that is achievable by varying the lengths of rectangular nanoantennas. From the presented simulation results, it follows that an arbitrary color can be achieved by properly selecting the length. Using these results, we have selected two rectangular nanoantennas and combined them to form a nonsymmetric cross. Freedom in choice of the length ratio of the longer (horizontal) to the shorter (vertical) segment allows us to obtain significant difference in resonance frequency for these segments and make the resulting structure sensitive to polarization of the incident wave. Thus, operation of the cross-shaped nanoantennas

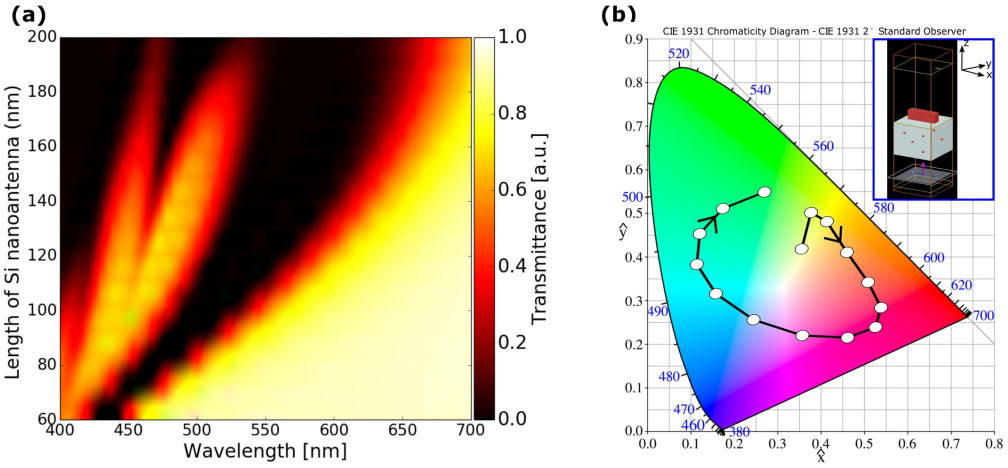

FIGURE 4.1: (a) Transmittance of Si rectangular nanoantennas on quartz substrate, when nanoantenna length is gradually varied from 60nm to 200nm. (b) Representation of transmittance spectra on CIE-1931 chromaticity diagram; blue numbers indicate wavelengths in nm for the ideal colors. Black line with circles indicates color changes when nanoantenna length is varied from 60nm (first circle) to 200nm (last circle); arrow shows direction in which length is increased. Inset shows unit cell of the simulated array of rectangular shaped Si nanoantennas with periodic boundary conditions; unit cell boundaries coincide with equicoordinate surfaces of Cartesian coordinate system.

and metasurface on their basis depends on polarization state. The general geometry of the designed metasurface is shown in Fig. 4.2. The lengths of the horizontal (L_h) and vertical (L_v) segments of each nonsymmetric nanoantenna are 150nm and 90nm, respectively, while the width ($W = W_h = W_v$) and height (h) are 40nm and 200nm for the both segments. The nanoantennas form square lattice with the lattice constant of 250nm. The Si nanoantennas are placed on top of the quartz substrate, whose thickness is $t = 275 \pm 5\mu$m, see Fig. 4.2(a). A schematic illustrating the structure excitation by using the x-polarized ($\Phi = 0°$) and the y-polarized ($\Phi = 90°$) normally incident waves (Φ denotes the polarization angle in the (x, y)-plane) is shown in Fig. 4.2(a), inset. Figure 4.2(b) presents the SEM image of the fabricated structure. The schematic of the device operating in transmission and reflection mode is presented in Fig. 4.2(c).

Response at each of two orthogonal polarizations is mainly determined by the length of either the horizontal or the vertical segment. For an arbitrary polarized, normally incident wave, the combined response, i.e., total transmission due to both polarization components, is given by the following equation:

$$T(\Phi, \lambda) = T_v(\lambda) \sin^2 \Phi + T_h(\lambda) \cos^2 \Phi, \tag{4.1}$$

where Φ is polarization angle and λ is free-space wavelength. $T_v(\lambda)$ and $T_h(\lambda)$ mean transmittance for y-polarized and x-polarized light, respectively.

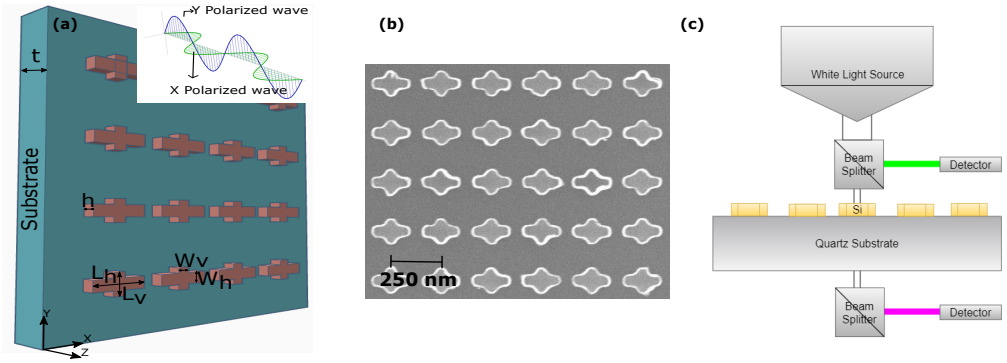

FIGURE 4.2: (a) Metasurface composed of nonsymmetric Si nanoantennas placed on top of quartz substrate; inset schematically shows wave propagation in case of x-polarized ($\Phi = 0°$) and y-polarized ($\Phi = 90°$) normally incident wave. (b) Top view of SEM image of fabricated device. (c) A schematic representation of the color filter operating in transmission and reflection modes.

In order to illustrate sensitivity of the combined response of the device to variations of polarization, we performed simulations by changing Φ from 0° to 90° with the step of 10°. The results are presented in Fig. 4.3. One can see that strong redistribution of the incident-wave energy between the transmitted and reflected waves takes place in the whole wavelength range considered (see supplementary information, Fig. S2 to S5). Moreover, there is strong sensitivity to the polarization state. For instance, the lowest Mie resonance is expected to appear for the horizontal antenna segment near 570nm, where the transmission dip appears for one of two orthogonal polarizations, $\Phi = 0°$, and then gradually disappears while increasing Φ. In turn, the transmission dip for the second orthogonal polarization, $\Phi = 90°$, which should be connected with the lowest Mie resonance of the vertical segment, appears near 480nm. The obtained results indicate that different colors can be obtained at different polarization states for a fixed set of geometrical parameters. As the length of the nanoantenna is increased, a higher Mie resonance appears for the horizontal segments, which leads to the additional dip of transmittance at 420nm when $\Phi = 0°$. More details regarding the effect of variation of Φ are given in supplementary information in Fig. S2 to S5. Two cases in Fig. 4.3 are interesting from the physics point of view, in which dependence on Φ tends to disappear. However, they are out of interest for the studied tunability mechanism which needs, in the contrast, strong sensitivity to variations in Φ.

To further clarify the operation principles of individual nanoantenna as a nanopixel, we have drawn the field distributions for the cross-shaped nanostructure for two orthogonal states of polarization of the incoming wave. Each nanoantenna segment, i.e., vertical and horizontal one, responds individually when electric vector of incident wave align with the geometry. In Fig. 4.4, electric and magnetic fields are plotted for $\Phi = 0°$

and 90°. When the electric field vector of the incoming wave is align with horizontal or vertical nanoantenna segment, the corresponding segment behaves like an individual pixel, whose response can be tuned by varying the length. Thus, when $\Phi = 90°$, only the vertical nanoantenna segment responds, that justifies the resonance observed in Fig. 4.3 near 480nm. For $\Phi = 0°$, horizontal segment nanoantenna is in excitation mode, and this results in resonance observed in Fig. 4.3 near 570nm. The magnetic field is confined around the center of the cross in both cases, so strong difference in electric field distribution is the origin of polarization sensitivity.

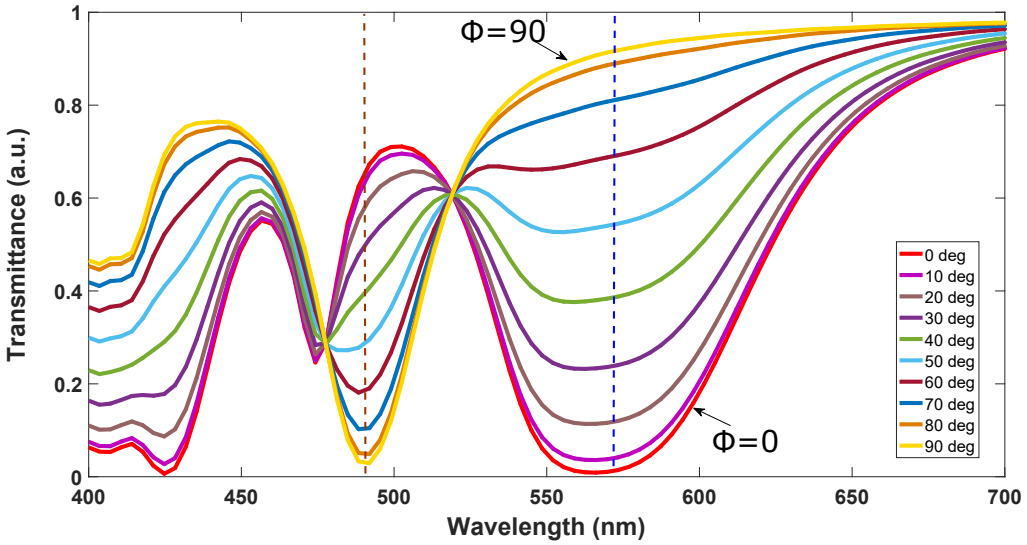

FIGURE 4.3: Shift in transmittance spectra when polarization angle of incoming wave, Φ, is changed from 0° to 90°. Dashed lines indicate two resonance cases with strong transmission contrast between two orthogonal polarization states ($\Phi = 0°$ and $\Phi = 90°$).

Experimental Validation Since white light contains all colors, its each spectral component is associated with a certain color in transmission and reflection modes. We have selected and considered in detail two nanoantenna design cases with two different dimension sets which are given in Table 4.1. These sets are chosen so that we could demonstrate the primary colors, i.e., RGB or CMY. Indeed, we observed different colors for different states of polarization of the incoming wave. In particular, RGB and CMY colors are obtained in reflection and transmission mode, respectively.

TABLE 4.1: **Dimensions of the studied nanoantennas in nm.**

	L_v	L_h	W_v	W_h	h
Case 1	90	160	40	40	200
Case 2	110	190	40	40	200

.

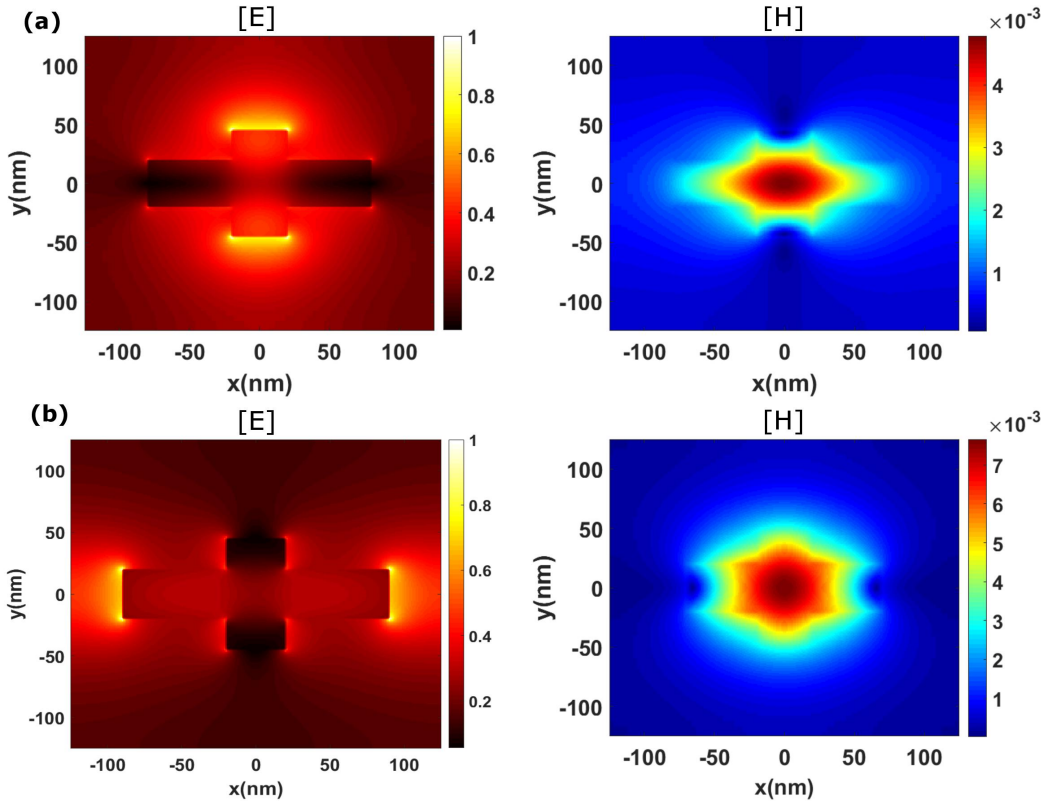

FIGURE 4.4: Electric and magnetic field distribution in (x, y)-plane, at the mid-height of nanoantenna ($z = h/2$): (a) $\lambda = 480$nm, y-polarized incident wave and (b) $\lambda = 570$nm, x-polarized incident wave.

Figure 4.5 presents the experimental colors observed under the optical microscope in transmission mode, when Φ is gradually varied from 0° to 90°. For $\Phi = 0°$, color response corresponds to the excitation of horizontal (oriented along the x-axis) nanoantenna segments, whereas $\Phi = 90°$ corresponds to the excitation of vertical (oriented along the y-axis) nanoantenna segments. For given sizes, a variety of colors, each of which corresponds to a certain value of Φ, is obtained, so tunability can be realized by means of variations in Φ. The intermediate response between $\Phi = 0°$ to 90° can be understood from the above presented discussion for equation 4.1. The achievable set of colors is determined by the ratio of the lengths of the vertical and horizontal segments. Whilst location of the transmittance dip is a function of nanoantenna length, it can be shifted within a larger part of the visible spectrum by scaling nanoantennas. The effect of geometrical parameters of nanoantennas is illustrated by the comparison of Case 1 and Case 2 in Fig. 4.5. By properly adjusting the lengths of two segments of each cross-shaped Si nanoantenna, any two arbitrary colors can be formed using only $\Phi = 0°$ and $\Phi = 90°$ cases.

A specific portion of the incident white light is reflected from the metasurface, while another part is transmitted through the array on quartz substrate, as schematically

shown in Fig. 4.2(c). The dielectric nanoantennas have very low losses that enables creation of various high-quality colors in both transmission and reflection mode. When the same devices operate in reflection mode, we obtain different colors for different states of polarization of the incoming wave. Figure 4.6 presents the experimental colors seen under the optical microscope in reflection mode when Φ is varied from 0° to 90°. As expected, the obtained set of colors is different than for transmission-mode operation. Again, the set of colors that are tunable by varying Φ depends on values of L_v and L_h, so the difference in colors achievable in Case 1 and Case 2 is significant. Moreover, since different color sets are obtained in transmission and reflection modes, additional degree of freedom in tunability can be added by switching between these two modes.

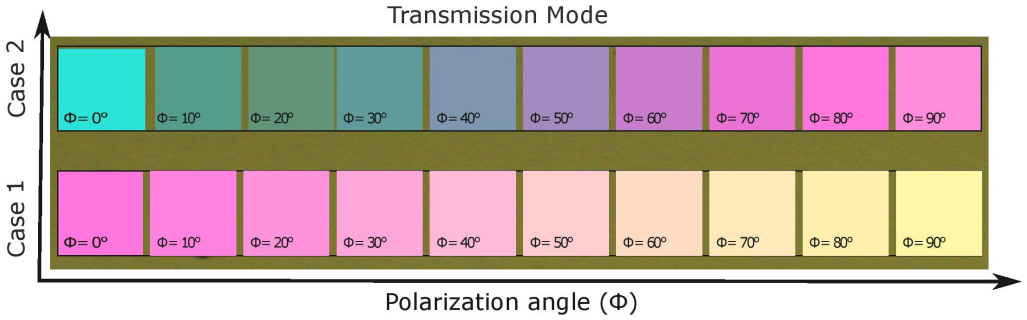

FIGURE 4.5: Colors visible under optical microscope in transmission mode when Φ is gradually varied from 0° to 90°. Dimensions of nanoantennas are given in Table 4.1.

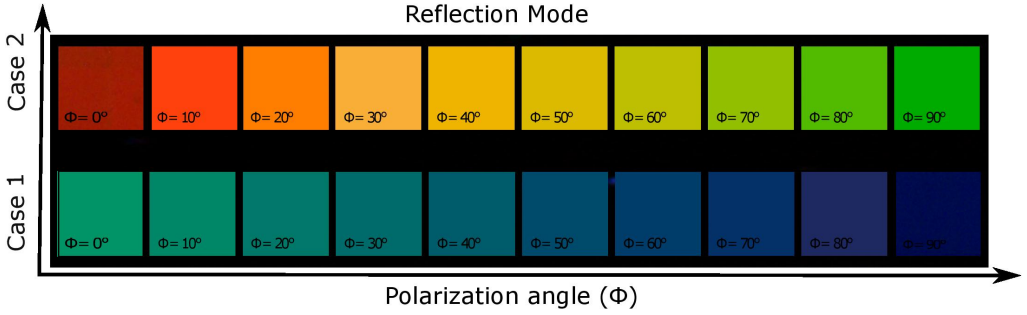

FIGURE 4.6: Colors visible under optical microscope in reflection mode when Φ is gradually varied from 0° to 90°. Dimensions of nanoantennas are given in Table 4.1.

A dual characterization is carried out to justify the above discussed results. We have used a home-made customized setup for this purpose. The details of the optical characterization are available in supplementary information. The experimental transmittance and reflectance spectra are converted into the colors by using standard chromaticity matching functions [119], see supplementary information. For the Case 1 and Case 2, the gradual color changes are observed when polarization angle is gradually varied from 0° to 90°. In Fig. 4.7, the experimental and simulated results are plotted on the standard CIE 1931 chromaticity diagram, in order to visualize the achievable color tunability. Generally, these results are in good coincidence. Some discrepancy appears due

to imperfections in fabrication and limitations of measurement accuracy. In particular, its possible reasons can be connected with that it can be difficult to fabricate a nanostructure with a high-aspect ratio. For Case 1 in transmission mode, it is expected from the simulation results that the changes in color should occur from magenta to yellow zone, when polarization of incident light is changed from 0° to 90°, and so happens in the experimental results with acceptable deviation. For Case 1 in reflection mode, color changes are predicted from green to blue zone, based on the simulation results, and so happens in the experimental results, also with acceptable deviation. A similar level of results coincidence has been found for Case 2, in both reflection and transmission modes. Hence, there is a good agreement between the simulation and experimental results, as far as the latter are still in the predicted zone of the colors.

Further study of the effect of geometrical parameters of the cross-shaped nanoantennas and their optimization can be promising for obtaining alternative tunability scenarios and possible extension of the tuning range.

4.3 Discussion

In summary, we have studied all-dielectric metasurfaces based on nonsymmetric cross-shaped Si nanoantennas, which are designed to operate as color filters in transmission and reflection modes. The proposed designs of low-loss all-dielectric filters enable high quality of colors for the both modes. The resonance location responsible for color selectivity can be varied in a desired way by properly adjusting sizes of individual nanoantennas. The nonsymmetric cross shape of nanoantennas makes them strongly sensitive to the polarization state of incident wave. Hence, efficient tuning of colors can be achieved in one structure just by changing polarization angle, as expected. The range of achievable colors depends on sizes of rectangular segments creating a cross. Tuning based on polarization change can be efficiently used in both transmission and reflection modes. In turn, switching between transmission and reflection modes gives more freedom for tuning. The proposed devices allow covering a wide gamut of colors on CIE-1931 chromaticity diagram. In particular, RGB or CMY colors are obtained in reflection and transmission mode, respectively. There is good coincidence between simulation and experimental results. Results of higher accuracy could be obtained by improvement of

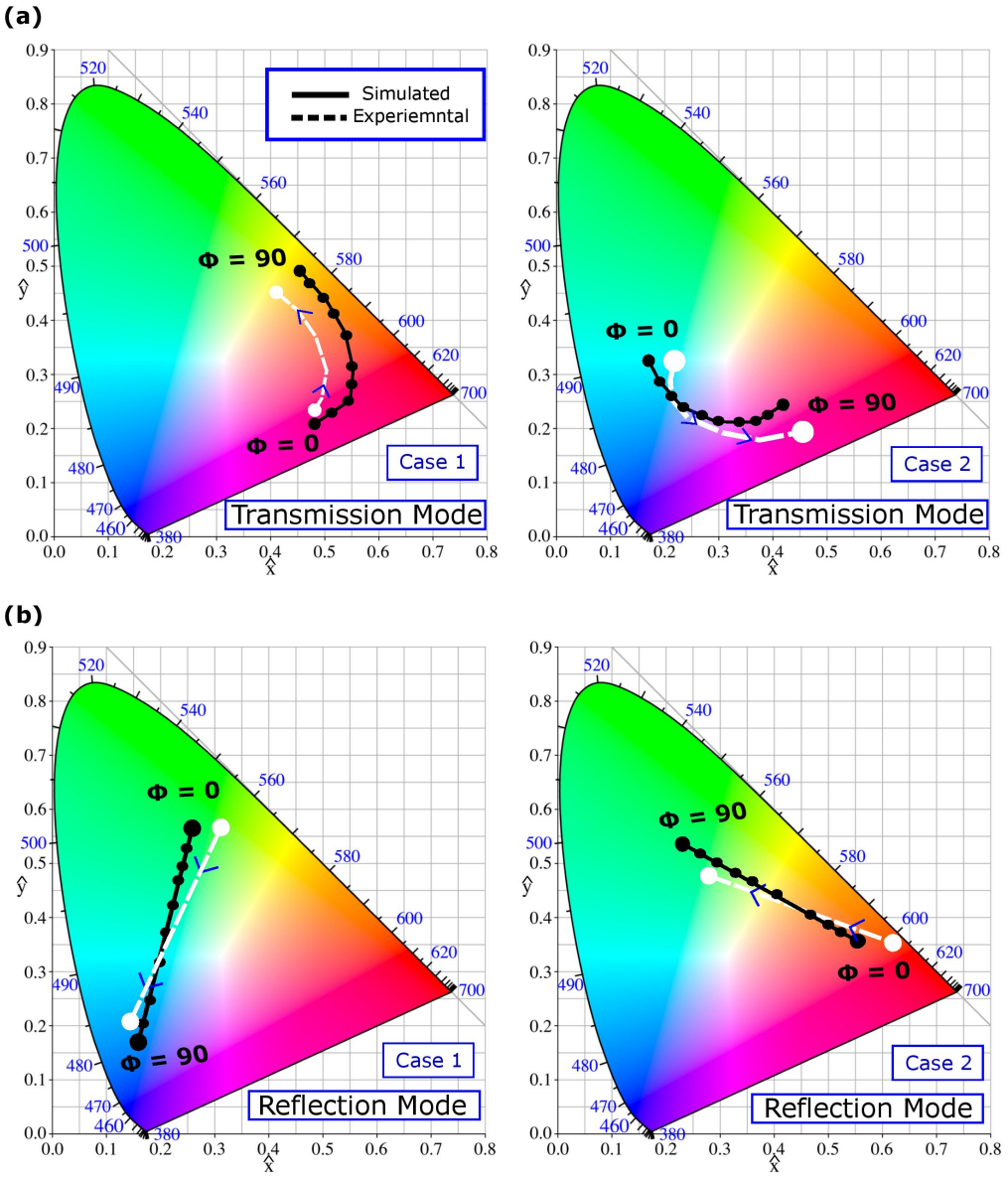

FIGURE 4.7: Polarization related changes in color: (a) for transmission mode, from magenta to yellow in Case 1 and from cyan to magenta in Case 2. (b) For reflection mode, from green to blue in Case 1 and from red to green in Case 2. Polarization angle of incident white light (Φ) is switched for experimental results from 0° to 90°; simulation results for polarization states, which correspond to Φ varied from 0° to 90° with the step $\Delta\Phi = 10°$, are shown for comparison. Blue numbers indicate wavelengths in nm for the ideal colors.

fabrication quality and measurement setup. The suggested devices have potential applications in the area of secured optical tag, nano spectroscopy, fluorescence microscopy and CCD imaging.

4.4 Methods

Simulations. We have used Lumerical FDTD [44] solver to study transmission and reflection for the metasurfaces comprising cross-shaped nanoantennas on quartz substrate. The materials used for substrate and cross-shaped nano antenna are SiO_2 and Si, respectively. The material parameters are taken from the default material library of the used software. A plane wave ranging the wavelength from 400nm to 700nm is incident from the top of the structure. The reflectance and transmittance spectra are simulated by considering a unit cell (single cross shaped nanoantenna on substrate) with periodic boundary conditions in x and y directions. Perfect matching layer (PML) boundary conditions were used in z direction to avoid reflections.

Device fabrication. A piranha cleaned quartz sample (275µm thick) is used to fabricate the device. We have deposited a thin layer of 200nm amorphous Si using ICPCVD tool at 300elsius with 150W added microwave power. A single-layer PMMA photoresist is used for patterning cross-shaped nanoresonators by using Raith 150-Two EBL tool. An electronic mask is designed using an open source Python program. The exposed sample is developed using MIBK-IPA (1:3) and an IPA solution for 45s and 15s, respectively. A thin layer of metal (5nm Cr as adhesion layer and 40nm Au) is deposited to transfer the pattern on metal layer for lift-off process using four target evaporators. After lift-off, the sample is etched using plasma asher to get the final pattern. A process flow chart with step by step details is available in supplementary information.

Optical characterization. A dual optical characterization is done to ensure the results. The sample is placed under Olympus optical microscope and illuminated with white light without filter. The colors can be directly seen under optical microscope in reflection and transmission mode by changing the polarization of the incident light. The reflectance and transmission spectra are measured using a home-made customized setup. A HL 2000 halogen lamp source is coupled with optical fiber to illuminate the sample with the light in visible range (wavelength of 400nm to 700nm). A polarizer is added in the path of the optical fiber to control the polarization. A 50× objective lens is used to tight focus the light on the sample. The spectra are measured by using the same objective lens. The data are normalized with respect to bare quartz sample. A Nikon camera attached with the assembly is used to take the photograph of illuminated area.

4.5 Supplementary information

4.5.1 Simulations methodology

A commercially available Lumerical FDTD solver is used to simulate a single rectangular nanoantenna and nanoantenna arrays. Si and SiO_2 are used as materials for nanoantennas and substrate, respectively. Their parameters are taken from the material library of the used software. First, the extinction cross section (ECS) of a single rectangular dielectric nanoantenna has been calculated by using a total-field scattered-field (TFSF) source with the bandwidth adjusted to visible wavelength which extends from 400nm to 700nm. The perfectly matched layer (PML) boundary conditions are employed in all three orthogonal directions, i.e., x, y, and z. Fig. 4.8 shows the ECS of the nanoantenna, when length of the rectangular nanoantenna is changed from 60nm to 200nm.

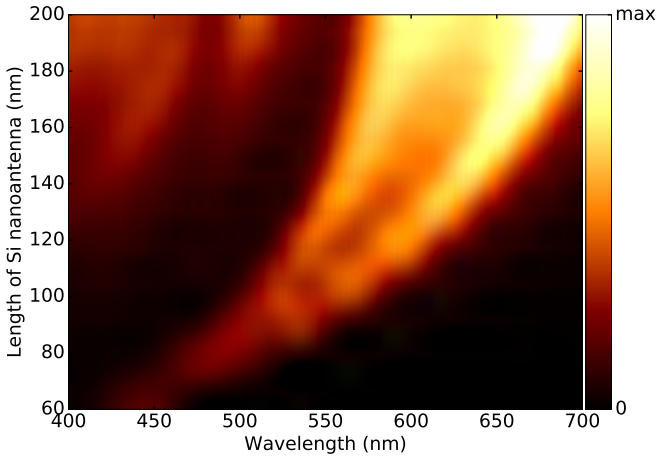

FIGURE 4.8: Extinction cross section (ECS) of single rectangular Si nanoantenna with width and height of 40nm and 200nm, respectively; its length is gradually increased from 60nm to 200nm. Two resonance peaks are associated with electric type and magnetic type resonances.

At smaller length values, the scattering peak is shifted from lower to higher visible spectrum. When the length is increased, the peak is split into two peaks. The larger the length, the stronger the peaks are shifted towards larger wavelengths. These two peaks can be associated with electric and magnetic resonances, which are known for dielectric nanoparticles. Some additional modes may also appear when the length of Si nanoantennas increases. However, the main contribution to scattering is provided by one or two modes, which manifest themselves in the shift of the ECS maxima from left to right, while the length of the Si nanoantennas is increased.

In order to get the reflectance and transmittance spectra for the array of cross-shaped nanoantennas, we have illuminated the metesurfaces with plane waves having different polarization states. We have used periodic boundary conditions in x and y directions and PML boundary conditions in z direction. In Figure 4.9, the color map of transmittance spectra is presented in wavelength - polarization angle (Φ) plane. Figure 4.10 illustrates the shift of the transmittance minima when Φ is switched from 0° to 90°. Figures 4.11 and 4.12 present reflectance in the same manner and in the same ranges of parameter variations as Figs. 4.9 and 4.10.

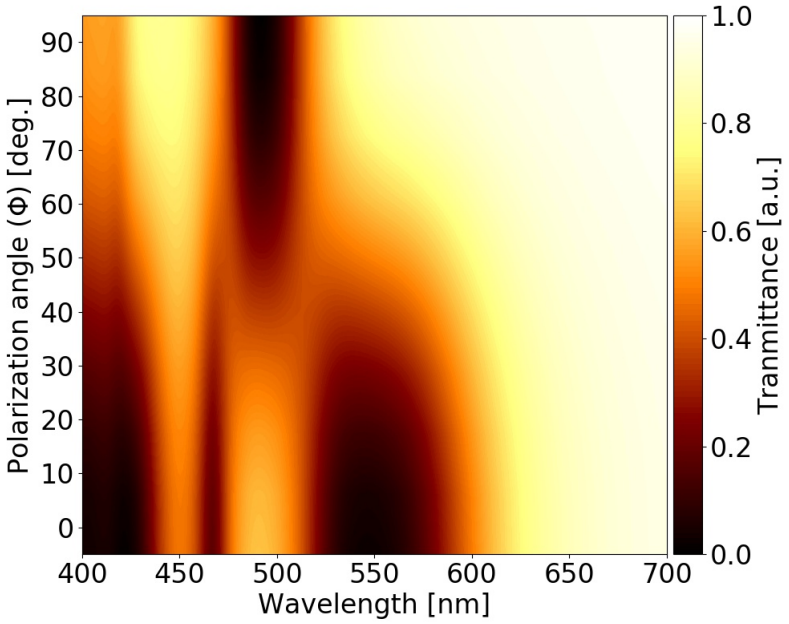

FIGURE 4.9: Color map of transmittance for arbitrary polarization state of incident wave in the visible region.

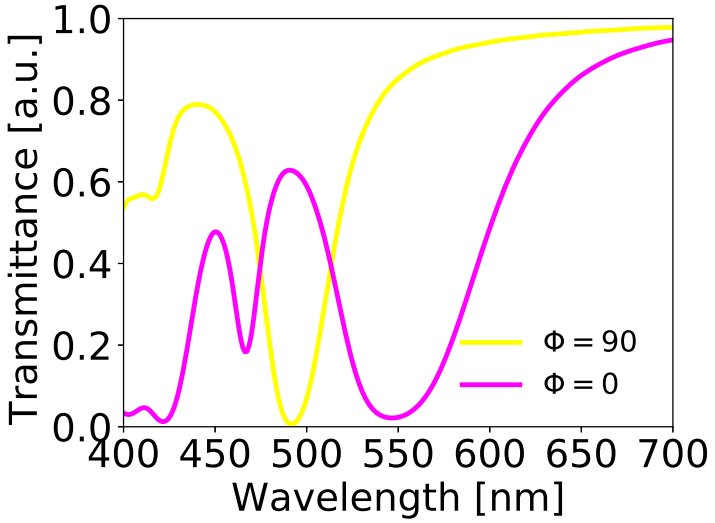

FIGURE 4.10: Transmittance at $\Phi = 0°$ and $\Phi = 90°$. Shift of the dip is clearly seen.

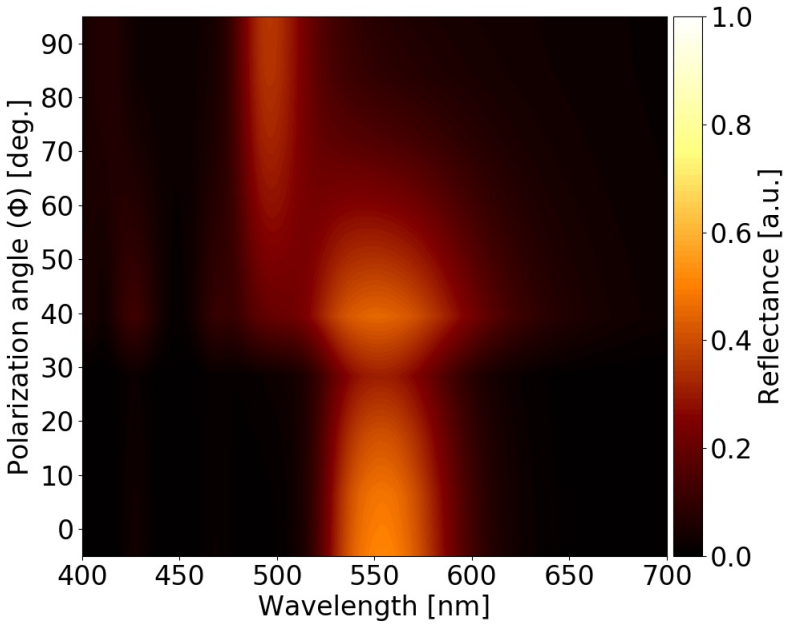

FIGURE 4.11: Color map of reflectance for arbitrary polarization state of incident wave, in the whole visible region.

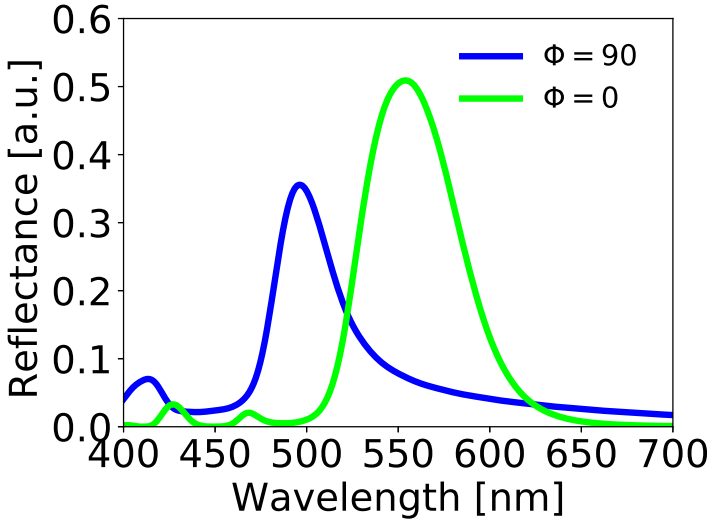

FIGURE 4.12: Reflectance at $\Phi = 0°$ and $\Phi = 90°$. Shift of the maximum is clearly seen.

4.5.2 Color representation on CIE-1931 Chart

This section has already been discussion in chapter 3 under supplementary information section.

4.5.3 Device fabrication

This section has already been discussion in chapter 3 under supplementary information section.

4.5.4 Optical characterization

A dual optical characterization is done to ensure the correctness of the results. The sample is first placed under Olympus optical microscope illuminated with a white light without filter. The colors can be directly seen under optical microscope in reflection and transmission modes at various polarization angles. Then, reflectance and transmittance spectra are measured using a home-made customized setup. A HL 2000 halogen lamp source is coupled with optical fiber to illuminate the sample in the visible range, i.e., from 400nm to 700nm). A polarizer is added in the path of the optical fibre to control the polarization. A 50× objective lens is used to focus the light on the sample. The reflectance and transmittance spectra are measured by using the same objective lens. The data are normalized with respect to the bare quartz sample. A Nikon camera attached with the assembly is used to take the photograph of the illuminated area.

Chapter 5

Liquid-crystal tunable color filters*

Designing color pixels using plasmonic nanostructures and metasurfaces has become a luring area of research in recent years. Here, we experimentally demonstrated the voltage tunability of a dynamic plasmonic color filter by using an aluminum grating integrated with the nematic liquid crystal (LC). Along with a typical substrate coated with rubbed polyimide film, the aluminum grating itself serves as a molecular alignment layer to form a twisted LC cell. This hybrid structure allows electrically controlled transmission color by applying the voltage. A significant spectral tunability of such a device has been demonstrated by applying the small voltage from 0 to 4 V_rms.

5.1 Introduction

Color filtering is a key function in many optical and optoelectronics applications such as camera, projector, CMOS image sensors, and many imaging and hand-held devices. Recent developments in plasmonics-based structural color filters can be expected as possible replacement of pigment-based color printing in the future. The structural color filter exhibits significant advantages over existing pigment-based technology, such as being compact in size, rendering non-degradable colors, having resolution well below the diffraction limit, and being environmentally friendly [45, 120]. The new technique of

*This chapter is published in Optics Express [52]

developing structural color devices based on femtosecond laser gives a new direction for the possibility of mass production [121].

Different approaches have been suggested to show the capability of structure-based color filtering, including metallic grating structures [103, 110], metallic disks [45, 70], complementary metallic design [84, 111], metalinsulatormetal (MIM) structures [122, 123], all-dielectric [50, 51, 121, 124], and hybrid structures [103, 125]. However, the main challenge is to design a tunable color filter. The capability of a structural color filter is limited owing to the fact that the response of the color filter is fixed once the device is fabricated. Recently, some research groups have demonstrated significant tunability of structural color filters by various means. A non-symmetric structure approach is used to tune the response based on polarization of incident light [51, 82, 84, 126]. Unfortunately, the tunability range of these devices is quite narrow, and it is very difficult to fabricate such structures. Other popular approaches rely on anti-bonding mode resonances [109] or MIM resonators [122] to tune the resonance wavelengths, but the size of the MIM-based devices are in the micron range, which is difficult to integrate with chips. It is obvious that tunable color filtering is still an open area of research. According to the literature, a couple of new techniques have been disclosed for tuning the color by means of hydrogen-responsive Mg nanoparticles [127] and mechanically stretchable substrates as active metasurfaces in dynamic plasmonic color display [128].

In this paper, we integrated the nematic liquid crystal (LC) with a simple aluminum (Al) grating metasurface. The cell thus formed shows significant spectral tunability by applying various voltages across the cell thickness. The reason to choose Al is its low interband transition loss, which can provide more vivid colors [115, 129]. LC has already been used to design active nanophotonics devices [130–133], beam-steering [134], tunable filters with microspheres [135], and phase-controlled all-dielectric metasurface [136] to achieve the tunability of resonance at near-infrared (NIR) wavelengths. An earlier attempt has also been made to enable the tunability of resonance in the visible range [137, 138]. However, the tunable color filter using aluminum metasurface in the visible range is less studied, in particular with the transmission mode. The working principle of our device is based on the fact that LC possesses both dielectric anisotropy and optical anisotropy, consequently exhibiting polarization tunability when a small electric field is applied across the LC. This anisotropic behavior can be easily manifested in a cell with twisted alignment of the LC. In a typical twisted-nematic cell, an applied voltage imposes an electric torque on the LC molecules against the restoring elastic one,

causing the molecular axis and, in turn, the optic axis of the LC to tilt toward the field direction. The tilted optic axis thus results in the change in effective refractive index. We utilized the anisotropic property of LC combined with an Al grating metasurface to realize the tunability of color filter.

5.2 Sample fabrication

The Al grating metasurfaces were fabricated using electron-beam lithography (EBL). To define a pattern, polymethylmethacrylate (PMMA) of 200 nm in thickness was coated on a typical indiumtin-oxide (ITO)-coated glass substrate followed by a patterning process. A 90 nm thin film of Al was deposited by using the E-gun evaporator. The Al gratings would be formed by lift-off process and they have the desired effect to align the contacting LC molecules to lie perpendicularly to the grating vector in the metasurface plane.

The ITO glass substrate with an Al grating metasurface serves as the bottom plate of the LC cell. The top plate of the cell is ITO glass spin-coated with a mechanically buffed polyimide layer for planar alignment of the LC molecules. The rubbing direction is parallel to the grating vector when assembled with a cell gap of 5 μm. The nematic liquid $n_e = 1.7472$ and ordinary refractive index $n_o = 1.5217$ at the temperature of 20° and wavelength of 589.3 nm, was introduced into each empty cell by capillary action. An alternating current (AC) voltage (1 kHz) was applied across the cell gap through ITO layers to control the state of LC. The schematic of the cell configuration is shown in Fig. 5.1. At null voltage, the polarization direction of linearly polarized light of normal incidence rotates by 90° after emerging from the cell through the polarization-rotation effect [139] in a twisted nematic cell as shown in Fig. 5.1(a). In Fig 5.1(b), by increasing the voltage to unwind the twist and maximize the tilt in the LC bulk, the polarization of linearly polarized light remains virtually unchanged, in perpendicular to the grating vector.

5.3 Spectral Characterization of Metasurfaces

For this work, the grating structures were designed with a fixed duty ratio of 0.5 and with three distinct widths: 150 nm, 200 nm and 230 nm. Figure 5.2(a) schematically depicts the design of a parallel-stripe-patterned grating characterized by the height h, width w and period (or grating constant) $P (P = 2w)$. Figure 5.2(b) shows a scanning

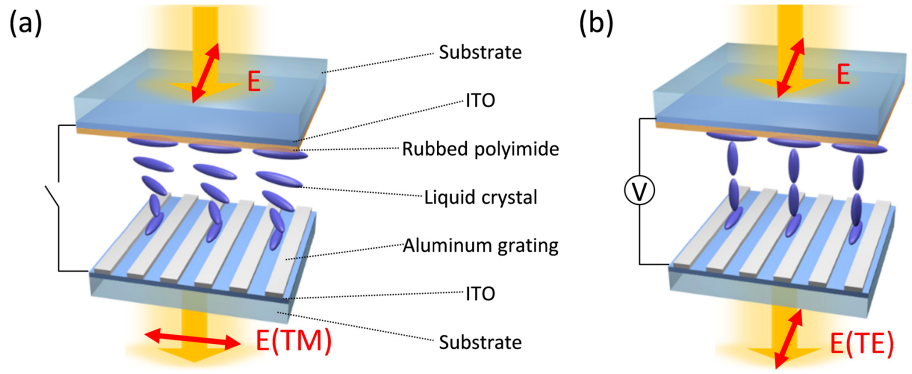

FIGURE 5.1: Schematic of the cell composed of sandwiched nematic LC, an Al grating and a polyimide-coated substrate in the (a) voltage-off and (b) voltage-on states.

electron microscope (SEM) image of one fabricated grating sample having = 90 nm, w = 150 nm and P = 300 nm.

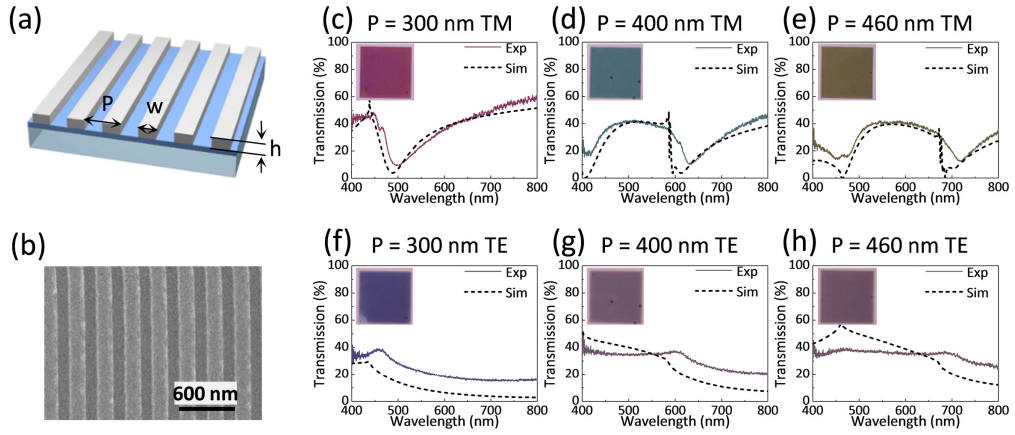

FIGURE 5.2: Schematic of the Al grating on the ITO coated glass substrate. (b) SEM image of aluminum grating with grating width 150 nm. The simulated and experiment transmission spectra of the aluminum grating when the incident light is (c)-(e) TM polarization and (f)-(h) TE polarization. The insets show the images directly recorded by optical microscopy with a camera.

Transmission spectra of each grating were then recorded for both TE and TM cases. All the collected data were normalized with respect to the bare ITO-coated glass substrate. A camera was used to take the micrographs of the illuminated area. Figure 5.2(c) to Fig. 5.2(e) show the comparisons of simulated and experimental spectra of the TM mode for three different grating structures. Note that the three insets show the correspondingly observed colors in transmission. Similar measurements were carried out for TE polarized light as shown in Fig. 5.2(f) to Fig. 5.2(h). The experimental spectra are in reasonable agreement with simulated data.

From Fig. 5.2 (c) to Fig. 5.2(e), it is clear that there are pronounced changes in the three transmission spectra for TM polarization so the change in color is dramatic and vivid. In contrast, the TE polarization produces featureless-like spectra, giving rise to limited change in color as shown in Fig. 5.2(f) to Fig. 5.2(h).

5.4 Modelling

In order to fit the experimental observation, simulations were performed by using finite difference time domain (FDTD) method, (FDTD Solutions, Lumerical). In the modeling, the LC molecules around the grating slits are parallel to the grating [140]. Therefore, for TE polarization, the vibration direction of incident optical electric field will be parallel to the molecular of the liquid crystal, and the effective refractive index of LC is $n_e = 1.75$. On the other hand, for the TM case, the vibration direction of electric field will be perpendicular to the molecular axis of the LC in the bulk, and the effective refractive index is $n_o = 1.75$.

Figure 5.3 shows the transmittance spectra of TE and TM polarizations with LC. By comparing Fig. 5.2(f) and Fig. 5.3(a), the resonance peak in the transmittance spectrum of TE polarization with LC is much higher and sharper than that of in air, so the color will be vivid in LC. In Fig. 5.3(a), the resonance peaks around 438 nm and 525 nm are diffraction signals given by [141]:

$$\lambda = Pn_i \tag{5.1}$$

where, $P = 300$ nm is the period of the grating and n_i is the refractive index of the surrounding medium of the grating. In TE polarization, the prime effect is diffraction and waveguide mode resonance [142], so the extraordinary transmission peaks in Fig. 5.3(a) would be influenced by the refractive index of the surrounding medium. Since the refractive indices of the substrate $n_{sub} = 1.46$ and of the LC $n_e = n_{lc} = 1.75$, there are two peaks at 438 nm and 525 nm. On the other hand, if the refractive index of substrates and liquid crystals could match, the narrower transmission band could be achieved.

In Fig. 5.3(b), the broad band resonance dip spanning from 460 nm to 484 nm is due to the plasmon resonance for TM polarization [142], which is given by [141]:

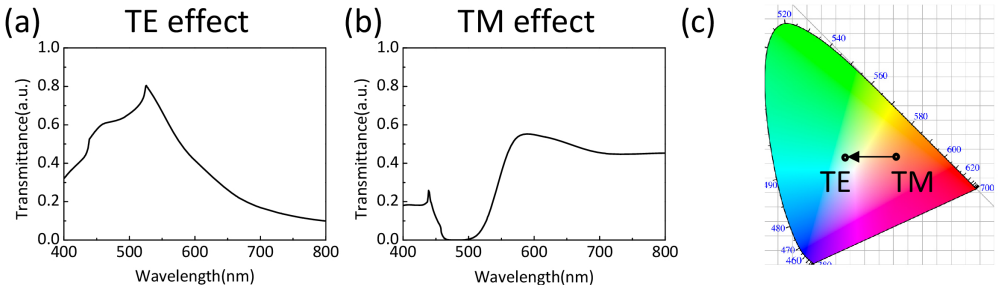

FIGURE 5.3: Simulated transmission spectra of an Al grating integrated with LC for $P = 300$ nm: (a) TE polarization; (b) TM polarization. (c) Change in color from TM to TE polarization as indicated by the color space coordinates on the CIE-1931 chromaticity diagram.

$$\lambda = P\sqrt{\frac{\epsilon_m \epsilon_i}{\epsilon_m + \epsilon_i}} \tag{5.2}$$

where ϵ_m and ϵ_i are dielectric permittivity of metal and surrounding medium, respectively. In TM polarization, the transmittance is near zero from 460 nm to 484 nm because the grating structures would provide the extra k-vector to excite surface plasmon polaritons [142]. We observed two resonance dips at 460 nm and 484 nm corresponding to the substrate ($\epsilon_i \cong 1.46^2$) and the LC ($\epsilon_i \cong n_o^2 \cong 1.52^2$) resonance wavelengths are close to each other, so the two resonance dips coalesce together to form a broadband resonance dip. A CIE-1931 chromaticity diagram is shown in Fig. 5.3(c) to help visualize the switch of color from TM to TE polarization.

5.5 Tunability of colors

Figure 5.4 shows the experimental results of Al gratings integrated with LC. The polarization direction of incident light is parallel to the grating stripes. When the applied voltage is 0 V, the polarization direction of electric field on the Al grating is twisted by 90° and changed to become parallel to the grating vector through the LC bulk. Because of the unperturbed twisted-nematic state of LC configuration, the TM polarization effect could be achieved when the applied voltage is 0 V in this framework. In contrast, the TE polarization effect could be achieved when the applied voltage is higher than 4 Vrms because the LC molecules are reoriented vertically to the substrate by the externally applied voltage across the cell thickness to permit the polarization state of light uninfluenced or untwisted in the passage through the cell. This is the key to enabling active tuning of color in our device.

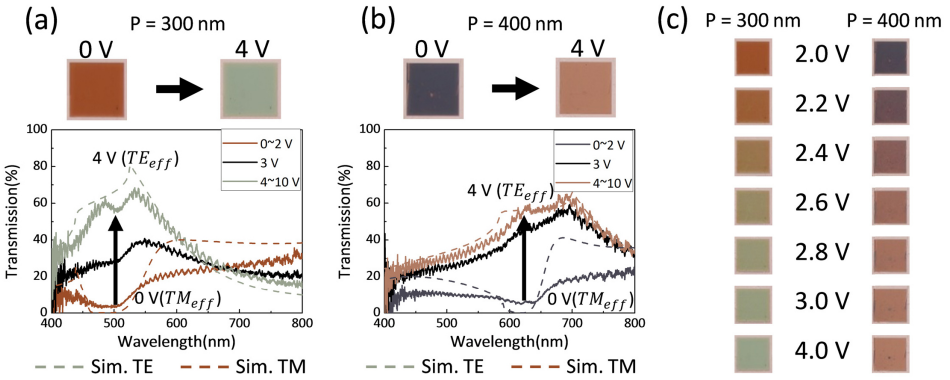

FIGURE 5.4: Experiment results of LC cells with Al gratings when the applied voltage increases from 0 V to 10 V_{rms}. The images on the top of spectral are optical images recorded by a CCD camera: (a) $P = 300$ nm (b) $P = 400$ nm. (c) Transmissive color appearance of the cells at various applied voltages.

By changing the state of LC using a small applied voltage, the color changed along with the TE and TM polarizations. The variations in color and spectrum with increasing voltage for two different grating constants are shown in Fig. 5.4(a) and Fig. 5.4(b). One can see that, with a small applied voltage, the spectrum and, in turn, color of the cells can be varied. The change from the corresponding the TM mode at 0 V to the TE mode at 4 V_{rms} thus provides dynamic color tunability. In Fig. 5.4(c), the gradual color variation is demonstrated with the applied voltage from 2 V_{rms} to 4 V_{rms}. When the applied voltage is larger than 4 V_{rms}, the color would freeze, because the molecules of LC are untwisted and totally aligned vertically.

5.6 Conclusion

In conclusion, we have demonstrated a LC-based tunable color filter, which shows high dynamic tunability of color in transmission. The integration of LC with a grating structure allows the broad dynamic tunability in quite controllable manner. By slightly adjusting the applied voltage between 2 V_{rms} and 4 V_{rms}, the color spectra changed in a reasonably broad spectral range. The concept can be extended for integrating LC with plasmonics or all dielectric metasurface-based color filters to achieve the high quality of color pixels. The integration of LC with color filters opens a new possibility to make tunable color filter devices.

Chapter 6

Light channeling and guiding using surface modification*

A general approach to localization, guiding and redirecting light in photonic waveguides via tailoring their interfaces (surfaces) is proposed. The approach is demonstrated for dielectric rod-type photonic crystal slabs, whose regular and defect parts are only distinguished by whether the nanocylinders are covered by metal caps or not. Thus, the rod-array part of the structure is not changed, while the local modifications are only applied to the interfaces. The basic functionalities, i.e., localized wave guiding, bending, and splitting are achievable using this approach. Selective dual-mode operation is possible due to co-existence of a defect mode and a chainlike mode in one structure.

6.1 Introduction

Recently, new mechanisms of controlling propagation in optical and microwave waveguides with planar covers at the interfaces attracted a lot of attention. In particular, optical waveguides covered by gradient metasurfaces [143] and microwave waveguides covered by uniform (non-gradient) metasurfaces [144] have been proposed. Propagation conditions of the original non-covered waveguides can be strongly modified and some new modes may appear, while only modifying the interfaces.

*This chapter is published in Optics Letters [53]

At the same time, there are various waveguiding structures used at optical frequencies. Among them, finite-thickness, rod/disk- and hole-type photonic crystals (PhCs) with and without geometrical defects, which are known as PhC slabs, have been the focus of interest in the two last decades [145–149]. Localization within line or point defects may occur due to defect modes, which appear in the stop bands of the corresponding defect-free structures. They enable efficient waveguiding, splitting, and bending, e.g., see [150–154]. Chain waveguides which use coupled dielectric, metallic, or metallo-dielectric resonant particles, or single-row hole arrays should also be mentioned in this concern [155–160]. Very recently, a new approach to the localized wave guiding has been proposed, which is realized by using a quasi-planar PhC slab with topologically protected states [161].

Conceptually, the approach suggested in this Letter is based on the use of surface defects introduced at the interface between waveguide and surrounding media, which may yield propagating volume defect modes. For validation purposes, we consider a dielectric rod-type PhC slab with the wave guiding capability, whose regular part's rods are covered by metal caps to achieve a stop band, while some rods remain uncovered to create a defect-mode waveguide. Thus, the boundary conditions at the interfaces of the regular and defect parts of the rod array are different. It will be shown how the waveguide-covering approach [143, 144], defect-mode waveguiding in PhC slabs [145, 146, 150], and wave guiding by chains [155, 156] can be efficiently combined in one device. The goal here is proof of concept. Design optimization is beyond the scope, as well as a use of surface waves and their hybridization with volume waves.

Compared to the earlier works on waveguide covering [143, 144], our approach may enable a defect-mode waveguiding and wave re-directing, e.g., bending and splitting. In contrast with the conventional PhC slabs [145, 146, 150], structures built on the suggested principles do not need any local internal modification to create a defect-mode waveguide. We demonstrate here that the basic functionalities realizable in the conventional (i.e., noncovered) PhC slab waveguides with defects can be replicated just via local modification of the interfaces. They include the localized wave guiding, splitting, and bending. Moreover, there are two distinguishable operation modes, both enabling localization, while re-direction is only allowed by one of them. The first mode is similar to the classical defect modes in PhC slab waveguides. The second one is associated with a waveguiding by a chain, while the regular part of PhC slab exerts a relatively weak effect. From the chain waveguide perspective, this regime is unusual, because the chain

waveguide is *embedded* into another structure with a waveguiding capability. It will be shown how the difference in properties of the first and the second mode is connected with the achievable functionality. The obtained results will also be discussed from the multifunctionality perspective.

6.2 Results and discussions

The main idea is illustrated by Fig. 6.1, upper panel. Some quasi-planar elements (denoted by A_{ij}) are assumed to cover the interfaces of the waveguide with the surrounding media in stepwise manner for local control of propagation. For demonstration, we use a rod-type PhC slab, i.e., an array of finite-height dielectric nanocylinders [146, 148, 149]. Then, we modify it by placing the metal caps at the top and the bottom of each nanocylinder that belongs to the regular part of the structure, as shown in Fig. 6.1, lower panel. Without the caps, such a PhC slab can support propagation of electromagnetic waves [146]. Hence, the non-capped rods may be used to create a defect in the periodic capped array. The height of nanocylinders is taken as $t_s = 200$ nm and the radius as 60 nm; period of the square lattices is 300 nm. The index of refraction of nanocylinder material is 3.46, what is close to Si at optical frequencies. Metallic caps are 20 nm thick and made of Au (permittivity dependence on frequency, f, is taken from [162]). The surrounding medium is considered as air for simplicity. Simulations are performed by using Lumerical, a commercial FDTD solver [44].

Dispersion has been calculated for a unit cell of the infinite capped structure, see insert in Fig. 6.2, right panel. Bloch boundary conditions in (x,z) and (y,z) planes and perfect matching layer (PML) boundary conditions below and above the structure were used. Vertical dipoles were randomly located in the unit cell to excite the TM modes only. The calculated band diagram is presented in Fig. 6.2, right panel. In addition to the conventional bands being sensitive to the variations of wavevector $\mathbf{k}$, there are nearly flat bands between $f = 420$ THz and 500 THz. Similar bands may exist in metal-rod [163] and excitonic [164] PhCs. As shown below, the nearly flat bands being located between the conventional bands do not affect the resulting transmission.

Next, we calculate transmittance (T) spectra for two finite-extent PhC slabs by using open boundary conditions in the z-direction, and PML conditions in the x and y direction. For the first one, all the rods are capped, i.e., there is no geometrical defect. For the second one, the central row of the rods is non-capped, like in Fig. 6.1, bottom

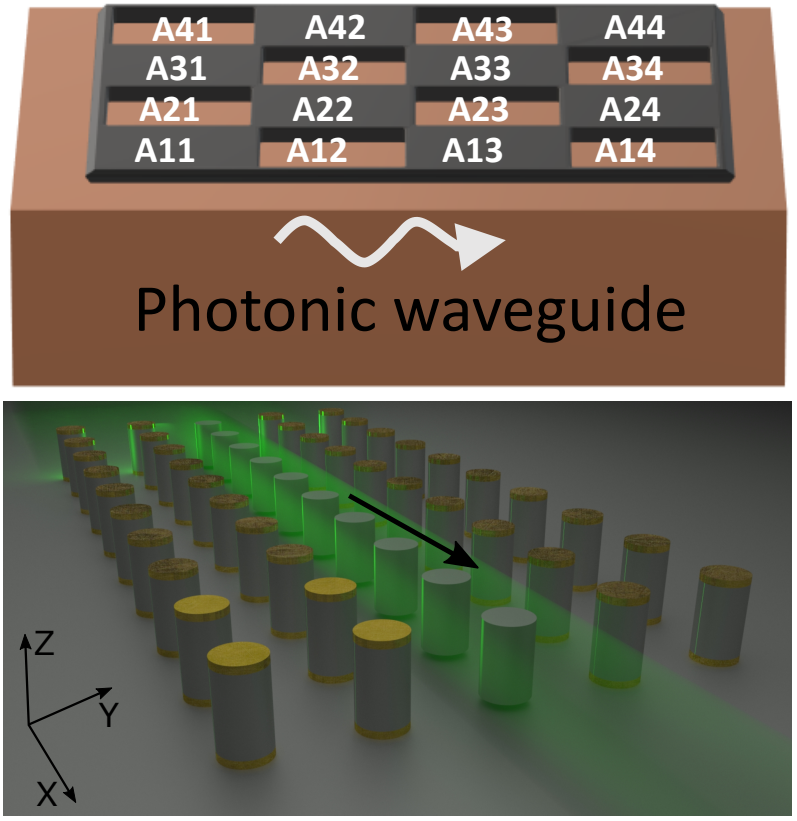

FIGURE 6.1: Upper panel: A general schematic of a photonic waveguide with the interface covered with different quasi-planar elements in a stepwise manner; A_{ij} denote quasi-planar elements with different electromagnetic properties; here $1 \leq i \leq 4$, $1 \leq j \leq 4$ but number of elements may be arbitrary, and parts of them may be the same. Lower panel: Artistic view of the PhC slab defect-mode waveguide created by the difference between the regular (capped) part of the structure and the central row composed of non-capped rods.

panel. Hence, defect-mode related localization and transmission may be expected, despite of the dielectric nanocylinders being the same for all rows. 20 unit cells in the x-direction and 9 unit cells in the y-direction were taken. A TM polarized broadband Gaussian beam source has been placed at the input of the line defect, and its maximum adjusted with the defect mid-planes, $y = 0$, $z = 0$. The results of full-wave simulations are presented in Fig. 6.2, left panel.

The transmittance results for the defect-free structure have been compared with the ones for the structure with the straight line defect in Fig. 6.2, left panel. In case of the defect-free structure, transmission is blocked between $f = 415$ and 475 THz. This behavior is in good coincidence with the dispersion results in Fig. 6.2, right panel. Moreover, as follows from the comparison of the transmittance spectra and the band structure, there is no signature of contribution of the (nearly) flat bands to the transmission for the defect-free structure, i.e., we obtain a wide stop band, as desired. Comparing the spectra for the structures with and without defect, one can observe two distinguishable

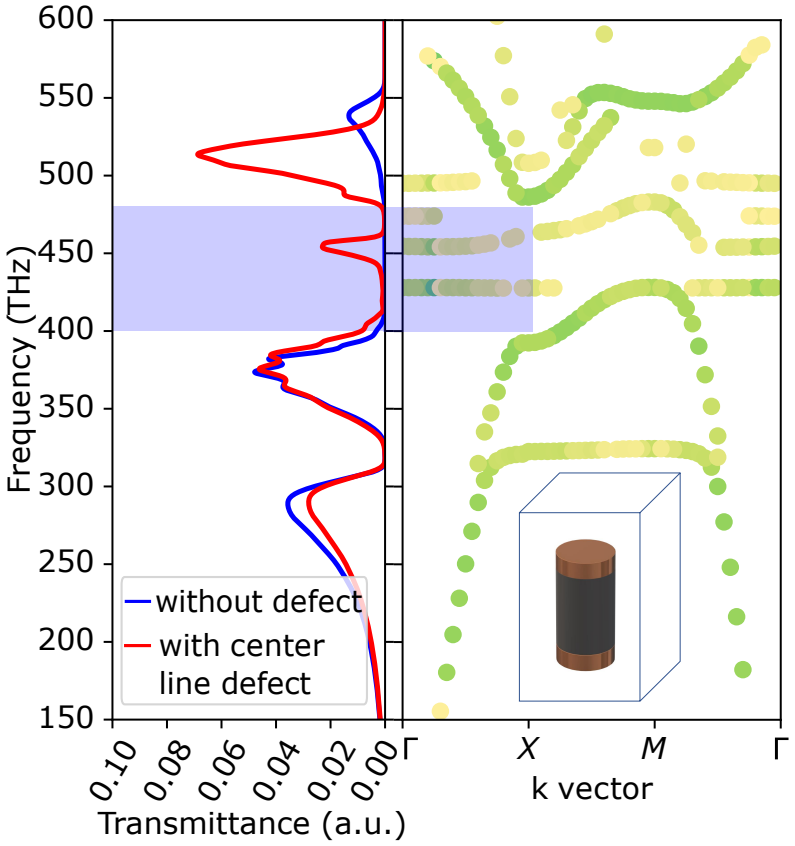

FIGURE 6.2: Right panel: Band diagram of the infinite defect-free PhC slab comprising the unit cells, every representing a dielectric nanocyliner capped with metal nanodisks at the top and the bottom, see the inset. Light-blue shaded area schematically shows spectral location of the gap between **k**-sensitive bands for propagation along $\Gamma - X$-direction (corresponding to the x axis). Left panel: Transmittance spectra (T vs. f) of the studied PhC slab with (red line) and without (dark-blue line) defect.

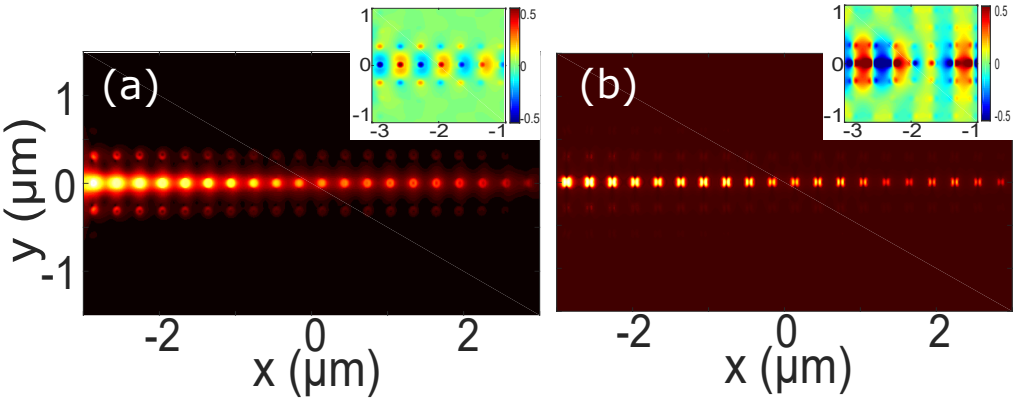

FIGURE 6.3: Spatial distribution of the power at mid-height of PhC slab with a straight line defect in the structure comprising 20×9 unit cells, at (a) 453 THz and (b) 513 THz; excitation is from the left side. Insets show amplitude of E_z component within 7×7 unit cell fragment, being closest to the source.

maxima, which appear owing to the line defect, being located at 453 THz and 513 THz. The first maximum is associated with a defect mode, since transmission in the defect-free structure is blocked within this spectral range, while the nearly flat bands only occur in dispersion. The second peak lays in the spectral range, where conventional **k**-sensitive

bands do exist. It is noticeable (and expectable) that transmissions in the structures with and without defects well coincide below 400 THz. On the contrary, the second maximum at 513 THz surprisingly shows a higher magnitude than in the defect-free structure in the same frequency range. Therefore, the origin of the second maximum may be not trivial, and it will be clarified below.

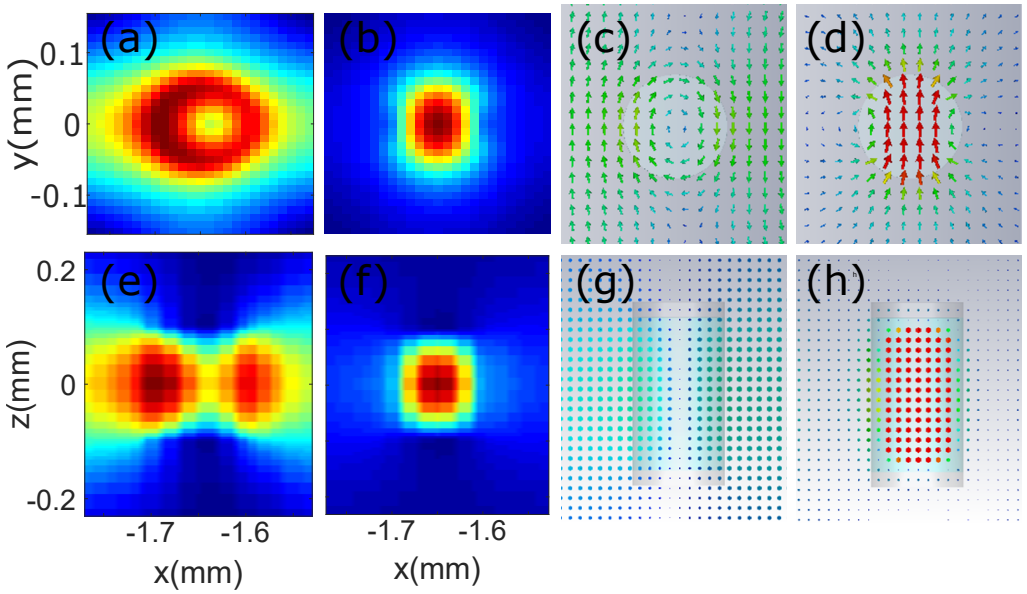

FIGURE 6.4: Map of magnitude of magnetic field in the (x,y)-plane at (a) 455 THz and (b) 513 THz, and in the (x,z)-plane at (e) 455 THz and (f) 513 THz (main structure). Quiver map of magnetic field vector in the (x,y)-plane at (c) 459.5 THz and (d) 520 THz, and in the (x,z)-plane at (g) 459.5 THz and (h) 520 THz (auxiliary structure). Frequencies are taken at the maxima of T.

Figure 6.3 presents the power map at the nanocylinder mid-height ($z = 0$) within the whole structure, which comprises 20×9 unit cells. One can see that localization and defect-mode waveguiding in the centered line channel, which is created by the non-capped rods, may occur at the both maxima of T, despite the above-mentioned differences. It is evident that defect-mode waveguiding can be obtained while the interfaces of the rods are only modified. For further clarity, we consider the field behavior within the unit cell of the central row, which is the second one from the source side. The field monitors were centered with respect to the mid-plane of the non-capped row of the rods. Figure 6.4(a,b,e,f) shows color maps of H field, at the two maxima of T, which are obtained by using Lumerical software [44]. The difference is clearly seen, which may lead to different capability in directional selectivity. Since Lumerical software is not well suitable to plot quiver maps required for identification of the contributing resonances, we also used an auxiliary structure with the same dominant physics. For this structure, quiver maps can be easily obtained by using CST Microwave Studio, another commercial software, in the waveguide-port excitation mode [165]. The auxiliary structure comprises

3×3 unit cells. Frequencies are slightly shifted as compared to the main (20×9) structure, in order to stay at the maxima of T. Results are presented in Fig. 6.4(c,d,g,h), being in appropriate coincidence with the ones in Fig. 6.4(a,b,e,f). One can see that TM mode with zero azimuthal index, $m = 0$, is dominant at the first maximum of T. At the second one, TM mode with $m = 1$ is dominant. Stronger asymmetry in the color map in Fig. 6.4(a) as compared to Fig. 6.4(c) is the only significant difference. However, similar behavior is observed also in the auxiliary structure but for the first rod from the source side. Indeed, deviations from the canonical modal profiles are weakening in both the main and auxiliary structures, if the distance from the edges is large enough. The mode corresponding to the first maximum shows no specific directional selectivity and, thus, is expected to be appropriate for bending. The mode corresponding to the second maximum yields a dipole array, so it might be not appropriate for bending.

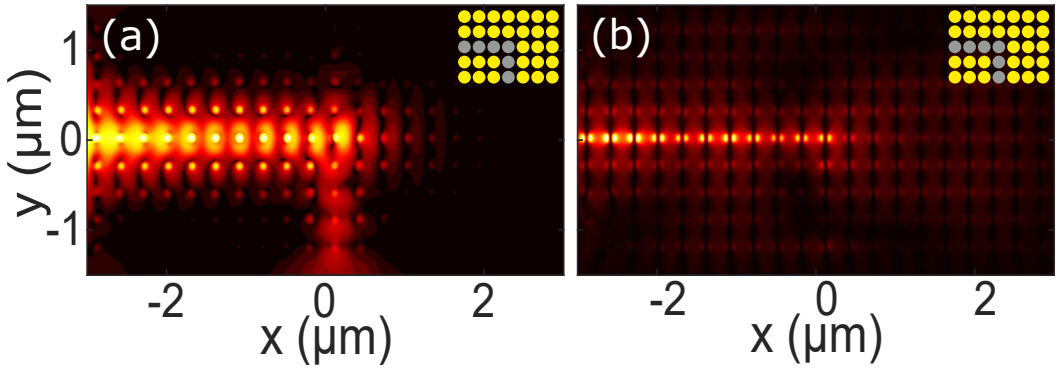

FIGURE 6.5: Same as in Fig. 6.3 but for the L-shaped waveguide.

To check the guess regarding directional selectivity of the first and the second mode, we simulated transmission in an L-shaped defect waveguide. It differs from the waveguide in Fig. 6.3 only in that the single non-capped row is bent now. The results are presented in Fig. 6.5. It is observed that the first mode enables bending, while transmission for the second mode into the bent arm is blocked. This behavior is in agreement with the prediction based on the results in Fig. 6.4. Indeed, only the mode in the gap between the regular bands, which is a mode with $m = 0$ (or its perturbed version), is appropriate for bending.

Now, let us clarify the origin of the second mode. Note that we do not observe strong power in the capped region in Fig. 6.3(b) and 6.5(b), whereas T in the case with defect is significantly larger at 513 THz than in the case without defects, see Fig. 6.2, left panel. Thus, it may be expected that a chainlike mode appears here and dominates a regular mode of the capped array, which may appear in this spectral regime, according to the dispersion shown in Fig. 6.2, right panel.

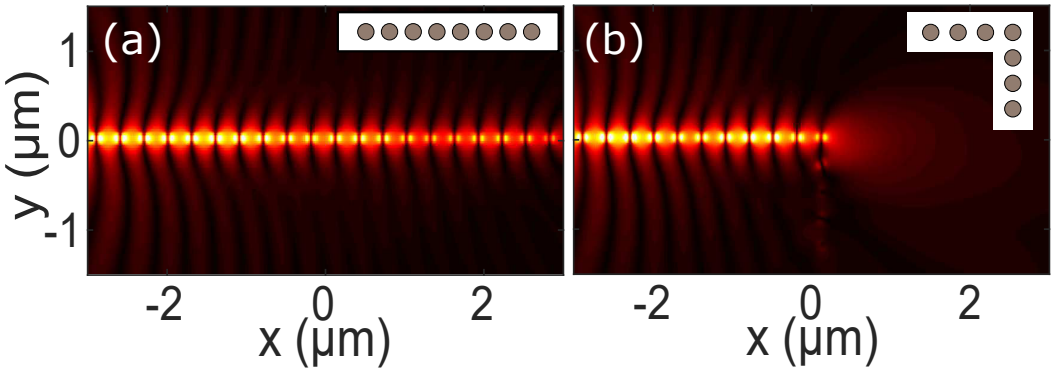

FIGURE 6.6: Spatial distribution of power at nanocylinder mid-height ($z = 0$) for (a) straight single-row chain and (b) L-shaped chain of nanocylinders, both at 513 THz; insets schematically show chain composition.

For comparison, Figs. 6.6(a) and 6.6(b) present power distribution for two chain waveguides, which are created by fully removing the capped (regular) part from the structures in Figs. 6.3 and 6.5, respectively. The qualitative coincidence between Fig. 6.6(a) and Fig. 6.3(b), and between Fig. 6.6(b) and Fig. 6.5(b) is quite good. Moreover, there is good coincidence in spectral location of the T maximum at 513 THz between the case with defect in Fig. 6.2, left panel and the chain in Fig. 6.6(a) (not shown). Hence, it is clear that transmission in Fig. 6.2, left panel and power maps in Figs. 6.3(b) and 6.5(b) at 513 THz is connected with the chainlike mode, while the surrounding regular part affects neither the basic modal features nor the achieved functionality. Indeed, there are some differences in power maps that may lead to different Q-factors, but the principal possibility of either wave guiding or blocking transmission is not changed.

It is noteworthy that bending in the chains like that in Fig. 6.6(b) may be possible while using, for instance, whispering-gallery modes [166]. It typically results in a substantially larger electrical size of the resonant particles, which can be inconsistent with the spectral range of lower-order modes of the PhC slab. It is also noticeable that, in contrast with [157], waveguiding in the straight chain waveguide in Fig. 6.6(a) is obtained by using the rods having much lower permittivity.

The detected modal selectivity has also been examined for a + (plus) shaped waveguide. For the first mode, when the incidence is from one of four arms of the structure (here – the left horizontal arm), we obtain wave guiding in the remaining three arms. Hence, we have splitting. For the second mode, wave guiding occurs only in one of those three arms, which is a straight continuation of the incidence arm. There is no splitting

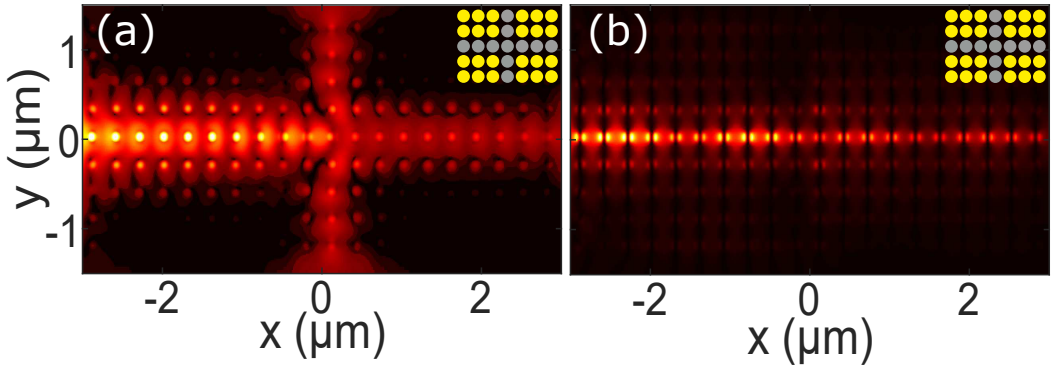

FIGURE 6.7: Same as in Fig. 6.3 but for the + shaped waveguide.

in this case, in line with the above discussed modal properties. Co-existence of the defect and chainlike modes in one structure enables also *multifunctional operation*. Multifunctionality may mean merging and superposition of two different functions at fixed f [167, 168], functionality depending on polarization [169], different (either merged or not merged) functions at different f [170–172], etc. From this perspective, the suggested approach may allow splitting or bending at one operating frequency and, respectively, non-split regime or blockage of transmission at the other, as shown in Figs. 6.7 and 6.5. For the dual-frequency mixtures of optical signals, selective bending in the structure in Fig. 6.5 can be used for sorting of the arriving signals. Selective splitting in the structure in Fig. 6.7 enables a partial demultiplexing. This regime can also be obtained in a T-shaped waveguide. At the next steps of this research program, local modification of the interfaces and, thus, boundary conditions in hole-type PhC slabs will be studied and dynamically tunable components, e.g., made of graphene, vanadium dioxide, will be introduced. The selectivity demonstrated by the presented results may open a route to multifunctional applications for a wide class of the structures built on the same principles.

6.3 Conclusion

To summarize, we demonstrated the potential of the approach based on local modification of the external boundary conditions of the PhC slab waveguide in obtaining light localization, guiding, splitting, and bending. It is shown that all of the above-mentioned functionalities of a photonic waveguide can be obtained in the defect-mode regime without any modification of the main, i.e., rod-array part of the structure. Rather, the modifications are needed to obtain stepwise changes in the boundary conditions, which are realized here by using thin metallic disks. Similar modifications can be achieved by

using other interface elements and the approach is applicable to rather arbitrary photonic waveguides. Due to the fact that the defect mode co-exists in the same structure with the chain-like mode which dominates the modes of the defect-free structure, dual-band operation can be realized, in which the functionalities are dependent on the used mode. A simultaneous use of the both modes can be prospective for multifunctional operation.

Chapter 7

Conclusions

The most of the research presented in the thesis was performed in the framework of the project funded by National Science Center Poland, Grant No 2015/17/B/ST3/00118 (Metasel): *Theoretical basics of metasurface based quasi-volumetric structures for future multifunctional photonics and microwave devices*, coordinated by dr Andriy E. Serebryannikov. I started my investigations from the understanding of the theoretical basics needed to design metasurfaces which can operate as color filters, already during my research work with Prof. Ravi Hedge at IIT Gandhinagar, India. My previous experience in simulations of the dielectric resonator microwave antennas gave me the insight to dielectric nanoantenna design. I performed simulations and made an experiment to validate the numerical results. Fortunately, experimental results match quite well with theoretical results and I was able to demonstrate the design of all-dielectric based color filters. Thus, Chapter 3 and Chapter 4 are devoted to the study of color filter design. In Chapter 3, I presented design and results for metasurfaces operating as color filters, which are based on cross-shaped silicon nanoantennas (nanoresonators). In order to obtain the desired functionality, I studied the Mie resonances of polarisation insensitive cross-shaped nanoresonators. The designed device is capable to produce high-quality colors in reflection mode with the extended gamut on the CIE chart. The extended gamut response is very important to achieve high-quality vivid colors. In Chapter 4, I extended my research work to design a tunable color filter, as compared to static color filters presented in Chapter 3. I used high index material (Si), which allows to confine the energy within the nanoresonators. I presented a non-symmetric nanoresonator design so that the response of the color filter is sensitive to the polarisation of the source.

In Chapter 5, I extended my research towards tunable color filters, which are another interesting topic of research. Thanks to prof. Chen group from NCTU Taiwan, I started working on the integration of LC with static (non-tunable) color filters to design tunable color filters. LC can change the refractive index in the presence of an electric field. This gives new possibilities to design tunable color filters by embedding the Al gratings into the LC. The performed research is unique in the sense that small biasing voltage results in vivid colors in reflection mode.

In the second-last chapter (Chapter 6), I explored the metasurfaces concept to design photonic crystal slab (PhC) waveguide by modification of its surface. The work presented up to Chapter 5 was devoted to control the transmission or reflection in case of normal incidence. In Chapter 6, I exploited a new mechanism to control in-plane propagation in the PhC waveguide by using metasurfaces. I used the surface impedance modification approach to control in-plane propagation of volume modes in the PhC waveguide. We showed that the four key properties controlling the propagation of the light, i.e., amplitude, phase, polarisation, and optical impedance, can be manipulated by a properly designed metasurface.

7.1 Outlook

In my thesis, I present the results of design, fabrication, and experimental study of the selected metasurface based devices. The work done made a progress towards the integrated photonics components, which is the future demanding area. Current research in the direction of color filters is the pre-mature stage and it still requires significant research and development to implement it at the product level. An important purpose of research is to achieve independent hue, saturation, and brightness for enabling the effective utilization of color filters in dynamic display applications [173]. This can open the possibilities to design ultra-thin displays with sub-wavelength resolution. Also, there is a need to develop a plateform to directly fabricate the color filters on photo-detector with high precision [174]. This can make it suitable for imaging applications and all-dielectric metasurfaces presented in the thesis are a timely and significant contribution to this direction. There is also an extensive research scope in the direction of tunable color filter design. It can be achieved by electronic means [122], thermal process, or by oxidation [175]. Our proposed method of LC integration with color filters is one more possibility in this direction.

Another important aspect of research is to figure out new way to fabricate color filters at large scale. Most of the known demonstrations of color filters is presented at a very small area due to the use of electron beam lithography (EBL) for fabrication, which limits the area size. Indeed, the EBL technique is not suitable for the mass production of such devices, so that a further technological advancement is required. Soft imprint lithography and self-assembly techniques might be suitable for large area fabrication [86, 176–178]. This can be used to design high-resolution long-lasting paintings.

Regardless of the color filter applications, there is an extensive scope of research for controlling the in-plane propagation by using metasurfaces [48]. The surface impedance approach (as discussed in Chapter 6) can be used, for instance, to design (de-)multiplexers, mode converters, and modulators. Interestingly, the concept of the metasurface controlled impedance of the waveguide surface can be further extended by using a thin layer of 2D materials, like graphene.

Overall, the potential of metasurfaces is very broad and that opens the opportunities in the new prospective directions of research. Moreover, the concept of metasurfaces may be exploited to design image processing devices [179] and neural network front-ends [180], for artificial intelligence machine learning [181], and in quantum optics [182, 183]. I believe that the research presented in this thesis and the papers published in 4 international journals will push forward the research and design of metasurfaces for these applications.

Publications

1. **Vashistha V**, Krawczyk M, Serebryannikov AE, Vandenbosch GA, "Light guiding, bending, and splitting via local modification of interfaces of a photonic waveguide", Optics Letters, 2019 Oct 1, 44(19), 4725-8.

2. Zelent M, Mailyan M, **Vashistha V**, Gruszecki P, Gorobets OY, Gorobets YI, Krawczyk M, "Spin wave collimation using a flat metasurface", Nanoscale, 2019, 11(19), 9743-8.

3. Xie ZW, Yang JH, **Vashistha V**, Lee W, Chen KP, "Liquid-crystal tunable color filters based on aluminum metasurfaces", Optics Express, 2017 Nov 27, 25(24), 30764-70.

4. **Vashistha V**, Vaidya G, Gruszecki P, Serebryannikov AE, Krawczyk M, "Polarization tunable all-dielectric color filters based on cross-shaped Si nanoantennas", Scientific Reports, 2017 Aug 14, 7(1), 8092.

5. **Vashistha V**, Vaidya G, Hegde RS, Serebryannikov AE, Bonod N, Krawczyk M, "All-dielectric metasurfaces based on cross-shaped resonators for color pixels with extended gamut", ACS Photonics, 2017 Apr 11, 4(5), 1076-82.

Bibliography

[1] A. I. Kuznetsov, A. E. Miroshnichenko, Y. H. Fu, J. Zhang, and B. Luk'yanchuk, "Magnetic light," *Scientific Reports*, vol. 2, p. 00492, 2012.

[2] N. Yu and F. Capasso, "Flat optics with designer metasurfaces," *Nature Materials*, vol. 13, no. 2, pp. 139–150, 2014.

[3] N. Yu, P. Genevet, M. A. Kats, F. Aieta, J.-P. Tetienne, F. Capasso, and Z. Gaburro, "Light propagation with phase discontinuities: generalized laws of reflection and refraction," *Science*, vol. 334, no. 6054, pp. 333–337, 2011.

[4] J. B. Pendry, "Negative refraction makes a perfect lens," *Physical Review Letters*, vol. 85, no. 18, p. 3966, 2000.

[5] L. D. Landau, J. Bell, M. Kearsley, L. Pitaevskii, E. Lifshitz, and J. Sykes, *Electrodynamics of continuous media*, vol. 8. elsevier, 2013.

[6] J. B. Pendry, A. Holden, W. Stewart, and I. Youngs, "Extremely low frequency plasmons in metallic mesostructures," *Physical Review Letters*, vol. 76, no. 25, p. 4773, 1996.

[7] J. B. Pendry, A. J. Holden, D. J. Robbins, W. Stewart, *et al.*, "Magnetism from conductors and enhanced nonlinear phenomena," *IEEE Transactions on Microwave Theory and Techniques*, vol. 47, no. 11, pp. 2075–2084, 1999.

[8] D. R. Smith, S. Schultz, P. Markoš, and C. Soukoulis, "Determination of effective permittivity and permeability of metamaterials from reflection and transmission coefficients," *Physical Review B*, vol. 65, no. 19, p. 195104, 2002.

[9] J. Zhou, T. Koschny, M. Kafesaki, E. Economou, J. Pendry, and C. Soukoulis, "Saturation of the magnetic response of split-ring resonators at optical frequencies," *Physical Review Letters*, vol. 95, no. 22, p. 223902, 2005.

[10] Y. Liu and X. Zhang, "Metamaterials: a new frontier of science and technology," *Chemical Society Reviews*, vol. 40, no. 5, pp. 2494–2507, 2011.

[11] V. M. Shalaev, "Optical negative-index metamaterials," *Nature photonics*, vol. 1, no. 1, p. 41, 2007.

[12] C. Rockstuhl, C. Menzel, T. Paul, T. Pertsch, and F. Lederer, "Light propagation in a fishnet metamaterial," *Physical Review B*, vol. 78, no. 15, p. 155102, 2008.

[13] X. Jia and X. Wang, "Optical fishnet metamaterial with negative, zero, positive refractive index and nearly perfect absorption behavior at different frequencies," *Optik*, vol. 182, pp. 464–468, 2019.

[14] C. M. Soukoulis and M. Wegener, "Past achievements and future challenges in the development of three-dimensional photonic metamaterials," *Nature Photonics*, vol. 5, no. 9, p. 523, 2011.

[15] M. Choi, S. H. Lee, Y. Kim, S. B. Kang, J. Shin, M. H. Kwak, K.-Y. Kang, Y.-H. Lee, N. Park, and B. Min, "A terahertz metamaterial with unnaturally high refractive index," *Nature*, vol. 470, no. 7334, p. 369, 2011.

[16] Z. Wang, F. Cheng, T. Winsor, and Y. Liu, "Optical chiral metamaterials: a review of the fundamentals, fabrication methods and applications," *Nanotechnology*, vol. 27, no. 41, p. 412001, 2016.

[17] S. A. Ramakrishna, "Physics of negative refractive index materials," *Reports on Progress in Physics*, vol. 68, no. 2, p. 449, 2005.

[18] B. Xiong, L. Deng, R. Peng, and Y. Liu, "Controlling the degrees of freedom in metasurface designs for multi-functional optical devices," *Nanoscale Advances*, vol. 1, no. 10, pp. 3786–3806, 2019.

[19] S. M. Kamali, E. Arbabi, A. Arbabi, and A. Faraon, "A review of dielectric optical metasurfaces for wavefront control," *Nanophotonics*, vol. 7, no. 6, pp. 1041–1068, 2018.

[20] D. Neshev and I. Aharonovich, "Optical metasurfaces: new generation building blocks for multi-functional optics," *Light: Science & Applications*, vol. 7, no. 1, pp. 1–5, 2018.

[21] H.-T. Chen, A. J. Taylor, and N. Yu, "A review of metasurfaces: physics and applications," *Reports on Progress in Physics*, vol. 79, no. 7, p. 076401, 2016.

[22] A. Y. Zhu, A. I. Kuznetsov, B. Lukyanchuk, N. Engheta, and P. Genevet, "Traditional and emerging materials for optical metasurfaces," *Nanophotonics*, vol. 6, no. 2, pp. 452–471, 2017.

[23] P. Genevet, F. Capasso, F. Aieta, M. Khorasaninejad, and R. Devlin, "Recent advances in planar optics: from plasmonic to dielectric metasurfaces," *Optica*, vol. 4, no. 1, pp. 139–152, 2017.

[24] S. A. Maier, *Plasmonics: fundamentals and applications*. Springer Science & Business Media, 2007.

[25] N. Meinzer, W. L. Barnes, and I. R. Hooper, "Plasmonic meta-atoms and metasurfaces," *Nature Photonics*, vol. 8, no. 12, p. 889, 2014.

[26] S. Pancharatnam, "Generalized theory of interference and its applications," in *Proceedings of the Indian Academy of Sciences-Section A*, vol. 44 (6), pp. 398–417, Springer, 1956.

[27] G. Zheng, H. Mühlenbernd, M. Kenney, G. Li, T. Zentgraf, and S. Zhang, "Metasurface holograms reaching 80% efficiency," *Nature Nanotechnology*, vol. 10, no. 4, p. 308, 2015.

[28] J. Zhang, M. ElKabbash, R. Wei, S. C. Singh, B. Lam, and C. Guo, "Plasmonic metasurfaces with 42.3% transmission efficiency in the visible," *Light: Science & Applications*, vol. 8, no. 1, p. 53, 2019.

[29] G. Mie, "Beiträge zur optik trüber medien, speziell kolloidaler metallösungen," *Annalen der Physik*, vol. 330, no. 3, pp. 377–445, 1908.

[30] P. J. Wyatt, "Light scattering and the absolute characterization of macromolecules," *Analytica Chimica Acta*, vol. 272, no. 1, pp. 1–40, 1993.

[31] "https://github.com/scottprahl/miepython."

[32] P. R. Wiecha, "pygdma python toolkit for full-field electro-dynamical simulations and evolutionary optimization of nanostructures," *Computer Physics Communications*, vol. 233, pp. 167–192, 2018.

[33] M. Decker, I. Staude, M. Falkner, J. Dominguez, D. N. Neshev, I. Brener, T. Pertsch, and Y. S. Kivshar, "High-efficiency dielectric Huygens′ surfaces," *Advanced Optical Materials*, vol. 3, no. 6, pp. 813–820, 2015.

[34] M. Kerker, D.-S. Wang, and C. Giles, "Electromagnetic scattering by magnetic spheres," *JOSA*, vol. 73, no. 6, pp. 765–767, 1983.

[35] Y. F. Yu, A. Y. Zhu, R. Paniagua-Domínguez, Y. H. Fu, B. Luk'yanchuk, and A. I. Kuznetsov, "High-transmission dielectric metasurface with 2π phase control at visible wavelengths," *Laser & Photonics Reviews*, vol. 9, no. 4, pp. 412–418, 2015.

[36] I. Staude, A. E. Miroshnichenko, M. Decker, N. T. Fofang, S. Liu, E. Gonzales, J. Dominguez, T. S. Luk, D. N. Neshev, I. Brener, *et al.*, "Tailoring directional scattering through magnetic and electric resonances in subwavelength silicon nanodisks," *ACS Nano*, vol. 7, no. 9, pp. 7824–7832, 2013.

[37] M. I. Shalaev, J. Sun, A. Tsukernik, A. Pandey, K. Nikolskiy, and N. M. Litchinitser, "High-efficiency all-dielectric metasurfaces for ultracompact beam manipulation in transmission mode," *Nano Letters*, vol. 15, no. 9, pp. 6261–6266, 2015.

[38] A. Arbabi, Y. Horie, M. Bagheri, and A. Faraon, "Dielectric metasurfaces for complete control of phase and polarization with subwavelength spatial resolution and high transmission," *Nature Nanotechnology*, pp. 937–943, 2015.

[39] Y. Yang, A. E. Miroshnichenko, S. V. Kostinski, M. Odit, P. Kapitanova, M. Qiu, and Y. S. Kivshar, "Multimode directionality in all-dielectric metasurfaces," *Physical Review B*, vol. 95, no. 16, p. 165426, 2017.

[40] W. T. Chen, A. Y. Zhu, V. Sanjeev, M. Khorasaninejad, Z. Shi, E. Lee, and F. Capasso, "A broadband achromatic metalens for focusing and imaging in the visible," *Nature Nanotechnology*, vol. 13, no. 3, p. 220, 2018.

[41] S. Shrestha, A. C. Overvig, M. Lu, A. Stein, and N. Yu, "Broadband achromatic dielectric metalenses," *Light: Science & Applications*, vol. 7, no. 1, p. 85, 2018.

[42] K. Busch, M. König, and J. Niegemann, "Discontinuous galerkin methods in nanophotonics," *Laser & Photonics Reviews*, vol. 5, no. 6, pp. 773–809, 2011.

[43] B. Gallinet, J. Butet, and O. J. Martin, "Numerical methods for nanophotonics: standard problems and future challenges," *Laser & Photonics Reviews*, vol. 9, no. 6, pp. 577–603, 2015.

[44] "www.lumerical.com/tcad-products/fdtd/ for software details."

[45] A. Kristensen, J. K. Yang, S. I. Bozhevolnyi, S. Link, P. Nordlander, N. J. Halas, and N. A. Mortensen, "Plasmonic colour generation," *Nature Reviews Materials*, vol. 2, no. 1, p. 16088, 2017.

[46] L. Cao, P. Fan, E. S. Barnard, A. M. Brown, and M. L. Brongersma, "Tuning the color of silicon nanostructures," *Nano Letters*, vol. 10, no. 7, pp. 2649–2654, 2010.

[47] J. Proust, F. Bedu, B. Gallas, I. Ozerov, and N. Bonod, "All-dielectric colored metasurfaces with silicon mie resonators," *ACS Nano*, vol. 10, no. 8, pp. 7761–7767, 2016.

[48] Z. Li, M.-H. Kim, C. Wang, Z. Han, S. Shrestha, A. C. Overvig, M. Lu, A. Stein, A. M. Agarwal, M. Lončar, *et al.*, "Controlling propagation and coupling of waveguide modes using phase-gradient metasurfaces," *Nature Nanotechnology*, vol. 12, no. 7, p. 675, 2017.

[49] K. Kumar, H. Duan, R. S. Hegde, S. C. Koh, J. N. Wei, and J. K. Yang, "Printing colour at the optical diffraction limit," *Nature Nanotechnology*, vol. 7, no. 9, pp. 557–561, 2012.

[50] V. Vashistha, G. Vaidya, R. S. Hegde, A. E. Serebryannikov, N. Bonod, and M. Krawczyk, "All-dielectric metasurfaces based on cross-shaped resonators for color pixels with extended gamut," *ACS Photonics*, vol. 4, no. 5, pp. 1076–1082, 2017.

[51] V. Vashistha, G. Vaidya, P. Gruszecki, A. E. Serebryannikov, and M. Krawczyk, "Polarization tunable all-dielectric color filters based on cross-shaped si nanoantennas," *Scientific Reports*, vol. 7, no. 1, p. 8092, 2017.

[52] Z.-W. Xie, J.-H. Yang, V. Vashistha, W. Lee, and K.-P. Chen, "Liquid-crystal tunable color filters based on aluminum metasurfaces," *Optics express*, vol. 25, no. 24, pp. 30764–30770, 2017.

[53] V. Vashistha, M. Krawczyk, A. E. Serebryannikov, and G. A. Vandenbosch, "Light guiding, bending, and splitting via local modification of interfaces of a photonic waveguide," *Optics Letters*, vol. 44, no. 19, pp. 4725–4728, 2019.

[54] R. F. Lyon, "A brief history of'pixel'," in *Digital Photography II*, vol. 6069, p. 606901, International Society for Optics and Photonics, 2006.

[55] B. E. Bayer, "Color imaging array," July 20 1976. US Patent 3,971,065.

[56] T. Kudo, Y. Nanjo, Y. Nozaki, K. Nagao, H. Yamaguchi, W.-B. Kang, and G. Pawlowski, "Pigmented photoresists for color filters," *Journal of Photopolymer Science and Technology*, vol. 9, no. 1, pp. 109–119, 1996.

[57] H. Taguchi and M. Enokido, "Technology of color filter materials for image sensor," in *Proceedings International Image Sensor Workshop*, pp. 8–11, 2011.

[58] R. F. Lyon and P. M. Hubel, "Eyeing the camera: Into the next century," in *Color and Imaging Conference*, vol. 2002, pp. 349–355, Society for Imaging Science and Technology, 2002.

[59] "See http://www.foveon.com/article.php?a=69."

[60] G. de Graaf and R. F. Wolffenbuttel, "Illumination source identification using a cmos optical microsystem," *IEEE Transactions on Instrumentation and Measurement*, vol. 53, no. 2, pp. 238–242, 2004.

[61] P. Vukusic and J. R. Sambles, "Photonic structures in biology," *Nature*, vol. 424, no. 6950, p. 852, 2003.

[62] I. Newton, *Opticks, or, a treatise of the reflections, refractions, inflections & colours of light*. Courier Corporation, 1952.

[63] I. Freestone, N. Meeks, M. Sax, and C. Higgitt, "The lycurgus cupa roman nanotechnology," *Gold Bulletin*, vol. 40, no. 4, pp. 270–277, 2007.

[64] Y. Gu, L. Zhang, J. K. Yang, S. P. Yeo, and C.-W. Qiu, "Color generation via subwavelength plasmonic nanostructures," *Nanoscale*, vol. 7, no. 15, pp. 6409–6419, 2015.

[65] A. V. Kildishev, A. Boltasseva, and V. M. Shalaev, "Planar photonics with metasurfaces," *Science*, vol. 339, no. 6125, p. 1232009, 2013.

[66] R. Adato, A. A. Yanik, J. J. Amsden, D. L. Kaplan, F. G. Omenetto, M. K. Hong, S. Erramilli, and H. Altug, "Ultra-sensitive vibrational spectroscopy of protein monolayers with plasmonic nanoantenna arrays," *Proceedings of the National Academy of Sciences*, vol. 106, no. 46, pp. 19227–19232, 2009.

[67] N. Liu, M. Mesch, T. Weiss, M. Hentschel, and H. Giessen, "Infrared perfect absorber and its application as plasmonic sensor," *Nano Letters*, vol. 10, no. 7, pp. 2342–2348, 2010.

[68] H. A. Atwater and A. Polman, "Plasmonics for improved photovoltaic devices," *Nature Materials*, vol. 9, no. 3, pp. 205–213, 2010.

[69] X. Chen, B. Jia, J. K. Saha, B. Cai, N. Stokes, Q. Qiao, Y. Wang, Z. Shi, and M. Gu, "Broadband enhancement in thin-film amorphous silicon solar cells enabled by nucleated silver nanoparticles," *Nano Letters*, vol. 12, no. 5, pp. 2187–2192, 2012.

[70] T. D. James, P. Mulvaney, and A. Roberts, "The plasmonic pixel: large area, wide gamut color reproduction using aluminum nanostructures," *Nano Letters*, vol. 16, no. 6, pp. 3817–3823, 2016.

[71] E. Almeida, O. Bitton, and Y. Prior, "Nonlinear metamaterials for holography," *Nature Communications*, vol. 7, p. 12533, 2016.

[72] X. Ni, A. V. Kildishev, and V. M. Shalaev, "Metasurface holograms for visible light," *Nature Communications*, vol. 4, p. 3807, 2013.

[73] S. J. Tan, L. Zhang, D. Zhu, X. M. Goh, Y. M. Wang, K. Kumar, C.-W. Qiu, and J. K. Yang, "Plasmonic color palettes for photorealistic printing with aluminum nanostructures," *Nano Letters*, vol. 14, no. 7, pp. 4023–4029, 2014.

[74] J. S. Clausen, E. Højlund-Nielsen, A. B. Christiansen, S. Yazdi, M. Grajower, H. Taha, U. Levy, A. Kristensen, and N. A. Mortensen, "Plasmonic metasurfaces for coloration of plastic consumer products," *Nano Letters*, vol. 14, no. 8, pp. 4499–4504, 2014.

[75] M. Srinivasarao, "Nano-optics in the biological world: beetles, butterflies, birds, and moths," *Chemical Reviews*, vol. 99, no. 7, pp. 1935–1962, 1999.

[76] P. Vukusic, J. Sambles, C. Lawrence, and R. Wootton, "Structural colour: now you see it —now you don't," *Nature*, vol. 410, no. 6824, pp. 36–36, 2001.

[77] S. Kinoshita, S. Yoshioka, and J. Miyazaki, "Physics of structural colors," *Reports on Progress in Physics*, vol. 71, no. 7, p. 076401, 2008.

[78] B. Gralak, G. Tayeb, and S. Enoch, "Morpho butterflies wings color modeled with lamellar grating theory," *Optics Express*, vol. 9, no. 11, pp. 567–578, 2001.

[79] Y.-K. R. Wu, A. E. Hollowell, C. Zhang, and L. J. Guo, "Angle-insensitive structural colours based on metallic nanocavities and coloured pixels beyond the diffraction limit," *Scientific Reports*, vol. 3, p. 1194, 2013.

[80] E. Højlund-Nielsen, J. Weirich, J. Nørregaard, J. Garnaes, N. A. Mortensen, and A. Kristensen, "Angle-independent structural colors of silicon," *Journal of Nanophotonics*, vol. 8, no. 1, pp. 083988–083988, 2014.

[81] A. S. Roberts, A. Pors, O. Albrektsen, and S. I. Bozhevolnyi, "Subwavelength plasmonic color printing protected for ambient use," *Nano Letters*, vol. 14, no. 2, pp. 783–787, 2014.

[82] T. Ellenbogen, K. Seo, and K. B. Crozier, "Chromatic plasmonic polarizers for active visible color filtering and polarimetry," *Nano Letters*, vol. 12, no. 2, pp. 1026–1031, 2012.

[83] K. Diest, V. Liberman, D. M. Lennon, P. B. Welander, and M. Rothschild, "Aluminum plasmonics: optimization of plasmonic properties using liquid-prism-coupled ellipsometry," *Optics Express*, vol. 21, no. 23, pp. 28638–28650, 2013.

[84] Z. Li, A. W. Clark, and J. M. Cooper, "Dual color plasmonic pixels create a polarization controlled nano color palette," *ACS Nano*, vol. 10, no. 1, pp. 492–498, 2016.

[85] L. Duempelmann, D. Casari, A. Luu-Dinh, B. Gallinet, and L. Novotny, "Color rendering plasmonic aluminum substrates with angular symmetry breaking," *ACS Nano*, vol. 9, no. 12, pp. 12383–12391, 2015.

[86] L. Wang, R. J. H. Ng, S. Safari Dinachali, M. Jalali, Y. Yu, and J. K. Yang, "Large area plasmonic color palettes with expanded gamut using colloidal self-assembly," *ACS Photonics*, vol. 3, no. 4, pp. 627–633, 2016.

[87] P. Richner, P. Galliker, T. Lendenmann, S. J. Kress, D. K. Kim, D. J. Norris, and D. Poulikakos, "Full-spectrum flexible color printing at the diffraction limit," *ACS Photonics*, vol. 3, no. 5, pp. 754–757, 2016.

[88] J. Fan, W. Wu, Z. Chen, J. Zhu, and J. Li, "Three-dimensional cavity nanoantennas with resonant-enhanced surface plasmons as dynamic color-tuning reflectors," *Nanoscale*, 2017.

[89] H. Ehrenreich and H. R. Philipp, "Optical properties of ag and cu," *Physical Review*, vol. 128, pp. 1622–1629, Nov 1962.

[90] P. R. West, S. Ishii, G. V. Naik, N. K. Emani, V. M. Shalaev, and A. Boltasseva, "Searching for better plasmonic materials," *Laser & Photonics Rev.*, vol. 4, no. 6, pp. 795–808, 2010.

[91] D. Gérard and S. K. Gray, "Aluminium plasmonics," *Journal of Physics D: Applied Physics*, vol. 48, no. 18, p. 184001, 2014.

[92] R. Paniagua-Domínguez, Y. F. Yu, A. E. Miroschnichenko, L. A. Krivitsky, Y. H. Fu, V. Valuckas, L. Gonzaga, Y. T. Toh, A. Y. S. Kay, B. Luk'yanchuk, and A. I. Kuznetsov, "Generalized brewster effect in dielectric metasurfaces," *Nature Communications*, vol. 7, p. 10362, 2016.

[93] N. Bonod, "Silicon photonics: Large-scale dielectric metasurfaces," *Nature Materials*, vol. 14, no. 7, pp. 664–665, 2015.

[94] S. Jahani and Z. Jacob, "All-dielectric metamaterials," *Nature Nanotechnology*, vol. 11, no. 1, pp. 23–36, 2016.

[95] J. Sautter, I. Staude, M. Decker, E. Rusak, D. N. Neshev, I. Brener, and Y. S. Kivshar, "Active tuning of all-dielectric metasurfaces," *ACS Nano*, vol. 9, no. 4, pp. 4308–4315, 2015.

[96] J. Li, N. Verellen, D. Vercruysse, T. Bearda, L. Lagae, and P. Van Dorpe, "All-dielectric antenna wavelength router with bidirectional scattering of visible light," *Nano Letters*, vol. 16, no. 7, pp. 4396–4403, 2016.

[97] P. Moitra, B. A. Slovick, W. Li, I. I. Kravchencko, D. P. Briggs, S. Krishnamurthy, and J. Valentine, "Large-scale all-dielectric metamaterial perfect reflectors," *ACS Photonics*, vol. 2, no. 6, pp. 692–698, 2015.

[98] S. Liu, M. B. Sinclair, T. S. Mahony, Y. C. Jun, S. Campione, J. Ginn, D. A. Bender, J. R. Wendt, J. F. Ihlefeld, P. G. Clem, J. B. Wright, and I. Brener, "Optical magnetic mirrors without metals," *Optica*, vol. 1, pp. 250–256, Oct 2014.

[99] R. S. Hegde and K. S. Panse, "Design and optimization of ultrathin spectral filters based on silicon nanocross antenna arrays," *Journal of Nanophotonics*, vol. 10, no. 2, pp. 026030–026030, 2016.

[100] I. Staude, A. E. Miroshnichenko, M. Decker, N. T. Fofang, S. Liu, E. Gonzales, J. Dominguez, T. S. Luk, D. N. Neshev, I. Brener, and Y. Kivshar, "Tailoring directional scattering through magnetic and electric resonances in subwavelength silicon nanodisks," *ACS Nano*, vol. 7, no. 9, pp. 7824–7832, 2013.

[101] D. Lin, P. Fan, E. Hasman, and M. L. Brongersma, "Dielectric gradient metasurface optical elements," *Science*, vol. 345, no. 6194, pp. 298–302, 2014.

[102] W. Yue, S. Gao, S.-S. Lee, E.-S. Kim, and D.-Y. Choi, "Subtractive color filters based on a silicon-aluminum hybrid-nanodisk metasurface enabling enhanced color purity," *Scientific Reports*, vol. 6, p. 29756, 2016.

[103] V. R. Shrestha, S.-S. Lee, E.-S. Kim, and D.-Y. Choi, "Polarization-tuned dynamic color filters incorporating a dielectric-loaded aluminum nanowire array," *Scientific Reports*, vol. 5, p. 12450, 2015.

[104] W. Zhao, B. Liu, H. Jiang, J. Song, Y. Pei, and Y. Jiang, "Full-color hologram using spatial multiplexing of dielectric metasurface," *Optics Letters*, vol. 41, no. 1, pp. 147–150, 2016.

[105] "http://colour.readthedocs.io/en/latest."

[106] "https://graphics.stanford.edu/courses/cs178/applets/custom-subtractive-too-wide.jpg."

[107] E. Hutter and J. H. Fendler, "Exploitation of localized surface plasmon resonance," *Advanced Materials*, vol. 16, no. 19, pp. 1685–1706, 2004.

[108] B. Zeng, Y. Gao, and F. Bartoli, "Ultrathin nanostructured metals for highly transmissive plasmonic subtractive color filters," in *CLEO: Science and Innovations*, pp. STu1M–6, Optical Society of America, 2014.

[109] J.-H. Yang and K.-P. Chen, "Evanescent wave-assisted symmetry breaking of gold dipolar nanoantennas," *Scientific Reports*, vol. 6, 2016.

[110] C.-W. Su and K.-P. Chen, "Broadband gold nanoantennas arrays with transverse dimension effects," *Optics Express*, vol. 24, no. 16, pp. 17760–17765, 2016.

[111] F. Cheng, J. Gao, T. S. Luk, and X. Yang, "Structural color printing based on plasmonic metasurfaces of perfect light absorption," *Scientific Reports*, vol. 5, p. 11045, 2015.

[112] T. Xu, Y.-K. Wu, X. Luo, and L. J. Guo, "Plasmonic nanoresonators for high-resolution colour filtering and spectral imaging," *Nature Communications*, vol. 1, p. 59, 2010.

[113] R. Rajasekharan, E. Balaur, A. Minovich, S. Collins, T. D. James, A. Djalalian-Assl, K. Ganesan, S. Tomljenovic-Hanic, S. Kandasamy, E. Skafidas, *et al.*, "Filling schemes at submicron scale: Development of submicron sized plasmonic colour filters," *Scientific Reports*, vol. 4, p. 6435, 2014.

[114] C. J. DeSantis, M. J. McClain, and N. J. Halas, "Walking the walk: A giant step toward sustainable plasmonics," *ACS Nano*, vol. 10, no. 11, pp. 9772–9775, 2016.

[115] M. W. Knight, N. S. King, L. Liu, H. O. Everitt, P. Nordlander, and N. J. Halas, "Aluminum for plasmonics," *ACS Nano*, vol. 8, no. 1, pp. 834–840, 2013.

[116] C.-S. Park, V. R. Shrestha, S.-S. Lee, and D.-Y. Choi, "Trans-reflective color filters based on a phase compensated etalon enabling adjustable color saturation," *Scientific Reports*, vol. 6, p. 25496, 2016.

[117] Y. Yu, L. Wen, S. Song, and Q. Chen, "Transmissive/reflective structural color filters: theory and applications," *Journal of Nanomaterials*, vol. 2014, p. 6, 2014.

[118] S. U. Lee and B.-K. Ju, "Wide-gamut plasmonic color filters using a complementary design method," *Scientific Reports*, vol. 7, p. 40649, 2017.

[119] T. Smith and J. Guild, "The c.i.e. colorimetric standards and their use," *Transactions of the Optical Society*, vol. 33, no. 3, p. 73, 1931.

[120] N. Dean, "Colouring at the nanoscale," *Nature Nanotechnology*, vol. 10, no. 1, p. 15, 2015.

[121] X. Zhu, W. Yan, U. Levy, N. A. Mortensen, and A. Kristensen, "Resonant laser printing of structural colors on high-index dielectric metasurfaces," *Science Advances*, vol. 3, no. 5, p. e1602487, 2017.

[122] K. Diest, J. A. Dionne, M. Spain, and H. A. Atwater, "Tunable color filters based on metal- insulator- metal resonators," *Nano Letters*, vol. 9, no. 7, pp. 2579–2583, 2009.

[123] M. Miyata, H. Hatada, and J. Takahara, "Full-color subwavelength printing with gap-plasmonic optical antennas," *Nano Letters*, vol. 16, no. 5, pp. 3166–3172, 2016.

[124] X. Zhu, C. Vannahme, E. Højlund-Nielsen, N. A. Mortensen, and A. Kristensen, "Plasmonic colour laser printing," *Nature Nanotechnology*, vol. 11, no. 4, p. 325, 2016.

[125] W. Yue, S. Gao, S.-S. Lee, E.-S. Kim, and D.-Y. Choi, "Highly reflective subtractive color filters capitalizing on a silicon metasurface integrated with nanostructured aluminum mirrors," *Laser & Photonics Reviews*, vol. 11, no. 3, p. 1600285, 2017.

[126] Y.-W. Huang, W. T. Chen, W.-Y. Tsai, P. C. Wu, C.-M. Wang, G. Sun, and D. P. Tsai, "Aluminum plasmonic multicolor meta-hologram," *Nano Letters*, vol. 15, no. 5, pp. 3122–3127, 2015.

[127] X. Duan, S. Kamin, and N. Liu, "Dynamic plasmonic colour display," *Nature Communications*, vol. 8, p. 14606, 2017.

[128] M. L. Tseng, J. Yang, M. Semmlinger, C. Zhang, P. Nordlander, and N. J. Halas, "Two-dimensional active tuning of an aluminum plasmonic array for full-spectrum response," *Nano Letters*, vol. 17, no. 10, pp. 6034–6039, 2017.

[129] J. Olson, A. Manjavacas, T. Basu, D. Huang, A. E. Schlather, B. Zheng, N. J. Halas, P. Nordlander, and S. Link, "High chromaticity aluminum plasmonic pixels for active liquid crystal displays," *ACS Nano*, vol. 10, no. 1, pp. 1108–1117, 2015.

[130] W. Dickson, G. A. Wurtz, P. R. Evans, R. J. Pollard, and A. V. Zayats, "Electronically controlled surface plasmon dispersion and optical transmission through metallic hole arrays using liquid crystal," *Nano Letters*, vol. 8, no. 1, pp. 281–286, 2008.

[131] V. K. Hsiao, Y. B. Zheng, B. K. Juluri, and T. J. Huang, "Light-driven plasmonic switches based on au nanodisk arrays and photoresponsive liquid crystals," *Advanced Materials*, vol. 20, no. 18, pp. 3528–3532, 2008.

[132] G. Si, Y. Zhao, E. Leong, and Y. Liu, "Liquid-crystal-enabled active plasmonics: a review," *Materials*, vol. 7, no. 2, pp. 1296–1317, 2014.

[133] Y.-C. Hsiao, C.-W. Su, Z.-H. Yang, Y. I. Cheypesh, J.-H. Yang, V. Y. Reshetnyak, K.-P. Chen, and W. Lee, "Electrically active nanoantenna array enabled by varying the molecular orientation of an interfaced liquid crystal," *RSC Advances*, vol. 6, no. 87, pp. 84500–84504, 2016.

[134] K.-P. Chen, S.-C. Ye, C.-Y. Yang, Z.-H. Yang, W. Lee, and M.-G. Sun, "Electrically tunable transmission of gold binary-grating metasurfaces integrated with liquid crystals," *Optics Express*, vol. 24, no. 15, pp. 16815–16821, 2016.

[135] G. Gilardi, D. Donisi, A. Serpengüzel, and R. Beccherelli, "Liquid-crystal tunable filter based on sapphire microspheres," *Optics letters*, vol. 34, no. 21, pp. 3253–3255, 2009.

[136] A. Komar, Z. Fang, J. Bohn, J. Sautter, M. Decker, A. Miroshnichenko, T. Pertsch, I. Brener, Y. S. Kivshar, I. Staude, *et al.*, "Electrically tunable all-dielectric optical metasurfaces based on liquid crystals," *Applied Physics Letters*, vol. 110, no. 7, p. 071109, 2017.

[137] Y. J. Liu, G. Y. Si, E. S. Leong, N. Xiang, A. J. Danner, and J. H. Teng, "Light-driven plasmonic color filters by overlaying photoresponsive liquid crystals on gold annular aperture arrays," *Advanced Materials*, vol. 24, no. 23, pp. OP131–OP135, 2012.

[138] D. Franklin, Y. Chen, A. Vazquez-Guardado, S. Modak, J. Boroumand, D. Xu, S.-T. Wu, and D. Chanda, "Polarization-independent actively tunable colour generation on imprinted plasmonic surfaces," *Nature Communications*, vol. 6, p. 7337, 2015.

[139] W. Lee, J.-S. Gau, and H.-Y. Chen, "Electro-optical properties of planar nematic cells impregnated with carbon nanosolids," *Applied Physics B*, vol. 81, no. 2-3, pp. 171–175, 2005.

[140] G. Bryan-Brown, C. Brown, I. Sage, and V. Hui, "Voltage-dependent anchoring of a nematic liquid crystal on a grating surface," *Nature*, vol. 392, no. 6674, p. 365, 1998.

[141] S. P. Palto, M. I. Barnik, V. V. Artemov, I. V. Kasyanova, N. M. Shtykov, A. R. Geivandov, S. G. Yudin, and M. V. Gorkunov, "Voltage-tunable optical transmission of subwavelength metal gratings filled with liquid crystals," in *Metamaterials X*, vol. 9883, p. 988307, International Society for Optics and Photonics, 2016.

[142] Q. Cao and P. Lalanne, "Negative role of surface plasmons in the transmission of metallic gratings with very narrow slits," *Physical Review Letters*, vol. 88, no. 5, p. 057403, 2002.

[143] Z. Li, M.-H. Kim, C. Wang, Z. Han, S. Shrestha, A. C. Overvig, M. Lu, A. Stein, A. M. Agarwal, M. Loncar, and N. Yu, "Controlling propagation and coupling of waveguide modes using phase-gradient metasurfaces," *Nature Nanotechnology*, vol. 12, pp. 675–683, 2017.

[144] Z. H. Jiang, L. Kang, and D. H. Werner, "Conformal metasurface-coated dielectric waveguides for highly confined broadband optical activity with simultaneous low-visibility and reduced crosstalk," *Nature Communications*, vol. 8, no. 1, p. 356, 2017.

[145] A. Chutinan and S. Noda, "Waveguides and waveguide bends in two-dimensional photonic crystal slabs," *Physical Review B*, vol. 62, no. 7, p. 4488, 2000.

[146] S. G. Johnson, P. R. Villeneuve, S. Fan, and J. D. Joannopoulos, "Linear waveguides in photonic-crystal slabs," *Physical Review B*, vol. 62, no. 12, p. 8212, 2000.

[147] W. Park and C. J. Summers, "Extraordinary refraction and dispersion in two-dimensional photonic-crystal slabs," *Optics Letters*, vol. 27, no. 16, pp. 1397–1399, 2002.

[148] X. Ao, L. Liu, L. Wosinski, and S. He, "Polarization beam splitter based on a two-dimensional photonic crystal of pillar type," *Applied Physics Letters*, vol. 89, no. 17, p. 171115, 2006.

[149] R. Pourabolghasem, R. Dehghannasiri, A. A. Eftekhar, and A. Adibi, "Waveguiding effect in the gigahertz frequency range in pillar-based phononic-crystal slabs," *Physical Review Applied*, vol. 9, no. 1, p. 014013, 2018.

[150] T. Baba, A. Motegi, T. Iwai, N. Fukaya, Y. Watanabe, and A. Sakai, "Light propagation characteristics of straight single-line-defect waveguides in photonic crystal slabs fabricated into a silicon-on-insulator substrate," *IEEE Journal of Quantum Electronics*, vol. 38, no. 7, pp. 743–752, 2002.

[151] M. Loncar, T. Doll, J. Vuckovic, and A. Scherer, "Design and fabrication of silicon photonic crystal optical waveguides," *Journal of Lightwave Technology*, vol. 18, no. 10, pp. 1402–1411, 2000.

[152] M. Notomi, A. Shinya, S. Mitsugi, E. Kuramochi, and H. Ryu, "Waveguides, resonators and their coupled elements in photonic crystal slabs," *Optics Express*, vol. 12, no. 8, pp. 1551–1561, 2004.

[153] R. Wilson, T. J. Karle, I. Moerman, and T. F. Krauss, "Efficient photonic crystal y-junctions," *Journal of Optics A: Pure and Applied Optics*, vol. 5, no. 4, p. S76, 2003.

[154] M. Kafesaki, M. Agio, and C. Soukoulis, "Waveguides in finite-height two-dimensional photonic crystals," *JOSA B*, vol. 19, no. 9, pp. 2232–2240, 2002.

[155] N. F. van Hulst, "Photonics: Light in chains," *Nature*, vol. 448, no. 7150, p. 141, 2007.

[156] R. M. Bakker, Y. F. Yu, R. Paniagua-Domnguez, B. Lukyanchuk, and A. I. Kuznetsov, "Resonant light guiding along a chain of silicon nanoparticles," *Nano Letters*, vol. 17, no. 6, pp. 3458–3464, 2017.

[157] R. S. Savelev, D. S. Filonov, M. I. Petrov, A. E. Krasnok, P. A. Belov, and Y. S. Kivshar, "Resonant transmission of light in chains of high-index dielectric particles," *Physical Review B*, vol. 92, no. 15, p. 155415, 2015.

[158] S. Fan, J. N. Winn, A. Devenyi, J. Chen, R. D. Meade, and J. Joannopoulos, "Guided and defect modes in periodic dielectric waveguides," *JOSA B*, vol. 12, no. 7, pp. 1267–1272, 1995.

[159] M. Beruete, F. Falcone, M. Freire, R. Marques, and J. Baena, "Electroinductive waves in chains of complementary metamaterial elements," *Applied Physics Letters*, vol. 88, no. 8, p. 083503, 2006.

[160] J. K. Poon, L. Zhu, G. A. DeRose, and A. Yariv, "Transmission and group delay of microring coupled-resonator optical waveguides," *Optics Letters*, vol. 31, no. 4, pp. 456–458, 2006.

[161] M. I. Shalaev, W. Walasik, A. Tsukernik, Y. Xu, and N. M. Litchinitser, "Robust topologically protected transport in photonic crystals at telecommunication wavelengths," *Nature Nanotechnology*, vol. 14, pp. 31–34, 2019.

[162] E. D. Palik, *Handbook of optical constants of solids*, vol. 3. Academic press, 1998.

[163] T. Ito and K. Sakoda, "Photonic bands of metallic systems. ii. features of surface plasmon polaritons," *Physical Review B*, vol. 64, no. 4, p. 045117, 2001.

[164] S. Nojima, "Excitonic polaritons in one-dimensional photonic crystals," *Physical Review B*, vol. 57, no. 4, p. R2057, 1998.

[165] "https://www.3ds.com/products-services/simulia/."

[166] S. V. Pishko, P. D. Sewell, T. M. Benson, and S. V. Boriskina, "Efficient analysis and design of low-loss whispering-gallery-mode coupled resonator optical waveguide bends," *Journal of Lightwave Technology*, vol. 25, no. 9, pp. 2487–2494, 2007.

[167] E. Colak, A. E. Serebryannikov, P. Usik, and E. Ozbay, "Diffraction inspired unidirectional and bidirectional beam splitting in defect-containing photonic structures without interface corrugations," *Journal of Applied Physics*, vol. 119, no. 19, p. 193108, 2016.

[168] M. Veysi, C. Guclu, O. Boyraz, and F. Capolino, "Thin anisotropic metasurfaces for simultaneous light focusing and polarization manipulation," *JOSA B*, vol. 32, no. 2, pp. 318–323, 2015.

[169] T. Cai, S. Tang, G. Wang, H. Xu, S. Sun, Q. He, and L. Zhou, "High-performance bifunctional metasurfaces in transmission and reflection geometries," *Advanced Optical Materials*, vol. 5, no. 2, p. 1600506, 2017.

[170] A. E. Serebryannikov, K. B. Alici, T. Magath, A. O. Cakmak, and E. Ozbay, "Asymmetric fabry-perot-type transmission in photonic-crystal gratings with one-sided corrugations at a two-way coupling," *Physical Review A*, vol. 86, no. 5, p. 053835, 2012.

[171] P. Rodríguez-Ulibarri, M. Beruete, and A. E. Serebryannikov, "One-way quasi-planar terahertz absorbers using nonstructured polar dielectric layers," *Physical Review B*, vol. 96, no. 15, p. 155148, 2017.

[172] X. Wang, J. Ding, B. Zheng, S. An, G. Zhai, and H. Zhang, "Simultaneous realization of anomalous reflection and transmission at two frequencies using bi-functional metasurfaces," *Scientific Reports*, vol. 8, no. 1, p. 1876, 2018.

[173] H. S. Song, G. J. Lee, D. E. Yoo, Y. J. Kim, Y. J. Yoo, D.-W. Lee, V. Siva, I.-S. Kang, and Y. M. Song, "Reflective color filter with precise control of the color coordinate achieved by stacking silicon nanowire arrays onto ultrathin optical coatings," *Scientific reports*, vol. 9, no. 1, p. 3350, 2019.

[174] E. Panchenko, L. Wesemann, D. E. Gómez, T. D. James, T. J. Davis, and A. Roberts, "Ultracompact camera pixel with integrated plasmonic color filters," *Advanced Optical Materials*, p. 1900893, 2019.

[175] Y. Nagasaki, M. Suzuki, I. Hotta, and J. Takahara, "Control of si-based all-dielectric printing color through oxidation," *ACS Photonics*, vol. 5, no. 4, pp. 1460–1466, 2018.

[176] W. Chaabani, J. Proust, A. Movsesyan, J. Beal, A.-L. Baudrion, P.-M. Adam, A. Chehaidar, and J. Plain, "Large-scale and low-cost fabrication of silicon mie resonators," *ACS Nano*, vol. 13, no. 4, pp. 4199–4208, 2019.

[177] M. Rumler, M. Foerthner, L. Baier, P. Evanschitzky, M. Becker, M. Rommel, and L. Frey, "Large area manufacturing of plasmonic colour filters using substrate conformal imprint lithography," *Nano Futures*, vol. 1, no. 1, p. 015002, 2017.

[178] P. Liu, L. Bai, J. Yang, H. Gu, Q. Zhong, Z. Xie, and Z. Gu, "Self-assembled colloidal arrays for structural color," *Nanoscale Advances*, vol. 1, no. 5, pp. 1672–1685, 2019.

[179] H. Kwon, D. Sounas, A. Cordaro, A. Polman, and A. Alù, "Nonlocal metasurfaces for optical signal processing," *Physical Review Letters*, vol. 121, no. 17, p. 173004, 2018.

[180] P. del Hougne, M. F. Imani, A. V. Diebold, R. Horstmeyer, and D. R. Smith, "Artificial neural network with physical dynamic metasurface layer for optimal sensing," *arXiv preprint arXiv:1906.10251*, 2019.

[181] L. Li, H. Ruan, C. Liu, Y. Li, Y. Shuang, A. Alù, C.-W. Qiu, and T. J. Cui, "Machine-learning reprogrammable metasurface imager," *Nature Communications*, vol. 10, no. 1, p. 1082, 2019.

[182] K. Wang, J. G. Titchener, S. S. Kruk, L. Xu, H.-P. Chung, M. Parry, I. I. Kravchenko, Y.-H. Chen, A. S. Solntsev, Y. S. Kivshar, *et al.*, "Quantum metasurface for multiphoton interference and state reconstruction," *Science*, vol. 361, no. 6407, pp. 1104–1108, 2018.

[183] P. Georgi, M. Massaro, K.-H. Luo, B. Sain, N. Montaut, H. Herrmann, T. Weiss, G. Li, C. Silberhorn, and T. Zentgraf, "Metasurface interferometry toward quantum sensors," *Light: Science & Applications*, vol. 8, no. 1, pp. 1–7, 2019.